AD

USAAVLABS TECHNICAL REPORT 68-89A

WIND TUNNEL TESTS OF THIN AIRFOILS OSCILLATING NEAR STALL

VOLUME I

SUMMARY AND EVALUATION OF RESULTS

By

Lewis Gray

Jaan Liiva

Franklyn J. Davenport

January 1969

U. S. ARMY AVIATION MATERIEL LABORATORIES
FORT EUSTIS, VIRGINIA

CONTRACT DAAJ02-67-C-0095
THE BOEING COMPANY
VERTOL DIVISION
PHILADELPHIA, PENNSYLVANIA

Disclaimers

The findings in this report are not to be construed as an official Department of the Army position unless so designated by other authorized documents.

When Government drawings, specifications, or other data are used for any purpose other than in connection with a definitely related Government procurement operation, the United States Government thereby incurs no responsibility nor any obligation whatsoever; and the fact that the Government may have formulated, furnished, or in any way supplied the said drawings, specifications, or other data is not to be regarded by implication or otherwise as in any manner licensing the holder or any other person or corporation, or conveying any rights or permission, to manufacture, use, or sell any patented invention that may in any way be related thereto.

Disposition Instructions

Destroy this report when no longer needed. Do not return it to the originator.

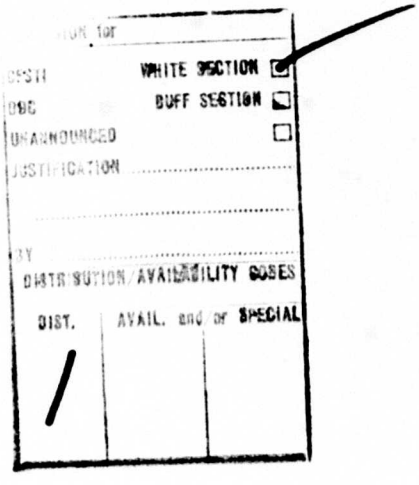

DEPARTMENT OF THE ARMY
U. S. ARMY AVIATION MATERIEL LABORATORIES
FORT EUSTIS, VIRGINIA 23604

This report has been reviewed by the U. S. Army Aviation Materiel Laboratories and is considered to be technically sound. The report is published for the exchange of information and the stimulation of ideas.

Task 1F162204A13903
Contract DAAJ02-67-C-0095
USAAVLABS Technical Report 68-89A
January 1969

WIND TUNNEL TESTS OF THIN AIRFOILS OSCILLATING NEAR STALL

Final Report

VOLUME I

SUMMARY AND EVALUATION OF RESULTS

D8-0925-1

By

Lewis Gray
Jaan Liiva
Franklyn J. Davenport

Prepared by

THE BOEING COMPANY
VERTOL DIVISION
Philadelphia, Pennsylvania

for

U.S. ARMY AVIATION MATERIEL LABORATORIES
FORT EUSTIS, VIRGINIA

SUMMARY

This report presents the results of an experimental investigation of the dynamic stall of two rotor blade airfoil sections (NACA 0006 and Vertol 13006-.7) chosen for high Mach number operation. Forces and moments in two-dimensional flow were determined by measuring differential pressures in pitching oscillation. Mach number, Reynolds number, and mean angle-of-attack ranges tested corresponded to the conditions prevailing on the retreating blades of full-scale helicopters. Frequencies of oscillation ranged up to the level corresponding to typical first torsional vibration modes of rotor blades.

Pitch oscillation was found to increase the angle of attack at which stall occurred, with a corresponding increase in maximum normal force. Hysteresis effects on the pitching moment response produced regions of negative aerodynamic damping in oscillations at mean angles of attack near the steady-flow stall values for all Mach numbers from 0.2 to 0.6.

The reduced frequency of oscillation was found to be the dominant influence on dynamic stall behavior, although some compressibility effects were noted at Mach numbers up to 0.4, and strong qualitative changes in the stall behavior were evident beyond that value.

Leading-edge camber and increased nose radius were found to increase the angle of attack and normal force at stall at all frequencies tested, as well as at fixed angle of attack. Patterns evident in the force and moment data indicate that these design features produce an effect much like a reduction of the Mach number.

FOREWORD

The results of a program of testing thin airfoils oscillating near stall are summarized in this report. The project was performed for the United States Army Aviation Materiel Laboratories under Contract DAAJ02-67-C-0095 and under the technical cognizance of Clifton G. Wrestler and Patrick Cancro of the Aeromechanics Division of USAAVLABS.

The report consists of two volumes:

Volume I, Summary and Evaluation of Results
Volume II, Data Report

The tests were conducted at the Commercial Airplane Division of The Boeing Company in the supersonic wind tunnel. The assistance and cooperation of the Model Design, Instrumentation, and Supersonic Wind Tunnel Testing Groups are gratefully acknowledged. The assistance of Messrs. W. McLean, K. Simmonds, and L. Dadone of the Vertol Division in running the tests is also greatly appreciated.

BLANK PAGE

TABLE OF CONTENTS

LIST OF ILLUSTRATIONS

LIST OF SYMBOLS

b	airfoil semichord, feet
C_D	airfoil drag coefficient
$\overline{C}_D$	mean value of drag coefficient over an oscillation cycle
C_M	airfoil pitching moment coefficient about quarter-chord, positive nose-up
$C_{M_{MIN}}$	minimum value of pitching moment coefficient attained in oscillation cycle
C_N	airfoil normal force coefficient, positive up
$C_{N_{MAX}}$	maximum value of normal force coefficient attained in oscillation cycle
C_P	pressure coefficient, $(P - P_S)/1/2\rho V^2$
c	airfoil chord, feet
$dC_M/d\alpha$	rate of change of pitching moment with angle of attack, per degree
f	drive frequency of airfoil motion in pitch, Hertz
H	tunnel height, feet
k	reduced frequency, $\pi fc/V$
M	tunnel free-stream Mach number
n	number of harmonic
P	static pressure, pounds per square inch absolute
P_S	tunnel test section static pressure, pounds per square inch absolute
P_T	tunnel test section total pressure, pounds per square inch absolute
RN	Reynolds number
TP	wind tunnel test point identification

T_T	tunnel test section total temperature, degrees Rankine
V	tunnel velocity, feet per second
W	work function, foot-pounds
x	airfoil chordwise location, measured from leading edge, positive rearward, feet
y	airfoil surface location measured perpendicular to chord line, positive upward, feet
α	instantaneous airfoil angle of attack, positive nose-up, degrees
α_o	mean angle of attack, positive nose-up, degrees
$\Delta\alpha$	amplitude of pitching motion, degrees
ΔC_P	differential pressure coefficient, $\Delta P/\frac{1}{2}\rho V^2$
$\Delta C_P/C_N$	differential pressure coefficient divided by the instantaneous normal force coefficient
ΔP	differential pressure, pounds per square foot
θ	pitching motion cyclic reference angle, degrees
ρ	density of air, slugs per cubic foot
ϕ_M	phase lead of first harmonic pitching moment response with respect to airfoil motion, degrees
ϕ_N	phase lead of first harmonic normal force response with respect to airfoil motion, degrees
1/rev, 3/rev, etc.	one per revolution, three per revolution, etc., corresponding to ratio of airfoil drive frequency to equivalent rotor drive frequency
$\oint$	contour integral

BLANK PAGE

INTRODUCTION

The speed and lifting capability of contemporary helicopters are limited by retreating blade stall. As aircraft speed or weight is increased beyond the stall limit, rapid increases in blade loads, control loads, or rotor horsepower occur. Attempts to predict these effects by using steady-flow airfoil characteristics* in strip theory analyses have been unsuccessful; the onset of stall is predicted too early.

There are two recognized aerodynamic effects, apart from centrifugal effects on the boundary layer, that can cause the differences between test and theory: yawed flow and unsteady aerodynamics. Neither effect has been included in current rotor analyses. In discussing the effects of yawed flow on the rotor blade, Harris[1] shows that part of the discrepancy between test and theory can be eliminated by including yaw effects in the airfoil tables. The second effect, unsteady aerodynamics, has been shown by various investigators (see Bibliography in Reference 2) to produce a stall delay which increases the maximum lift coefficient above that for static stall. In addition to this stall delay, negative aerodynamic damping can occur for pitch oscillations through stall. This negative damping is caused by time lag effects in the blade pitching moment versus angle-of-attack relation and can cause large torsional blade deflections and large control loads. The resulting blade and control stresses caused by stall can limit the flight speed of the helicopter; therefore, it is important that the effects of dynamic stall be fully understood. Further, these dynamic effects must be incorporated in rotor blade analyses in order to predict the performance and flight limitations of high-performance helicopter rotors near stall.

A comprehensive literature search revealed little useful oscillatory data appropriate to helicopter blade applications and no theories which adequately predict dynamic stall effects. To establish a comprehensive framework of experimetnal data for immediate use in rotor analyses, and to provide sufficient data to stimulate the formulation of a dynamic stall theory, a program of two-dimensional wind tunnel tests was conducted in 1966-1967 and is reported in Reference 2. The two airfoils tested in that program were the NACA 0012 (modified) used on the CH-47A, and the Vertol 23010-1.58 currently used on the CH-47B and C models. Those tests substantiated the work of previous investigations and carried the results into many areas where no data were formerly available.

*Tabulated aerodynamic coefficients reflecting both Mach number and flow separation effects.

Many current high-performance rotor blade designs use thin airfoil sections near the tip to postpone the onset of power losses due to compressibility.

No dynamic stall data for such profiles were available, and the need was clear. The test program reported here was conducted to fill that need.

TEST FACILITIES, MODELS, AND DATA SYSTEM

The section presents a brief description of the basic test facility, apparatus, and data recording and reduction system. These are described in more detail in Reference 2. For the present tests, a number of improvements (relating principally to model construction techniques and to the data reduction system) have been made and are discussed below.

TEST FACILITIES

The subsonic, variable-density, two-dimensional, 1-by-3-foot test section of the Boeing 4-by-4-foot supersonic wind tunnel was used to test 8-inch-chord model airfoils. The test section's total pressure and airfoil drive frequency were increased to simulate Reynolds numbers and reduced frequenices corresponding to a 2-foot-chord full-scale rotor blade. The tunnel Mach number capability with the model installed was limited to 0.75 because of blockage effects.

The pitch oscillating mechanism is shown in Figure 1. A hydraulic motor supplies the power to rotate a flywheel with an eccentrically mounted cam. The cam slides in a slotted crank which is rigidly attached to the airfoil model on the pitch axis. Four fixed nominal amplitudes of oscillation, from 2.5 to 10 degrees, are provided by different eccentric locations for the cam.

AIRFOIL MODELS AND INSTRUMENTATION

The first test airfoil was the Vertol 13006-.7. This nose-cambered airfoil, of 6 percent thickness ratio, has an increased leading-edge radius compared with the standard NACA 13006 section. This modification improves the maximum lift characteristics without raising the drag level. The aerodynamic design considerations of this airfoil section are reported by Davenport and Front[3]. To provide a broader data base for thin airfoil dynamic characteristics, a thin symmetrical airfoil section (the NACA 0006) was also tested.

Airfoil contours and coordinates for each model are shown in Figure 2; a statement of the basic model parameters and instrumentation installation is given in the table on page 6. Both models were machined from solid steel in order to obtain adequate structural stiffness.

The miniature differential pressure transducers used for this test were encapsulated in cylindrical plugs before installation in the airfoil, as shown in Figure 3.

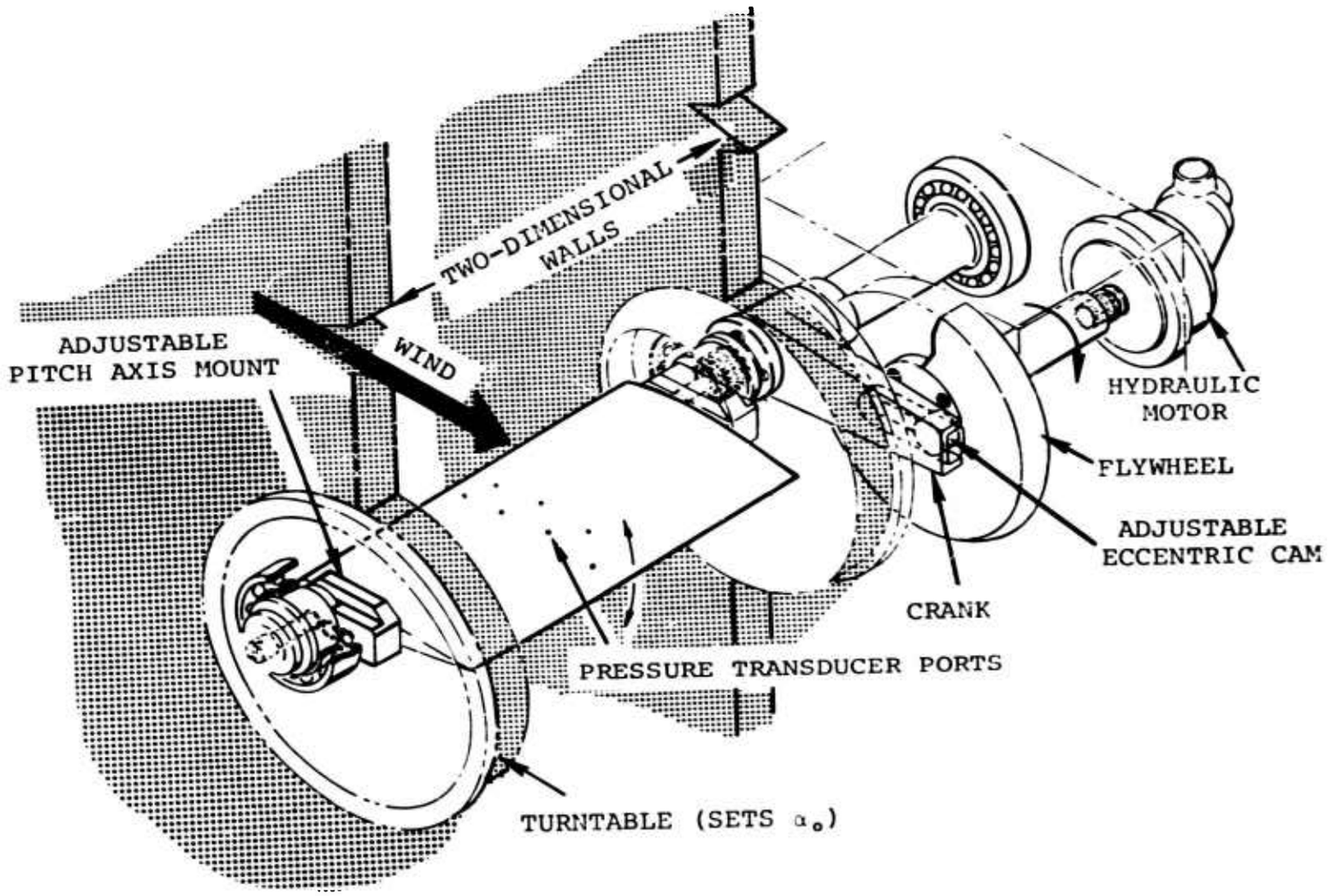

Figure 1. Pitch Oscillating Mechanism.

x/c	y/c
0.0	0.0
0.0125	0.00947
0.025	0.01307
0.050	0.01777
0.075	0.02100
0.100	0.02341
0.150	0.02673
0.200	0.02869
0.250	0.02971

x/c	y/c
0.300	0.03001
0.400	0.02902
0.500	0.02647
0.600	0.02282
0.700	0.01832
0.800	0.01312
0.900	0.00724
0.950	0.00403
1.000	0.00063

LEADING-EDGE RADIUS = 0.004

CENTER { x = 0.004 ; y = 0.0

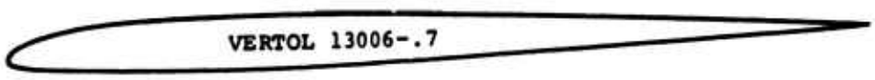

x/c	y/c UPPER	y/c LOWER
-0.0020	-0.0117	-0.0117
0.0	-0.0064	-0.0171
0.0025	-0.0040	-0.0190
0.0075	-0.0013	-0.0208
0.0125	0.0012	-0.0219
0.025	0.0057	-0.0235
0.050	0.0127	-0.0255
0.075	0.0177	-0.0268
0.100	0.0216	-0.0275
0.150	0.0260	-0.0286

x/c	y/c UPPER	y/c LOWER
0.200	0.0285	-0.0294
0.250	0.0295	-0.0299
0.300	0.0299	-0.0300
0.400	0.0290	-0.0290
0.500	0.0265	-0.0265
0.600	0.0228	-0.0228
0.700	0.0183	-0.0183
0.800	0.0131	-0.0131
0.900	0.0072	-0.0072
0.950	0.0040	-0.0040
1.000	0.0006	-0.0006

LEADING-EDGE RADIUS = 0.007

CENTER { x = 0.005 ; y = -0.0117

Figure 2. Test Airfoil Coordinates.

AIRFOIL MODEL AND INSTRUMENTATION DATA	
Item	Description
Airfoil Section	NACA 006 and Vertol 13006-.7
Model Span	12 inches nominal
Model Scale	1/3, based on 2-foot-chord rotor blade
Model Chord	8 inches
Thickness Ratio	6 percent
Construction	Machined from maraging steel
Transducer Type	Scientific Advances SD-M6
Number Installed	14 per model
Location in Percent Chord	1, 2.5, 5, 10, 15, 20, 25, 30, 40, 50, 70, 80, 87.5, 95
Pressure Range	$\pm$ 50 psi located from 1 to 10 percent chord $\pm$ 25 psi located from 15 to 95 percent chord
Minimum Natural Frequency of Installed Transducers	4,000 Hertz
Damping Ratio of Installed Transducers	0.25

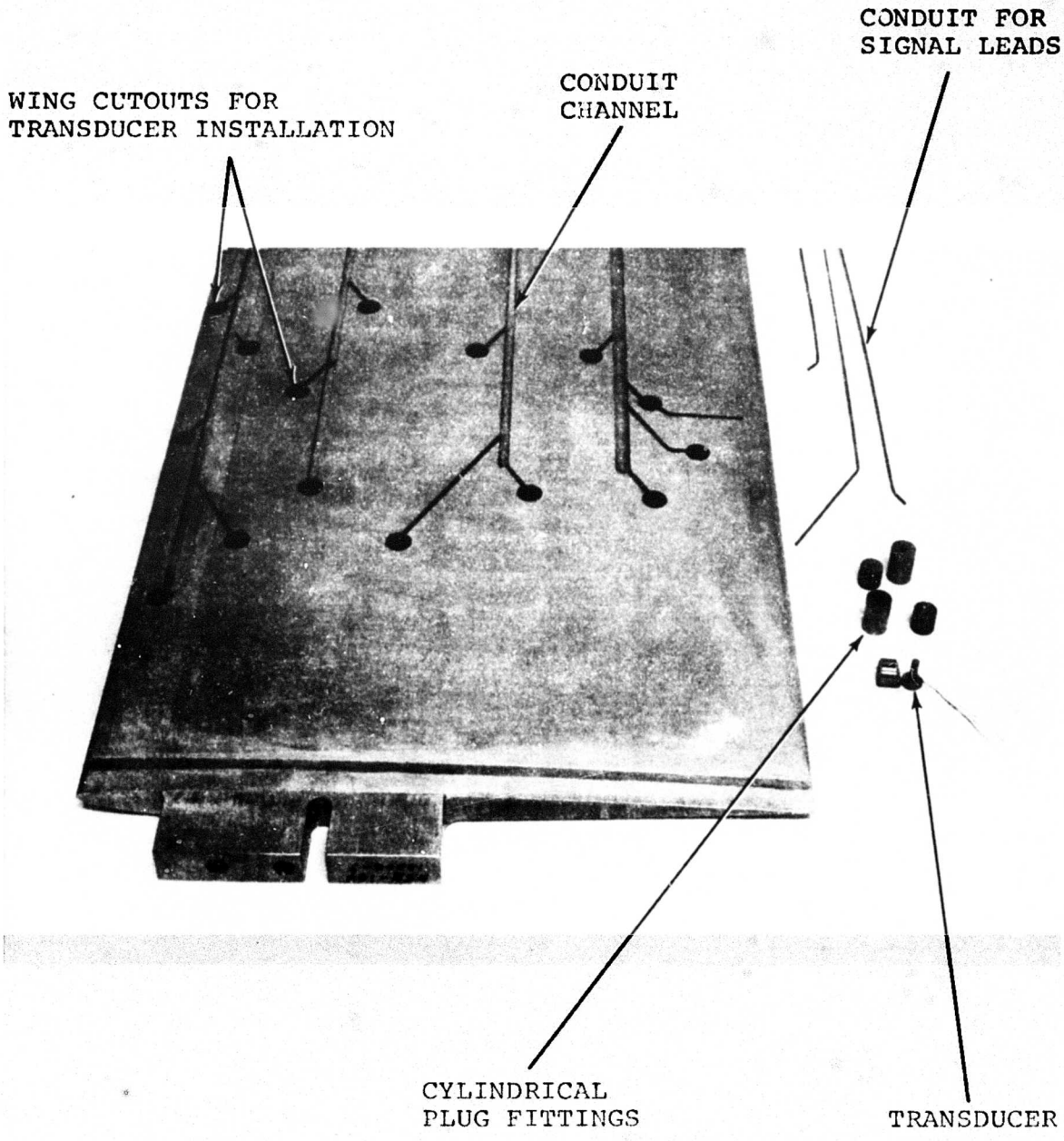

Figure 3. Airfoil Model Construction Details.

DATA RECORDING AND REDUCTION SYSTEM

The complete data recording and reduction system is shown schematically in Figure 4. The data recording, on-line oscillograph, and X-Y plotter presentation were controlled automatically during test runs through the tunnel operating console. After analysis and editing of the oscillograph records, all further data reduction was done off-line at the Vertol Division.

Data Recording

All test data, including both airfoil pressures and tunnel operating condition information, were recorded simultaneously by a pair of Sangamo Model 3500 FM wideband, 14-channel tape recorders. A time code signal and a flywheel 1/rev pulse were duplicated on both tapes to provide data synchronization. In addition, an Electronic Associates Model TR48 analog computer was used to integrate the differential pressures to provide preliminary on-line values of C_N and C_M, which were recorded for reference.

All test parameters, including C_N and C_M, were recorded simultaneously on oscillograph stripouts for direct data monitoring. A time integral value representing the average aerodynamic cycle damping given by $\oint C_M.d\alpha$ was also included. In addition, an X-Y pen plotter was used on-line to record scaled aerodynamic damping versus α_o, or C_N versus α_o during steady-flow tests. This information formed the basis for planning the detailed execution of a major part of the test program.

Data Reduction

Six hundred and seventy-three different test conditions were recorded and digitally processed, representing a total of more than 8 million digital readings. Each oscillatory test point represented an average of at least 10 individual consecutive data cycles (20 cycles at drive frequencies of 48 Hertz and higher), with approximately 50 points read for each cycle and parameter.

To process this large volume of data, the off-line data reduction system described in Reference 2 was used to convert the analog signals to digital form and to provide all final data output. Two additional corrections were made to the data taken from these tests to account for the significant nonlinear sensitivity characteristics of the transducer units and their response to the pitch accelerations of the model.

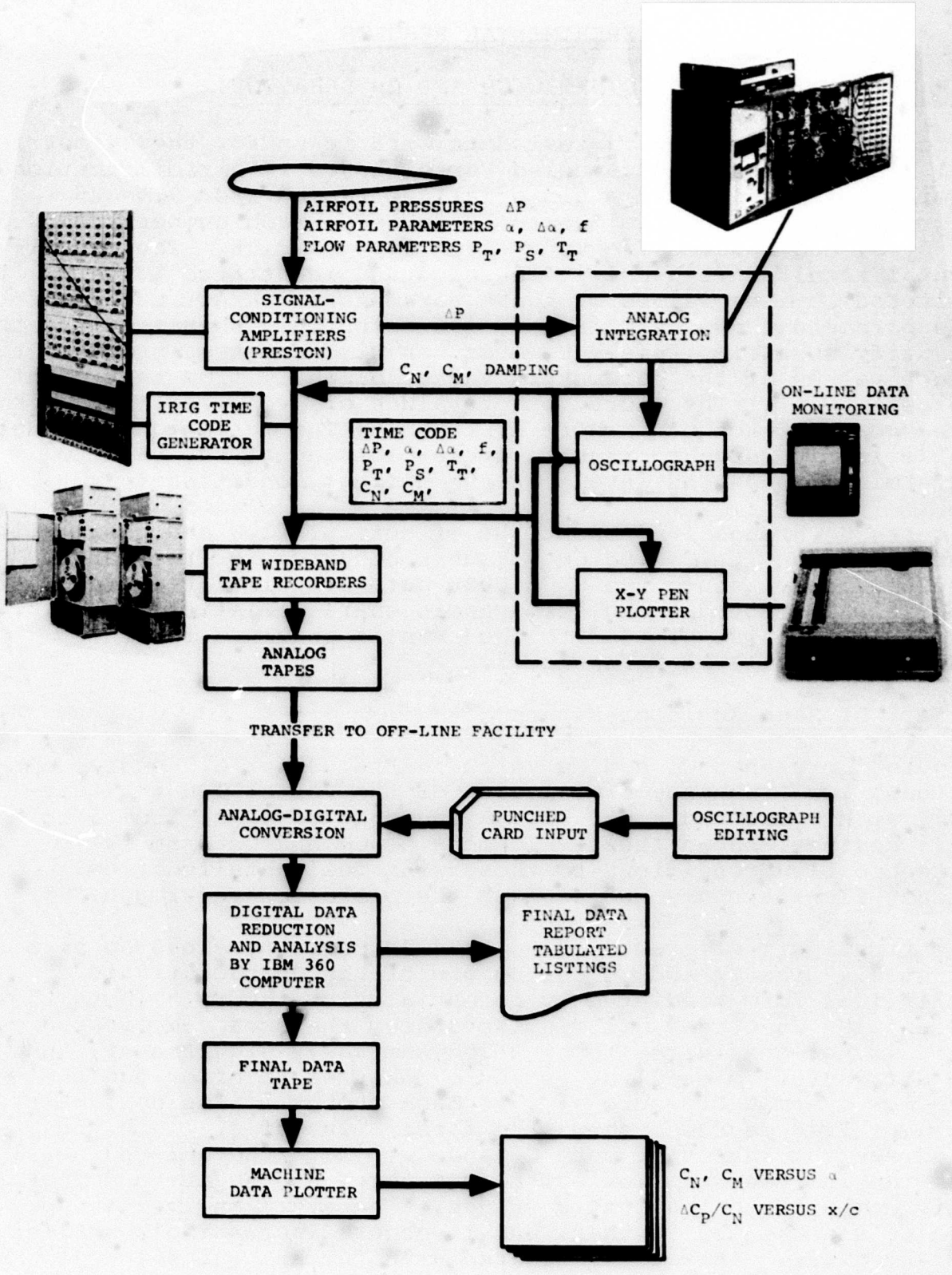

Figure 4. Data Recording and Reduction System.

EXPERIMENTAL RESULTS

PARAMETRIC TRENDS FOR DYNAMIC C_N AND C_M BEHAVIOR

Forced pitch oscillation test data were taken for the symmetrical NACA 0006 and the cambered Vertol 13006-.7 airfoil sections. Nominal values of mean angle of attack ranged from 0 to 25 degrees, amplitude from 2.5 to 10 degrees, Mach number from 0.2 to 0.75, and reduced frequency from 0.04 to 0.66. The experimental results are usually discussed and identified in terms of selected nominal values of these parameters. Exact values of the parameters are used in the discussion only when required to identify specific items. However, as with any test program, the exact values of the parameters varied slightly from test point to test point. Therefore, exact values of M, α_o, $\Delta\alpha$, f, and k are shown on each plot where applicable. The variations are not sufficiently large to require cross-plotting of the data to determine trends and levels at the nominal conditions.

Figures 5 through 10 present the effects of flow and oscillation parameters on the C_N and C_M versus α behavior for the Vertol 13006-.7 only, since the NACA 0006 data are similar except where specifically noted. The aerodynamic characteristics for both airfoils are also similar to the results obtained for the thicker airfoils of Reference 2.

Effect of Mean Angle of Attack

Figure 5 presents C_N and C_M versus α traces for a 5-degree amplitude, low-frequency oscillation of the Vertol 13006-.7 airfoil at M = 0.2 and k = 0.11. A sequence of α_o's, from 5 to 17.5 degrees, shows the development of C_N and C_M from fully attached flow conditions to those with fully stalled flow. Steady-flow data are included on the plots for reference.

The first pair of traces, at α_o = 4.93 degrees, shows no sign of stall. The C_N and C_M curves are of the characteristic elliptical form predicted by potential-flow theory. (Both the C_N and the C_M curves are displaced from the steady-α lines. This is not considered to be aerodynamically significant, and is attributed to baseline pressure measurement error due to the low dynamic pressure at this Mach number.) The next pair, at α_o = 7.48 degrees, shows the first signs of stall in the figure-eight shapes of both C_N and C_M. Note the delayed stall and the increases in maximum normal force and negative moment peak compared to the static values. The stall angle goes up as α_o is increased further, but it occurs increasingly earlier in the cycle. This is associated with further gains in the maximum C_N, which reaches a peak for α_o = 14.82 degrees. When α_o is increased to 17.31 degrees, the minimum angle of attack during oscillation is now above the static stall value and is too high for there to be a complete recovery to attached flow.

characteristics. Consequently, there are reductions in maximum C_N and in the amplitudes of the C_N and C_M excursions, although they remain approximately centered on the steady data.

Effect of Pitching Frequency

Figure 6 shows a sequential set of C_N and C_M traces at increasing frequency for the Vertol 13006-.7 airfoil at M = 0.2, $\Delta\alpha$ = 5 degrees, and α_o = 10 degrees. The most visible trend with frequency is the increased postponement of stall effects, evidenced by the overshoot behavior of both C_N and C_M in comparison to the superposed steady-flow characteristics.

The C_M break at stall occurs initially during the increasing-α part of the cycle. The stall effect is delayed as frequency is increased until, at k = 0.351, it occurs at the point of maximum α in the cycle. Further increases in frequency result in a progressive postponement into the decreasing-α portion of the cycle. Potential-flow C_M ellipses at the lowest and highest frequencies are given for comparison.

The area enclosed by the C_M trace is proportional to the work per cycle (or "cycle damping") and has important physical significance. The net work done by the airfoil on the surrounding air is proportional to the integral

$$W = -\oint C_M \, d\alpha. \qquad (1)$$

The damping is positive for a counterclockwise circuit. Areas enclosed by a clockwise circuit are damped negatively; i.e., the airfoil system extracts energy from the airstream. This can lead to an increase in the amplitude of oscillation with time for an elastic system, and it is precisely the condition for flutter.

The C_M traces demonstrate the effect of stall delay on the aerodynamic damping. As the α for C_M stall increases to the maximum value, the net area contributing to negative damping also grows to a maximum. At higher frequencies, the C_M break occurs <u>after</u> maximum α. This creates a counterclockwise end loop, whose growth ultimately leads to net positive damping.

Up to the frequency where the C_M break occurs at the maximum α, C_{NMAX} occurs after the C_M break and coincides approximately with the negative moment peak. At higher frequencies, the C_{NMAX} position reverts to a point where α is still increasing. This is consistent with potential flow theory, as shown for the case at the highest frequency.

Note that C_N tends briefly to move toward a more positive value at the moment when C_M breaks in the negative direction. This behavior, which will be discussed later in terms of pressure distribution data, indicates that a vortex is shed from the leading edge at the moment of flow separation.

Effect of Pitch Amplitude, Maximum α Fixed

The C_N and C_M traces for three different amplitudes of oscillation at M = 0.2 and k = 0.11 compare the stall behavior at constant maximum α in Figure 7. Since the nominal frequency of oscillation is the same for each case, the differences in the C_N and C_M characteristics are the result of pitch rate effects, $d\alpha/dt$ being proportional to $\Delta\alpha$.

$C_{N_{MAX}}$ increases noticeably with increasing amplitude. In addition, the angles of attack for C_M stall break and for $C_{N_{MAX}}$ are higher at increasing amplitude and do not correspond to a fixed α increment above the static stall value. These effects are similar to those induced by frequency increases, as discussed earlier.

Effect of Mach Number

To illustrate the effects of Mach number on stalling characteristics, Figure 8 presents three sets of C_N and C_M traces at different parametric conditions for Mach numbers of 0.2 and 0.4.

The first set of traces, at f = 12 Hertz (scale 1/rev frequency), α_o = 10 degrees, and $\Delta\alpha$ = 5 degrees, shows reductions in the $C_{N_{MAX}}$ and α for stall with an increase in Mach number. In addition, the C_N and C_M loops are smaller. These changes, however, must be ascribed to the effect of the reduction of reduced frequency (k) by inference from the second and third sets of curves.

The second set of curves illustrates the comparative behavior with Mach number at nearly constant reduced frequency. In this case, close similarities in the maximum excursions of the C_N and C_M behavior are evident. However, the pitching moment traces do indicate an earlier inception of stall at the higher Mach number condition, which substantially reduces the net area of the C_M loop. This is coupled with only small changes in the C_N trace close to the position of $C_{N_{MAX}}$.

A comparison of Mach number effects at the same k but with a better match of the stalling behavior is presented in the third set of traces. Here, α_o is reduced by 2.5 degrees for the M = 0.4 case. The traces show a remarkable similarity in shape, which emphasizes the sensitivity of the stalling to Mach number, allowing for the expected displacement due to the difference

in α_o. (These strong similarities do not persist much beyond M = 0.4, because of the influence of transonic flow on the stall process, as will be made clear later. For C_N and C_M traces at M = 0.6, the reader is referred to Volume II, Figure 1.)

Effect of Leading-Edge Design

Figure 9 presents a comparison of the dynamic C_N and C_M behavior between the Vertol 13006-.7 and NACA 0006 airfoils at M = 0.2 and f = 12 Hertz (equivalent 1/rev frequency). Note that the α for C_M stall break is about 3 degrees higher for the Vertol 13006-.7 airfoil, which corresponds closely to the difference in the steady-flow α for the inception of laminar separation. (See Appendix I for discussion.)

To illustrate the effect of camber and leading-edge radius at higher frequency and Mach number, Figure 10 presents C_N and C_M loops at M = 0.4 and f = 48 Hertz. Because a comparison of the two airfoils at the same α_o would indicate significant dissimilarities in the traces, the α_o has been reduced by 2.2 degrees for the NACA 0006. The similarities between the stalling patterns for the airfoils are striking. The difference in α_o is consistent with steady-flow stalling behavior presented in Appendix I, from which it is inferred that airfoil geometry effects observed in steady flow persist under oscillatory conditions.

Note also that the traces in Figure 10 show a remarkable similarity to those illustrating Mach number effects presented in Figure 8. The most important difference among the traces is the value of α_o.

SUMMARY OF $C_{N_{MAX}}$ AND DAMPING DATA

Maximum Dynamic Normal Force

Figures 11 through 13 show the maximum lift capabilities of the NACA 0006 and Vertol 13006-.7 airfoils. For a realistic comparison of the lift potential of these two airfoils with respect to the flight operating environment of a rotor blade, it is necessary to study behavior in 1/rev motion. Figure 11 shows the dynamic maximum C_N and negative C_M attained at $\Delta\alpha$ = 5 degrees and f = 12 Hertz. The cambered airfoil shows substantially better lift for all Mach numbers tested (0.2 to 0.6). The negative pitching moment maxima are roughly equal. The increase in dynamic maxima with reduction of M is due to the increased reduced frequency.

The effects of the full range of test frequency and Mach number on the maximum C_N values attained during pitch oscillation at $\Delta\alpha$ = 5 degrees are shown for the Vertol 13006-.7 airfoil in

Figure 12 and for the NACA 0006 airfoil in Figure 13. The reduced frequency shows a dominant influence, while Mach number effects are present, but weaker.

The effect of Mach number on dynamic stall is to decrease the maximum attainable C_N by about the same order of magnitude as under steady-flow conditions, except at M = 0.2. At M = 0.2 it was apparent that α_o's higher than those tested here would produce higher maximum C_N's for values of k above 0.44; therefore, these lines represent a limit due only to the scope of testing. The data trend differences which are apparent at M = 0.2 are attributed to the virtual absence of compressibility effects; here, the cambered airfoil shows significantly better maximum lift at k = 0.11.

Aerodynamic Pitch Damping

Principal pitch damping characteristics for the Vertol 13006-.7 airfoil are shown in Figures 14 through 16. Pitch damping is expressed as a ratio to the theoretical potential-flow damping, the derivation of which is based on unsteady aerodynamic theory[4] and has been documented in Reference 2.

Figure 14 presents the variation of pitch damping with frequency at M = 0.2 and $\Delta\alpha$ = 5 degrees. Correspondence with potential-flow damping is indicated by a pitch damping of unity, and fair agreement is obtained until destabilizing effects due to stall appear. As the frequency is increased, this destabilization is postponed to higher values of α_o, as pointed out in previous discussion of the parametric trends.

Consideration of practical rotor blade operation indicates that the aerodynamic damping characteristics are most important at a frequency corresponding to the blade's first torsional mode and at relatively small amplitude. Figure 15 gives the variation of pitch damping with Mach number for f = 48 Hertz (corresponding to a typical blade torsional natural frequency) and $\Delta\alpha$ = 2.5 degrees. Both the amount of negative damping and the α_o at which it appears are reduced for increasing Mach number until compressibility effects eliminate negative damping altogether, as at M = 0.6 and above.

Because of the nonlinear nature of stall, the damping can be expected to vary with amplitude. This is clearly shown in Figure 16 for data at 2.5 and 5-degree amplitudes and f = 48 Hertz. Destabilizing effects begin at a higher α_o for $\Delta\alpha$ = 2.5 degrees, but the magnitude of the negative damping is larger.

The mean angle of attack at which the damping goes through zero defines a "stability boundary", beyond which pitch oscillations may occur. Figure 17 presents stability boundaries on the

M - α_o plane for the Vertol 13006-.7 airfoil to show the effect of 2.5 and 5-degree amplitudes at two frequencies, corresponding to the rotor blade 4/rev and 6/rev motions. Mach number effects limit areas of negative damping to M < 0.6 at the lower frequency. An increase in frequency leads to an enlargement of the region of instability and delays any beneficial compressibility effects until Mach numbers greater than those tested. Note that the lower stability boundary is not strongly sensitive to amplitude. Instability generally appears at a lower α_o for the larger oscillation.

A comparison of the stability limits for both airfoils at 4/rev equivalent frequency is presented in Figure 18. The NACA 0006 section generally has stability boundaries at reduced α_o's for oscillatory amplitudes of both 2.5 and 5 degrees. This is consistent with the effects of leading-edge design discussed previously. In addition, compressibility effects appear sooner; this is a result of the sharper leading edge and is substantiated by the steady-flow results of Appendix I.

DISCUSSION OF STALL AND REATTACHMENT PROCESSES

Considerable insight into the flow processes governing dynamic C_N, C_M, hysteresis, and damping effects may be derived from study of details of the aerodynamic loading. To provide a background for comparison with the dynamic results, it is essential first to examine the variation of chordwise loadings experienced under steady-flow conditions.

NOTE: The chordwise pressure distribution plots presented in Figures 21 through 27 have been normalized by dividing ΔC_p by C_N for clarity.

Chordwise Loadings Under Static Conditions

Figure 19 indicates the progressive variations in the static chordwise loading distributions which characterize stall development on the Vertol 13006-.7 airfoil within the range of test conditions investigated. At M = 0.2, the loading is initially of the classical potential-flow type with a high suction pressure peak at the leading edge, as shown for α = 10.2 degrees. The second loading distribution, given at α = 10.6 degrees, corresponds to an angle of attack just above a small, sharp discontinuity in the C_N - α curve (see Figure 36 in Appendix I).

At α = 10.6 degrees the leading-edge pressure peak shows a significant reduction, indicating that a laminar separation bubble has formed. This phenomenon is characteristic of "thin airfoil stall" and is discussed in detail by McCullough and Gault[5]. The sharp leading edge of a thin airfoil results in a strong adverse pressure gradient (just after the peak) too

close to the nose for transition from laminar to turbulent flow to have occurred in the boundary layer. Laminar boundary layers are less resistant to separation than turbulent ones, and separation occurs. However, the very sharpness of the pressure peak implies that the region of strong adverse pressure gradient must be small. Transition to turbulent separated flow and reattachment of the boundary layer then result. The gradual enlargement of this separation bubble with increasing α prevents further discontinuities in C_N and C_M as α increases. The loading distribution on the fully stalled airfoil (shown at α = 16.6 degrees) is almost flat, with only a small peak at the leading edge.

Next, consider the loadings at M = 0.6, where a very different behavior is evident. Loadings are shown for angles of attack at α = 8.4 degrees and α = 9.1 degrees, which are just below and above the point where deviation from the linear lift slope occurs (see Figure 36 in Appendix I).

At a Mach number of 0.6, the Cp corresponding to local sonic velocity is -1.3. Assuming the most conservative pressure loading on the lower surface (Cp = +1.11), the peak Mach number on the upper surface must be almost 1.5. This implies that the flow around the nose is a supersonic expansion, which eliminates the strong adverse pressure gradient noted for the M = 0.2 condition. Recovery to subsonic flow must then be achieved by a shock or by a system of weaker compression waves. The boundary layer, by now turbulent, passes through recompression without separating. The flow accommodates to higher α by gradual forward movement and weakening of the shock, without discontinuities in C_N or C_M. In fully developed stall, as depicted by the data for α = 16.6 degrees, the loading has reverted to the type appearing at lower Mach numbers.

The main features of the static loading behavior of the NACA 0006 airfoil are closely similar to those of the Vertol 13006-.7, but the sharper leading edge and the lack of camber lead to their development at lower angles of attack.

Dynamic Effects on Loadings During Pitch Oscillation

Effect of Frequency

Figure 20 presents cycle histories of C_N, C_M, and five selected chordwise ΔCp's for the Vertol 13006-.7 airfoil oscillating at 12 Hertz and M = 0.3. The data shown represent the average of ten consecutive cycles of oscillation. Steady C_N and C_M values corresponding to the instantaneous α are also shown for comparison. Note that, even at such a comparatively low frequency, a significant postponement of stall is evident in the C_N and C_M traces.

Figure 21 shows the corresponding sequence of chordwise loading distributions at 20-degree intervals throughout the cycle. The first loading, at an α before stall commences, precisely matches the theoretical steady-flow loading. This is true of all cases where stall is absent. When stall does occur, as at θ = 20 degrees, it is initiated by collapse of the leading-edge ΔC_p, and this effect is rapidly transmitted toward the trailing edge. The loadings shown between θ = 80 and θ = 140 degrees are characteristic of fully developed stall. Recovery from the stall condition begins at the leading edge, with a return of the distribution to the theoretical shape, as shown for θ = 140 through 180 degrees. The inception of stall and the fully developed stall loadings are similar for all Mach numbers (0.2 to 0.6) tested at this frequency. The corresponding data for the NACA 0006 behave in the same manner.

The effect of increasing the frequency of oscillation to 68 Hertz is shown in Figures 22 and 23, which are directly comparable to Figures 20 and 21. The difference in dynamic effects is striking. In Figure 22 it is seen that a marked increase in the stall delay has resulted in a nearly sinusoidal C_N trace, and the C_M break characteristic of the lower frequencies no longer exists. Furthermore, interesting differences in the development of the stalled flow are indicated by the loading data.

The sequence of chordwise loading plots in Figure 23 shows that stall begins at the leading edge. A wavelike bulge (presumably due to a low-pressure zone on the upper surface) then appears just aft of the leading edge and moves slowly downstream. (Its rate is about 0.1 chord per 20-degree interval. At this reduced frequency, the free-stream wind velocity corresponds to 0.44 chord per 20-degree interval.) It is likely that the phenomenon responsible is a free vortex shed from the leading edge when flow separation first occurs, and which then drifts downstream in the "wind shadow" of the airfoil.

The loadings at θ = 340 degrees (i.e., -20 degrees), 0 degrees, and 20 degrees show noticeable deviations from the steady-flow theoretical line, though no signs of stall are present. These deviations are attributed to the pitching motion which, at this point, effectively adds camber to the airfoil by producing a relative wind component in the downward sense ahead of the pitch axis, and in the upward sense aft of it. The redistribution of loading to be expected therefrom is consistent with the noted deviations.

Effects of Mach Number

Figures 24, 25, and 26 show cycle histories of C_N, C_M, and selected ΔC_p's for M = 0.2, 0.4, and 0.6, respectively, at a nominal reduced frequency of 0.2. The mean angle of attack

is in each case approximately equal to that for steady-α stall, while $\Delta\alpha$ = 5 degrees.

The force and moment data are quite similar for all three conditions. In each case C_N goes about 0.8 beyond the static level, reaching a maximum well after flow separation is indicated by collapse of the loading at the leading edge. At the same time, C_M reaches a minimum value of about -0.3. The recovery process, as indicated by the leading-edge loading, is complete at the 220-degree point in the cycle. Between 200 degrees and 260 degrees, it appears that dynamic loading due to nose-down pitch rate reduces C_N and produces a positive C_M.

Substantial differences are visible only in the loading data, mainly at the beginning and end of the cycle. The maximum local loading is strongly limited by Mach number, declining from ΔC_P = 7.0 at M = 0.2 to ΔC_P = 4.5 at M = 0.6. Transonic flow effects account for this limitation effect, as noted previously.

CYCLE-TO-CYCLE FORCE AND MOMENT VARIATIONS

All data presented elsewhere in this report were obtained by averaging the measurements taken from groups of ten or more consecutive cycles of oscillation. The dynamic response of a rotor blade will, of course, depend on the loads acting over individual cycles. The question of variation from cycle to cycle is therefore of practical importance.

Figure 27 shows typical C_N and C_M traces obtained during four successive cycles of pitch oscillation for the Vertol 13006-.7 airfoil where strong stall effects are present. The variations in both C_N and C_M are negligible where stall effects are absent, as shown by that part of the cycle between stall recovery and inception. During the initial period of stall, C_N and especially C_M show very repeatable behavior. During the stall recovery period, however, a wide variety of patterns may be followed.

Since C_N and C_M behave in a regular manner when attached flow prevails and also when the flow breakdown begins, it may be inferred that the marked scatter in the stalled-flow behavior is not caused by wind tunnel flow turbulence or by variations in the model airfoil motion. Instead, these flow variations during stall recovery are attributed to the presence of large-scale turbulent eddies formed above the airfoil as suggested from the previous discussion of dynamic loadings during stall. The random nature of turbulent flow is well known and can be expected to result in loading variations susceptible only to statistical description.

DRAG IN PITCHING OSCILLATION

Because of difficulties in measuring the instantaneous airfoil drag under unsteady-flow conditions, as reported in Reference 2, only time-average drag values were determined. The average drag in pitch oscillation was obtained by using a slowly traversing pitot-static probe to survey the wake momentum profile.

Drag data were obtained for both airfoils. Measurements for the NACA 0006 airfoil, taken at M = 0.4, are compared in Figure 28 to the steady-flow C_D, which is shown as a dashed line. The oscillatory drag data agree with the trends for thicker airfoils given by Reference 2 and show that the average C_D in pitch oscillation is always higher than the steady level, increasing with frequency between 12 and 48 Hertz. A small part of this increase may be due to the fact that $\Delta\alpha$ increases with frequency because of mechanical effects.

Figure 29 shows drag data obtained for the Vertol 13006-.7 airfoil at M = 0.4 and 0.6. At M = 0.4, the data trends are similar to those for the symmetrical airfoil but show a 2-degree advantage in the angle of attack for the drag increase due to stall, which is consistent with the static behavior. At M = 0.6, oscillatory data were obtained only at a frequency of 12 Hertz.

COMPARISON WITH PREVIOUS RESULTS

Static and dynamic data from this test on the NACA 0006 and Vertol 13006-.7 airfoils are compared in Figures 30 through 33 with the results of a similar series of tests on the symmetrical NACA 0012 (modified) and the cambered Vertol 23010-1.58 sections.

The steady-flow C_N and C_M characteristics are compared at M = 0.4 in Figure 30. Both thick airfoils show the large, abrupt changes in C_N and C_M characteristic of leading-edge stall[5]. This stall is caused by a sudden separation of the flow over the entire upper surface of the airfoil. No appreciable buffeting was observed from the pressure traces for these airfoils below stall. The thin airfoils, on the other hand, show a change in the lift-curve slope but little or no loss of lift, and a comparatively gradual development of the nose-down pitching moment due to stall. (This is characteristic of thin-airfoil stall, as noted above.) Buffeting, detected from ΔCp fluctuations on the analog records, begins before the lift curve changes slope.

Comparisons of the characteristics of the dynamic data can be summarized in terms of two important parameters: the dynamic $C_{N_{MAX}}$ at frequencies corresponding to a typical helicopter rotor 1/rev, and cycle damping at the rotor blade first

torsional natural frequency. For convenience, the cycle damping is divided by the theoretical damping, based on Theodorsen's formulation[4].

Curves of $C_{N_{MAX}}$ versus Mach number are presented in Figure 31. Cycle damping of the four airfoils is compared in Figure 32 for 6/rev pitch motion (k = 0.74) at M = 0.2. The cambered airfoils show a substantial advantage over the symmetrical airfoils, both in the inception and in the magnitude of negative damping at a given α.

The region of instability (based on zero damping) is shown in Figure 33 for an equivalent frequency of 6/rev. Both camber and airfoil thickness are seen to postpone the regions of negative damping to higher angles of attack.

The general reduction in the α_o range of instability with increasing Mach number is due to transonic flow effects. For the thicker airfoils, stall caused by the sudden flow separation on the upper surface at Mach numbers up to 0.5 is replaced by a stable expansion-fan and shock system at higher M. Separation, if present, occurs aft of the shock.

Transonic flow effects appear sooner in the case of 6-percent-thickness airfoils, but they are limited to smaller regions close to the leading edge because of the sharper nose profiles.

COMPARISON WITH THEORETICAL PREDICTIONS

In Figure 34, chordwise loading distributions under steady-flow conditions below stall are compared with theoretical predictions for both airfoils at M = 0.2, where compressibility effects are virtually absent. Data for the NACA 0006 were taken directly from Reference 6, while those for the Vertol 13006-.7 airfoil were developed using the vorticity polygon method of Reference 7. Agreement is excellent in both cases.

The experimental dynamic force and moment derivatives for both airfoils at small α_o values (no stall present) are compared with theoretically predicted data in Figure 35. The theoretical values, based on thin airfoil representation with the effects of compressibility and tunnel walls (method of images) included, were calculated with a computer program supplied by NASA[8]. The data show essentially identical characteristics for each airfoil. The differences between test and theory are similar to the trends noted for thicker airfoils, as reported in Reference 2.

The experimental values of normal force amplitude are slightly lower than predicted. This is consistent with the universally noted reduction in static lift-curve slope caused by viscosity. The trend to higher lift-curve slope as Mach number is increased

is in good agreement with the predictions. The data for lift phase agree very well with the theory, maximum differences being less than 5 degrees.

The pitching moment amplitudes agree well in trends with Mach number but show a reduction in magnitude, similar to that noted for C_N. This reduction is attributed to viscous effects. The C_M phase data show appreciable departure from predictions away from the midranges of reduced frequency, with maximum differences up to 30 degrees. These variations result from the extreme sensitivity of the pitching moment phase to the pitch reference center, coupled with slight shifts of the aerodynamic center from the quarter-chord point for the additional loading due to oscillation.

CONCLUSIONS

1. Thin airfoils oscillating in pitch, at the amplitudes and frequencies typically experienced by blade elements of helicopter rotors, show a strong dynamic postponement of lift and moment stall to higher angles of attack than experienced under steady-flow conditions.

2. Substantial increases in the maximum normal force above steady-flow values are attained during oscillation, and increase with frequency but decline as the Mach number increases to 0.6. Increases in the maximum normal force capability are about equal to those attained by the thicker airfoil sections reported in Reference 2.

3. The Vertol 13006-.7 airfoil stalls at higher angles of attack than the NACA 0006 section. This is consistent with the differences in steady-flow behavior and is unaffected by oscillation frequency.

4. Pitch oscillations at angles of attack where stall takes place can result in net energy inputs from the airflow into the airfoil system. These conditions of negative damping imply the possibility of divergent torsional oscillations in a rotor blade. The inception of negative damping is shifted to higher α_o by increasing frequency, but it occurs earlier as Mach number is increased. At frequencies between 4/rev and 6/rev, corresponding to a typical rotor blade first torsional vibration mode, the width and intensity of negatively damped regions diminish at the higher Mach numbers. At M = 0.6, negative damping at 4/rev frequency has disappeared but is present at 6/rev.

5. The flow processes governing stall development and recovery are initiated by conditions at the leading edge and rapidly progress toward the trailing edge. The character of the chordwise loading during stall and reattachment shows considerable variation over the range of test conditions studied. It indicates that large-scale vortex shedding is induced on the airfoil upper surface, and that its intensity is strongly dependent on the reduced frequency.

RECOMMENDATIONS

1. The data presented in this report should be further analyzed with a view to the establishment of a mathematical description of dynamic stall. An empirical formulation of this type is a necessary first step in the practical application of these data to rotor dynamic and aerodynamic computer analyses.

2. A program of analysis should be undertaken to develop a detailed understanding of the flow processes affecting dynamic stall, such as local supersonic flow and vortex shedding. The program would require supplemental experimental work in flow visualization and the measurement of absolute pressures to define local-flow Mach numbers on the airfoil surfaces.

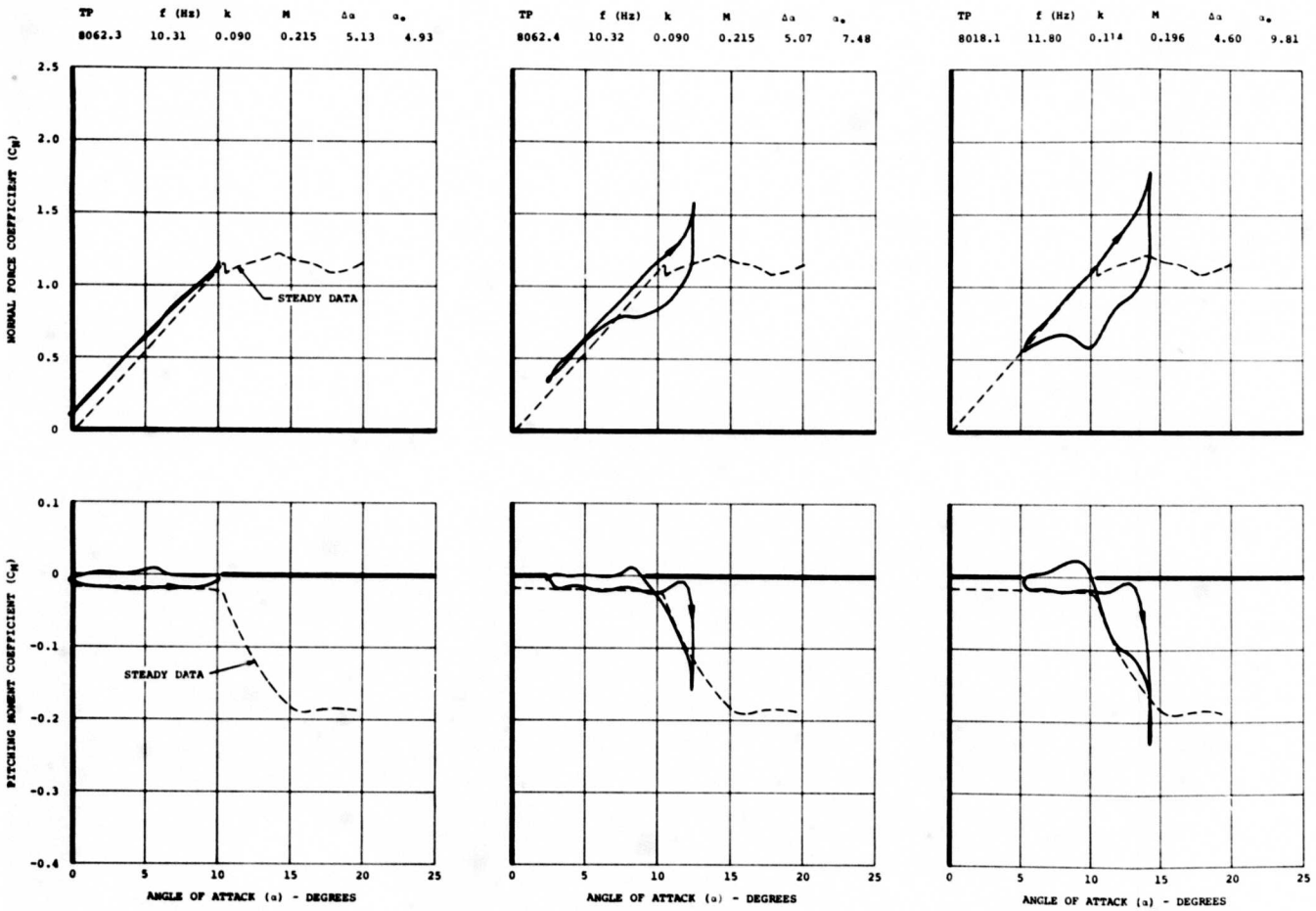

Figure 5. Effect of Mean Angle of Attack on Dynamic C_N and C_M Versus α for Pitch Oscillation of the Vertol 13006-.7 Airfoil at M = 0.2, f = 12 Hertz, and $\Delta\alpha$ = 5°.

M	Δα	α_o
0.196	4.60	9.81

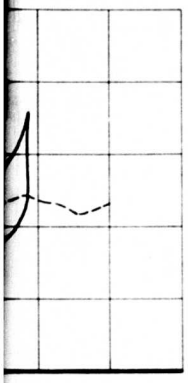

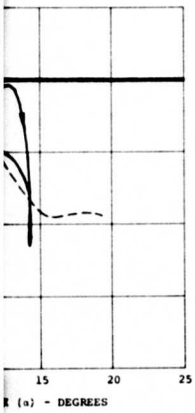

TP	f (Hz)	k	M	Δα	α_o
8018.2	12.00	0.116	0.196	4.50	12.37

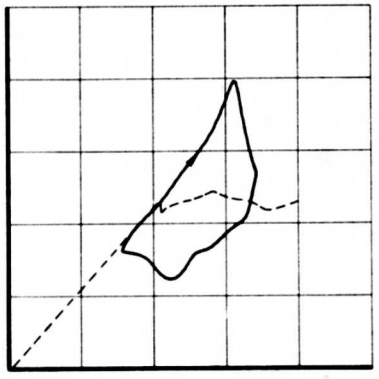

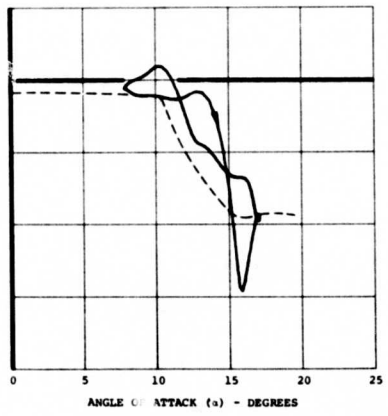

TP	f (Hz)	k	M	Δα	α_o
8018.3	11.92	0.115	0.196	4.54	14.82

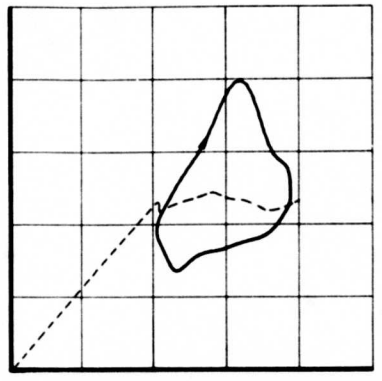

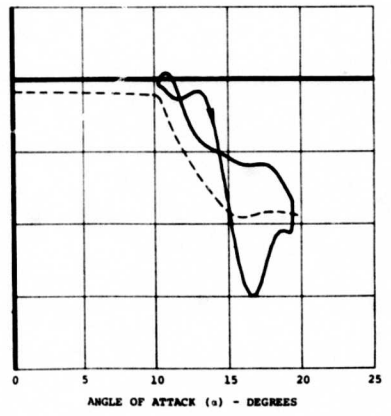

TP	f (Hz)	k	M	Δα	α_o
8018.4	12.05	0.117	0.196	4.59	17.31

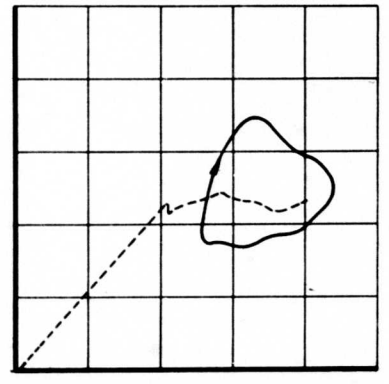

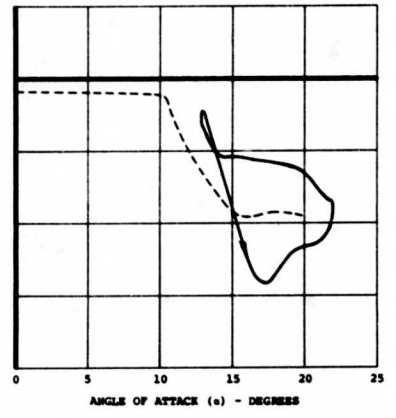

B

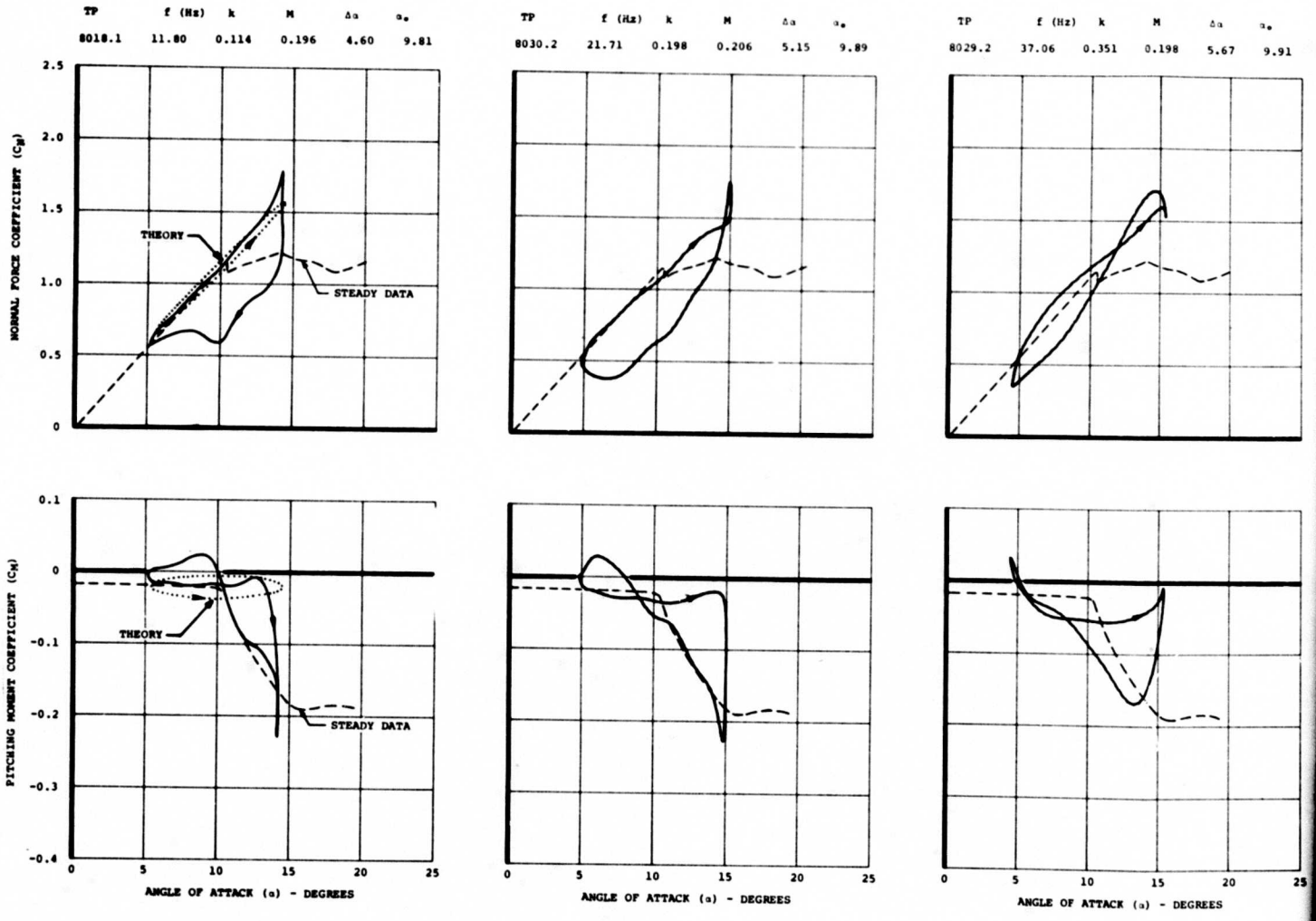

Figure 6. Effect of Frequency on Dynamic C_N and C_M for the Vertol 13006-.7 Airfoil at M = 0.2, $\Delta\alpha$ = 5°, and α_o = 10°.

M	Δα	α_o
0.198	5.67	9.91

TP	f (Hz)	k	M	Δα	α_o
8031.4	49.92	0.467	0.201	5.84	9.87

TP	f (Hz)	k	M	Δα	α_o
8045.1	58.44	0.515	0.210	5.92	10.09

TP	f (Hz)	k	M	Δα	α_o
8047.4	72.70	0.633	0.215	6.78	9.94

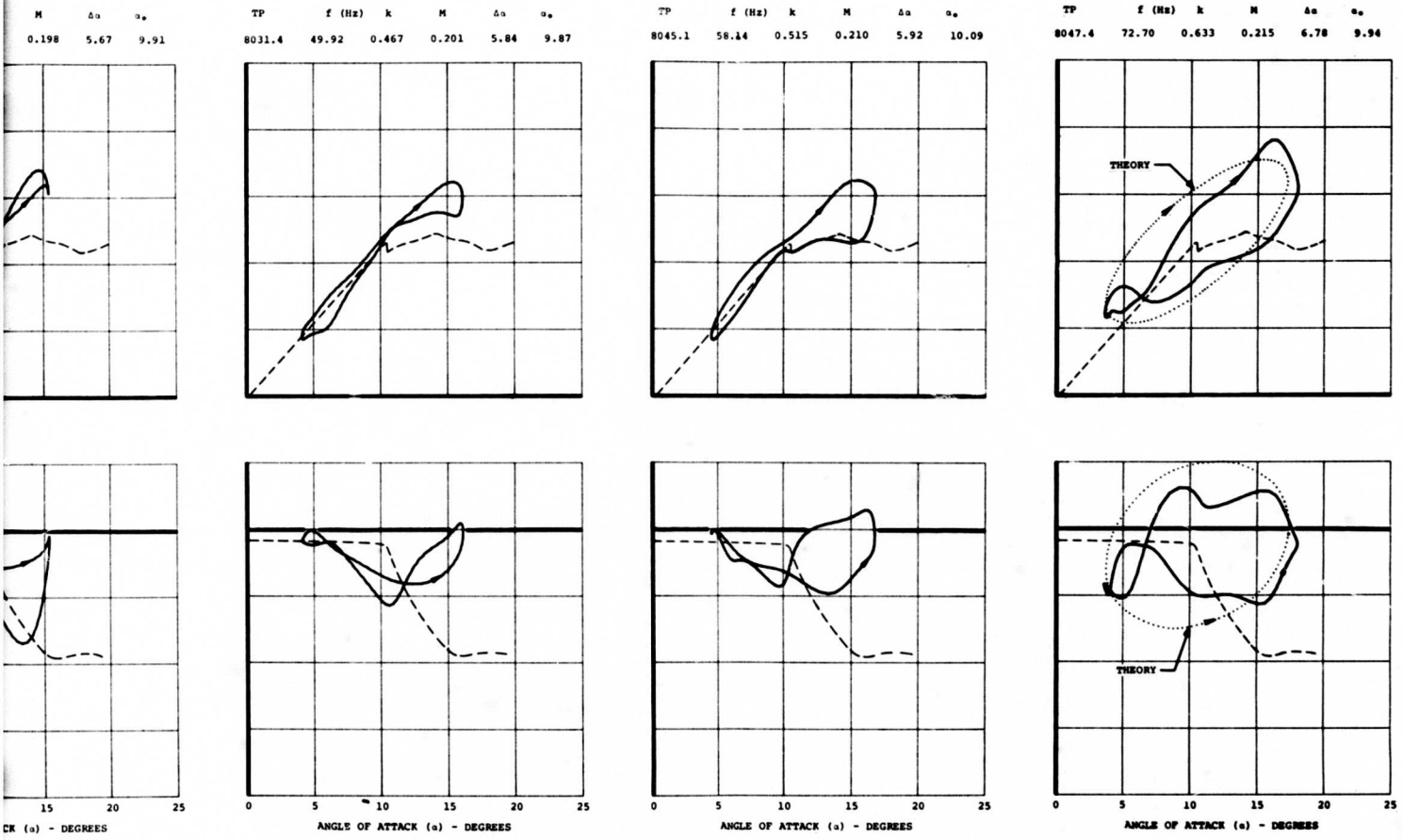

B

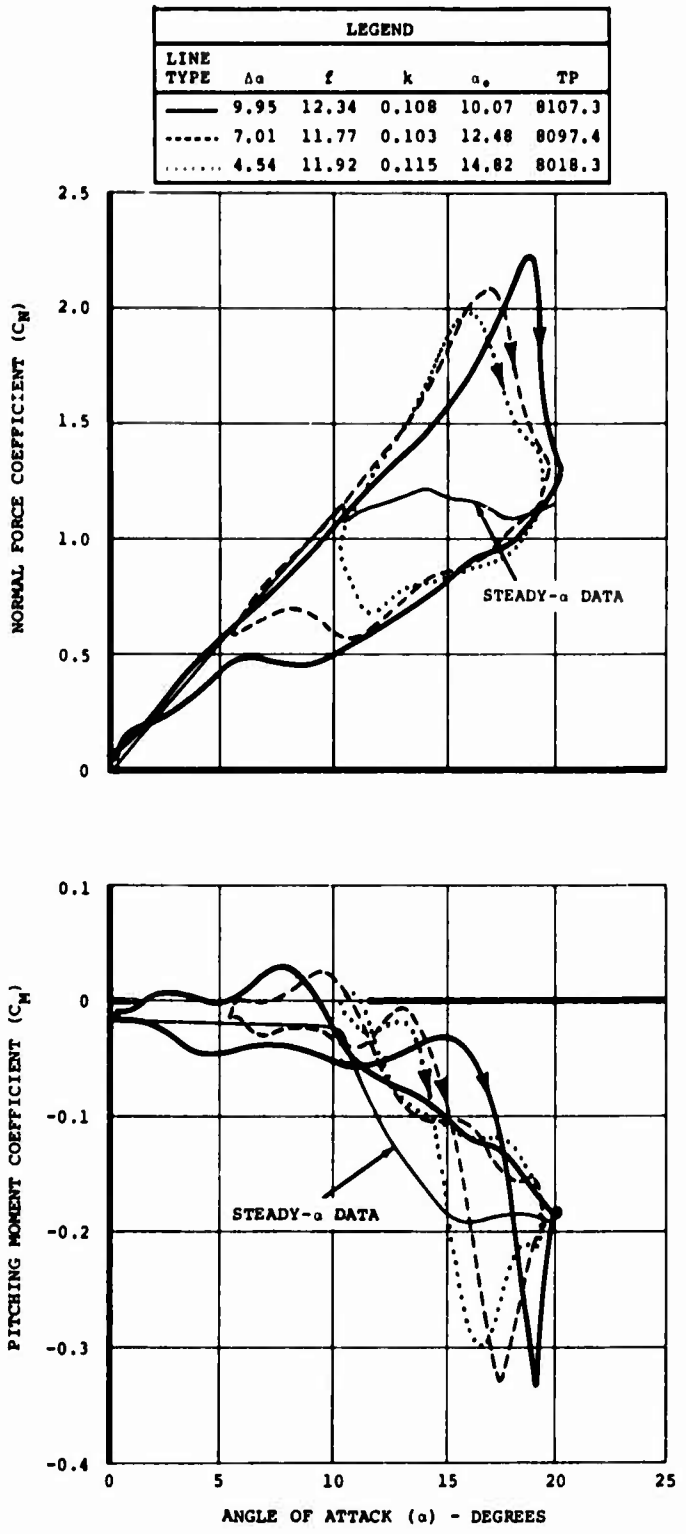

Figure 7. Effect of Oscillation Amplitude on Dynamic C_N and C_M Versus α for the Vertol 13006-.7 Airfoil at M = 0.2, f = 12 Hertz, and Constant Maximum α.

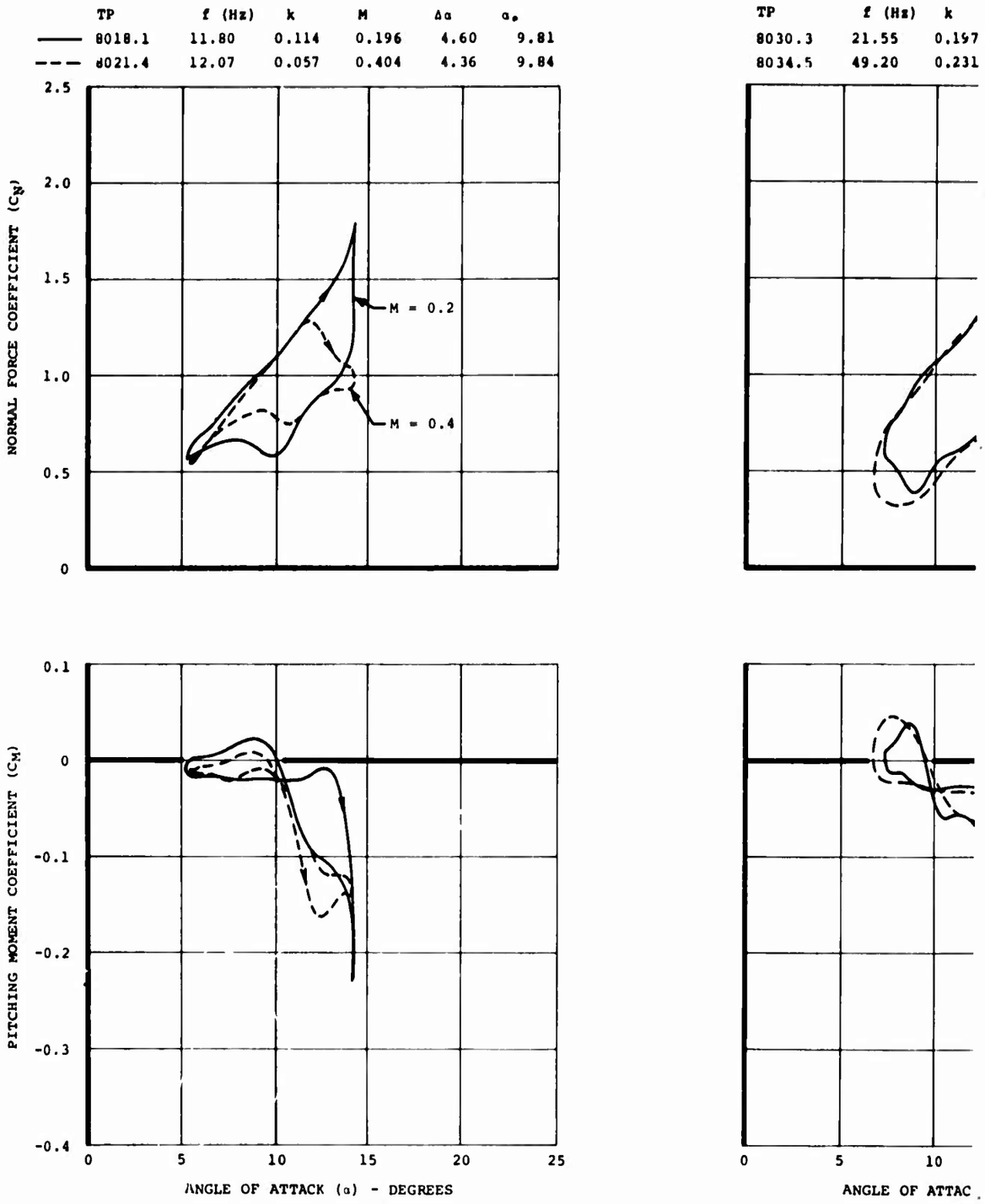

Figure 8. Effect of Mach Number on the Dynamic C_N and C_M for the Vertol 13006-.7 Airfoil at $\Delta\alpha = 5°$.

TP	f (Hz)	k	M	Δα	α_o
8030.3	21.55	0.197	0.206	5.14	12.36
8034.5	49.20	0.231	0.404	5.58	12.36

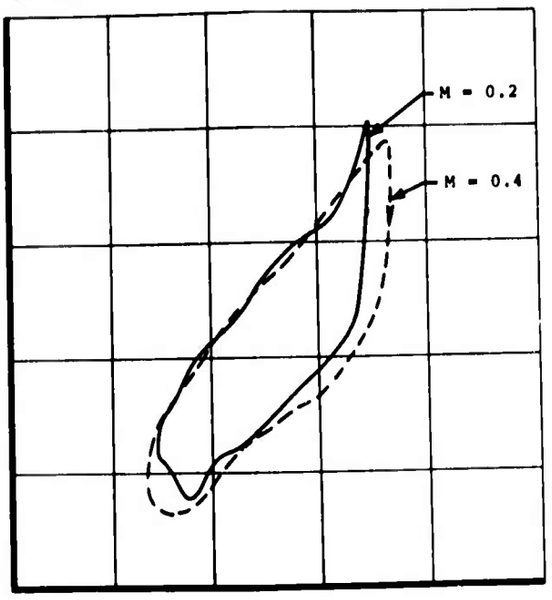

TP	f (Hz)	k	M	Δα	α_o
8030.3	21.55	0.197	0.206	5.14	12.36
8034.4	49.17	0.231	0.404	5.58	9.98

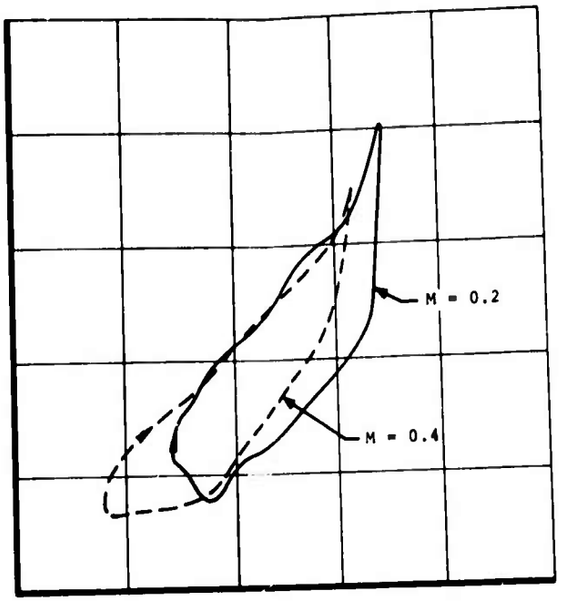

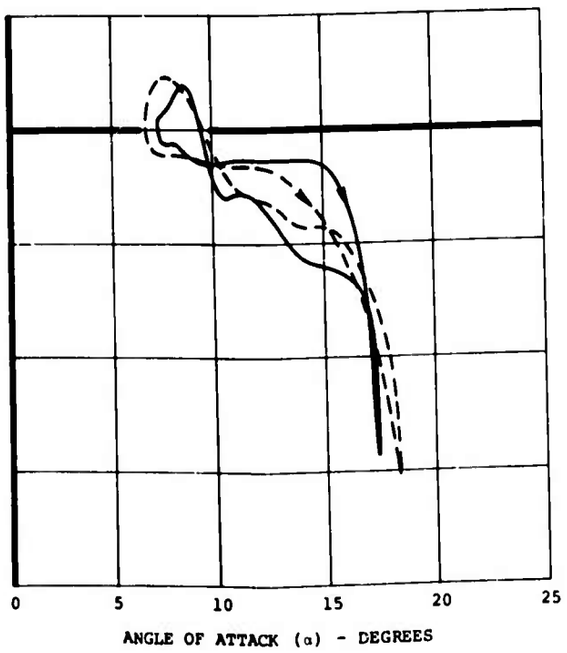

ynamic C_N and C_M
at $\Delta\alpha = 5°$.

B

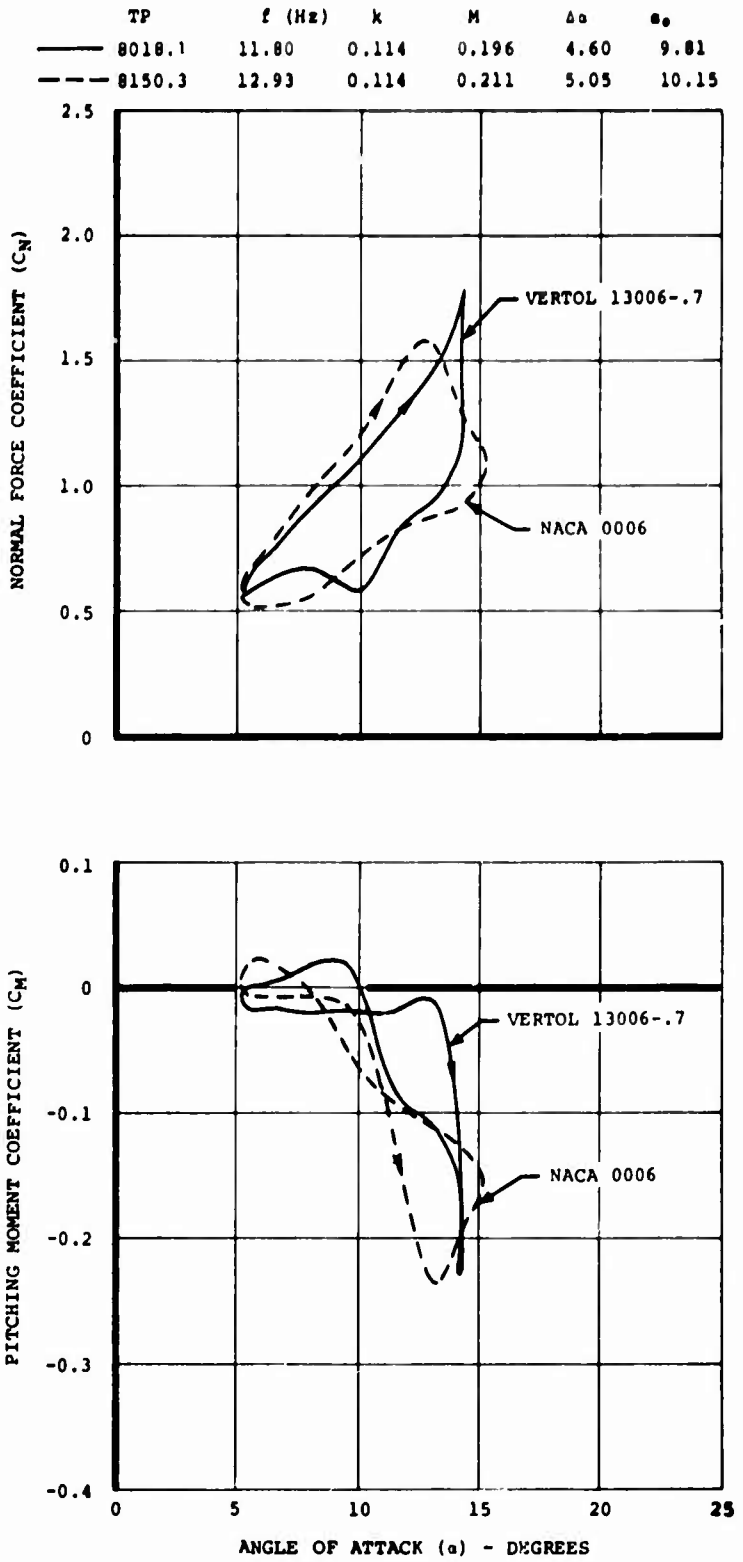

Figure 9. Effect of Leading-Edge Design on the Dynamic C_N and C_M at f = 12 Hertz, M = 0.2, $\Delta\alpha$ = 5°, and α_o = 10°.

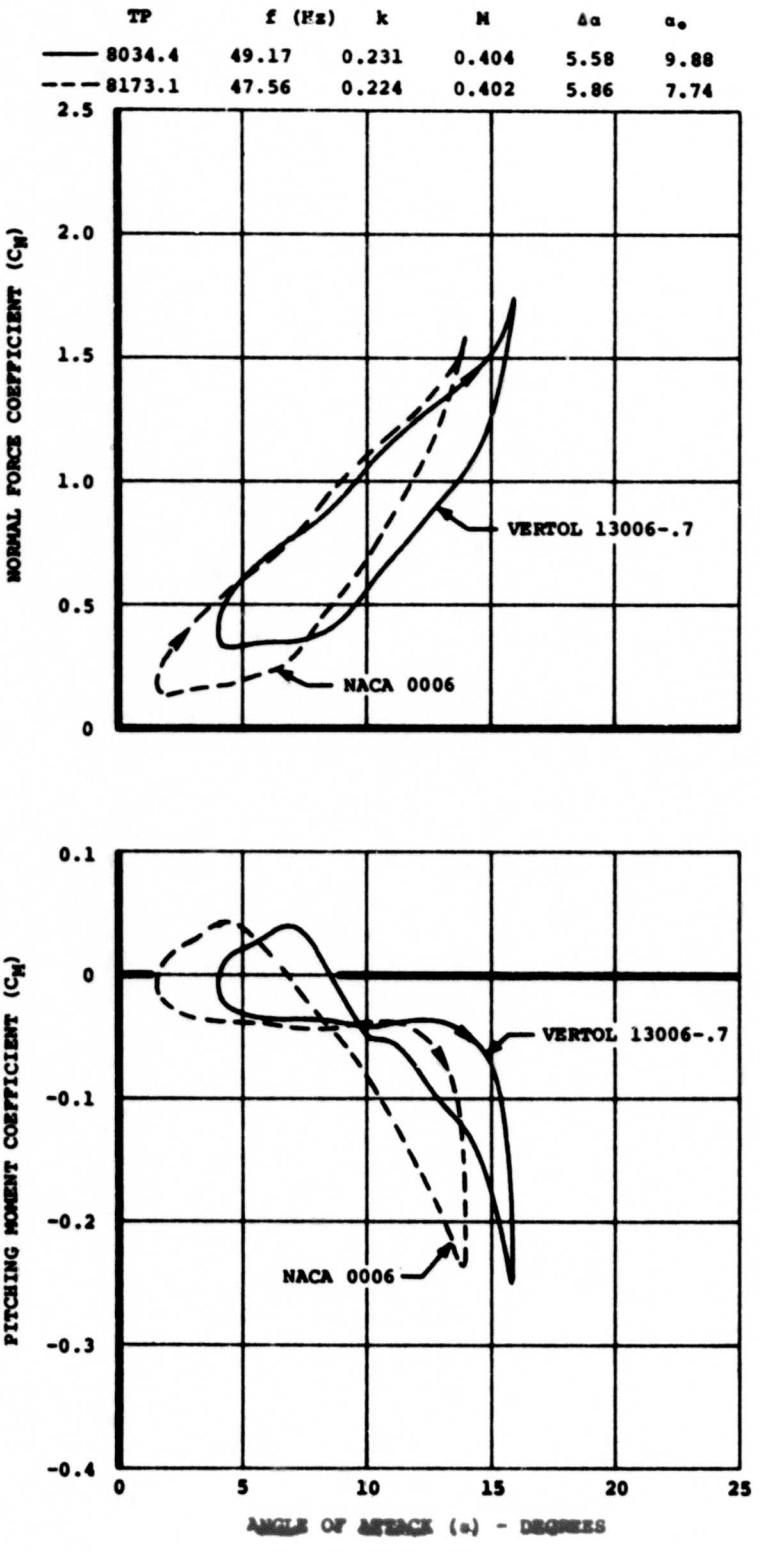

Figure 10. Effect of Leading-Edge Design on the Dynamic C_N and C_M at f = 48 Hertz, M = 0.4, and $\Delta\alpha = 5°$.

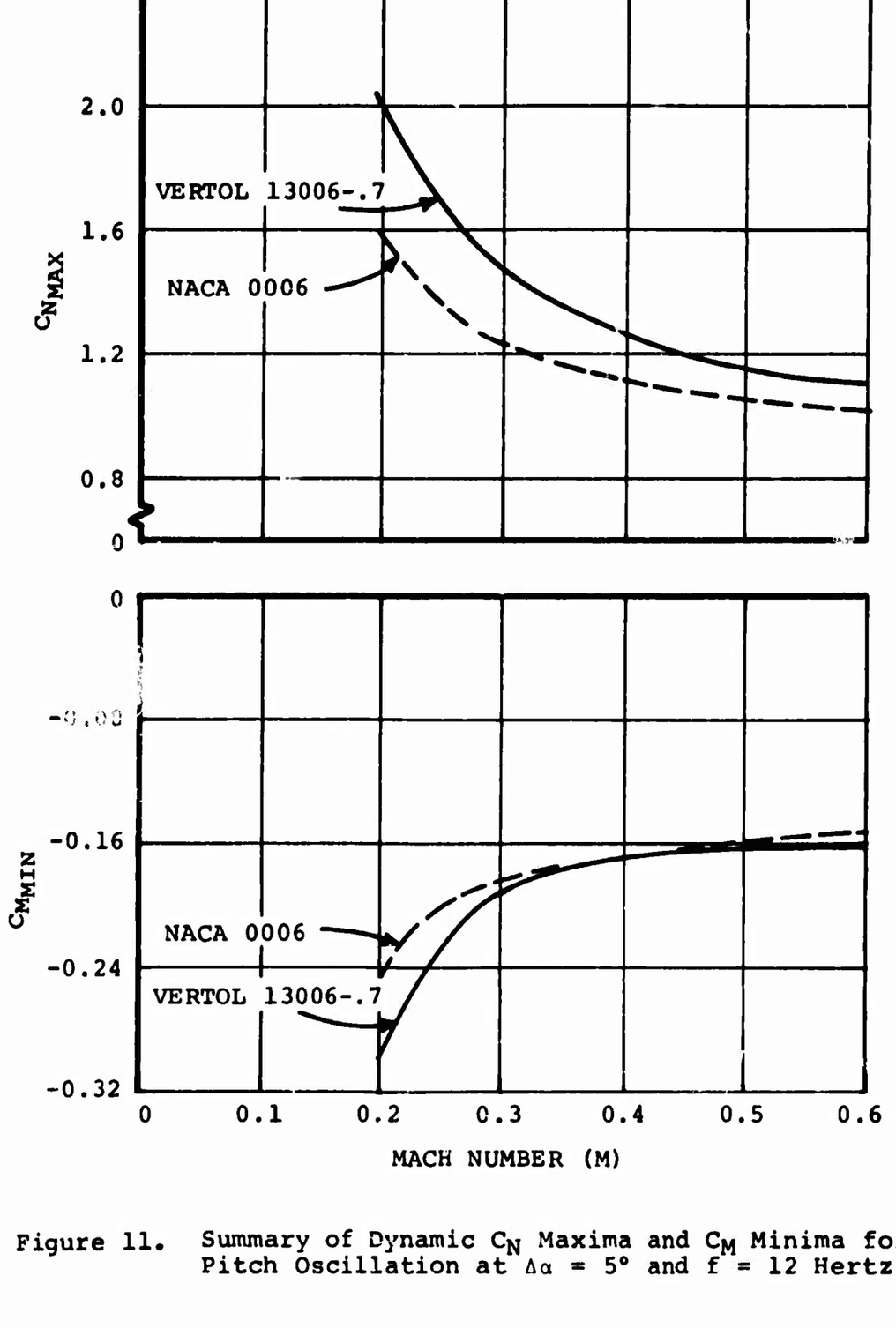

Figure 11. Summary of Dynamic C_N Maxima and C_M Minima for Pitch Oscillation at $\Delta\alpha$ = 5° and f = 12 Hertz.

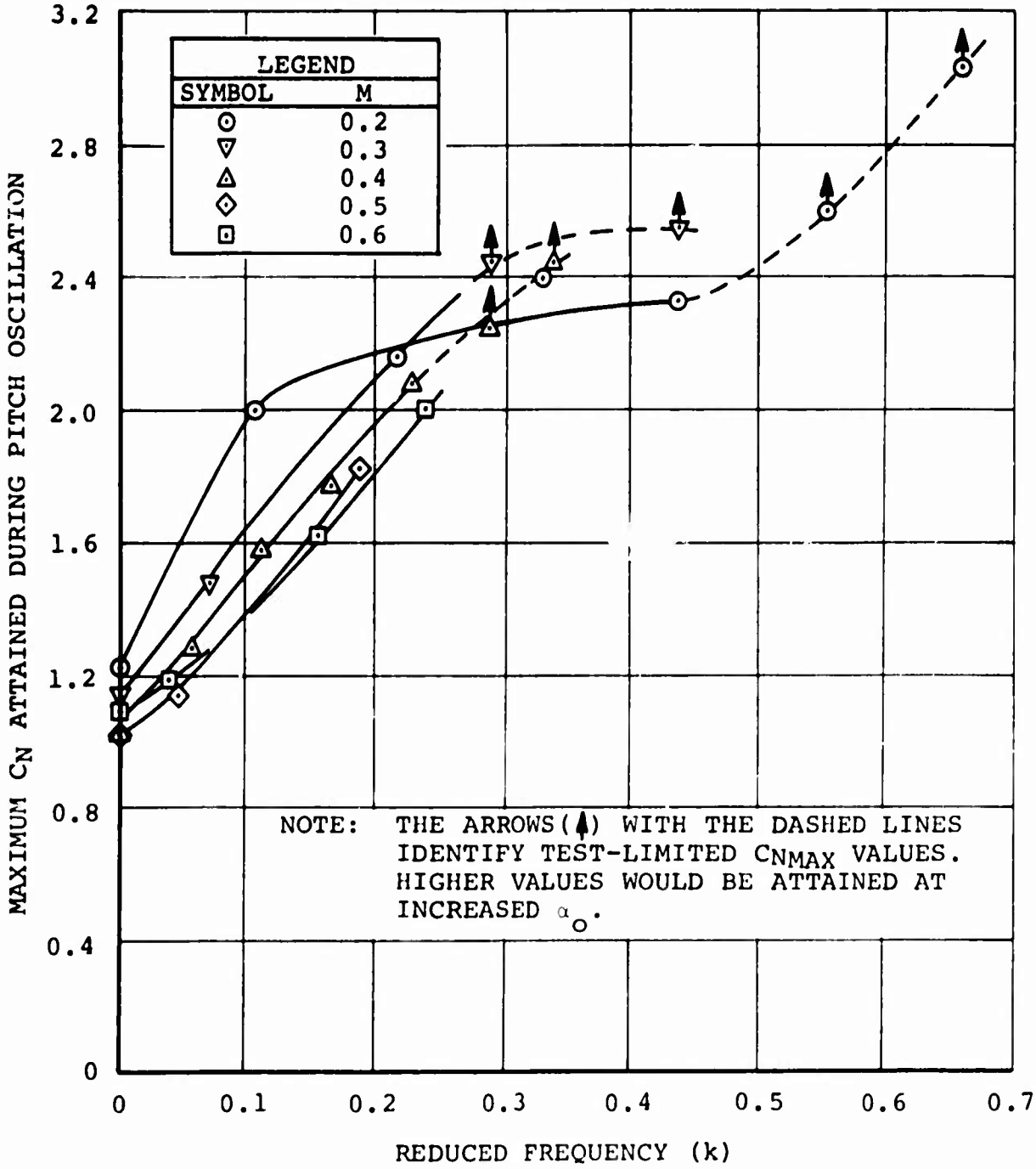

Figure 12. Maximum C_N Attained for the Vertol 13006-.7 Airfoil in Pitch Oscillation at $\Delta\alpha = 5°$.

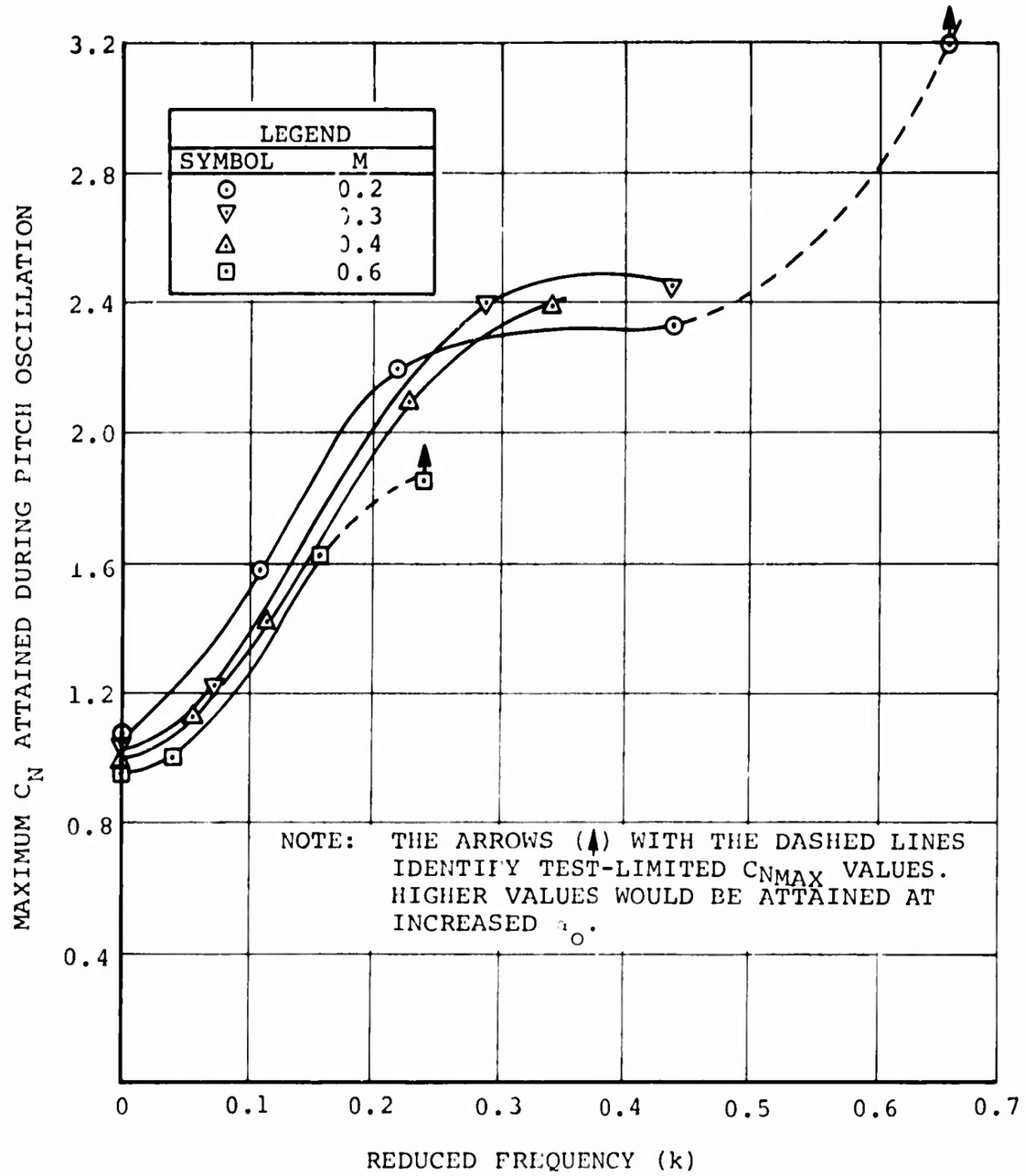

Figure 13. Maximum C_N Attained for the NACA 0006 Airfoil in Pitch Oscillation at $\Delta\alpha$ = 5°.

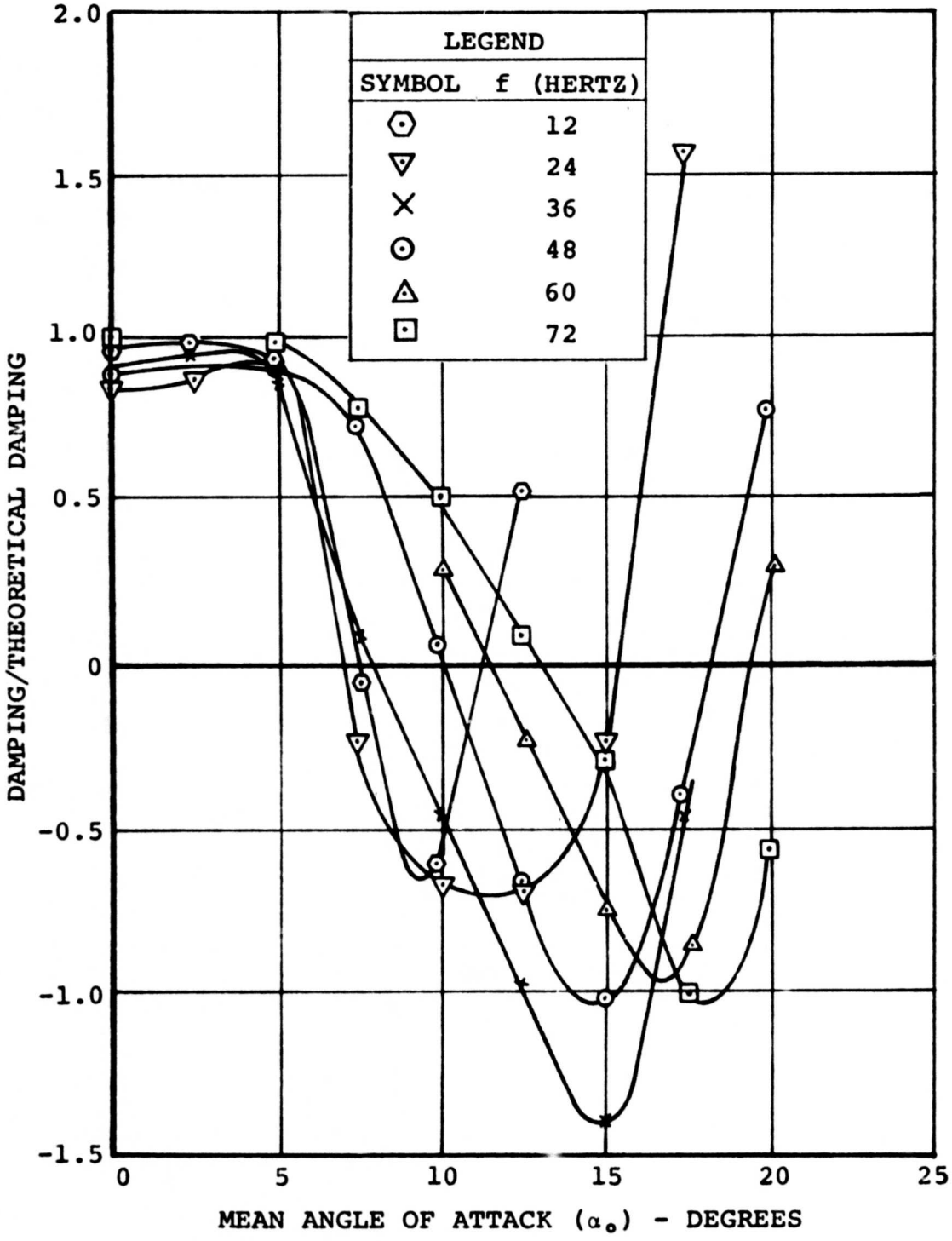

Figure 14. Effect of Oscillation Frequency on Pitch Damping Characteristics for the Vertol 13006-.7 Airfoil at M = 0.2 and $\Delta\alpha$ = 5°.

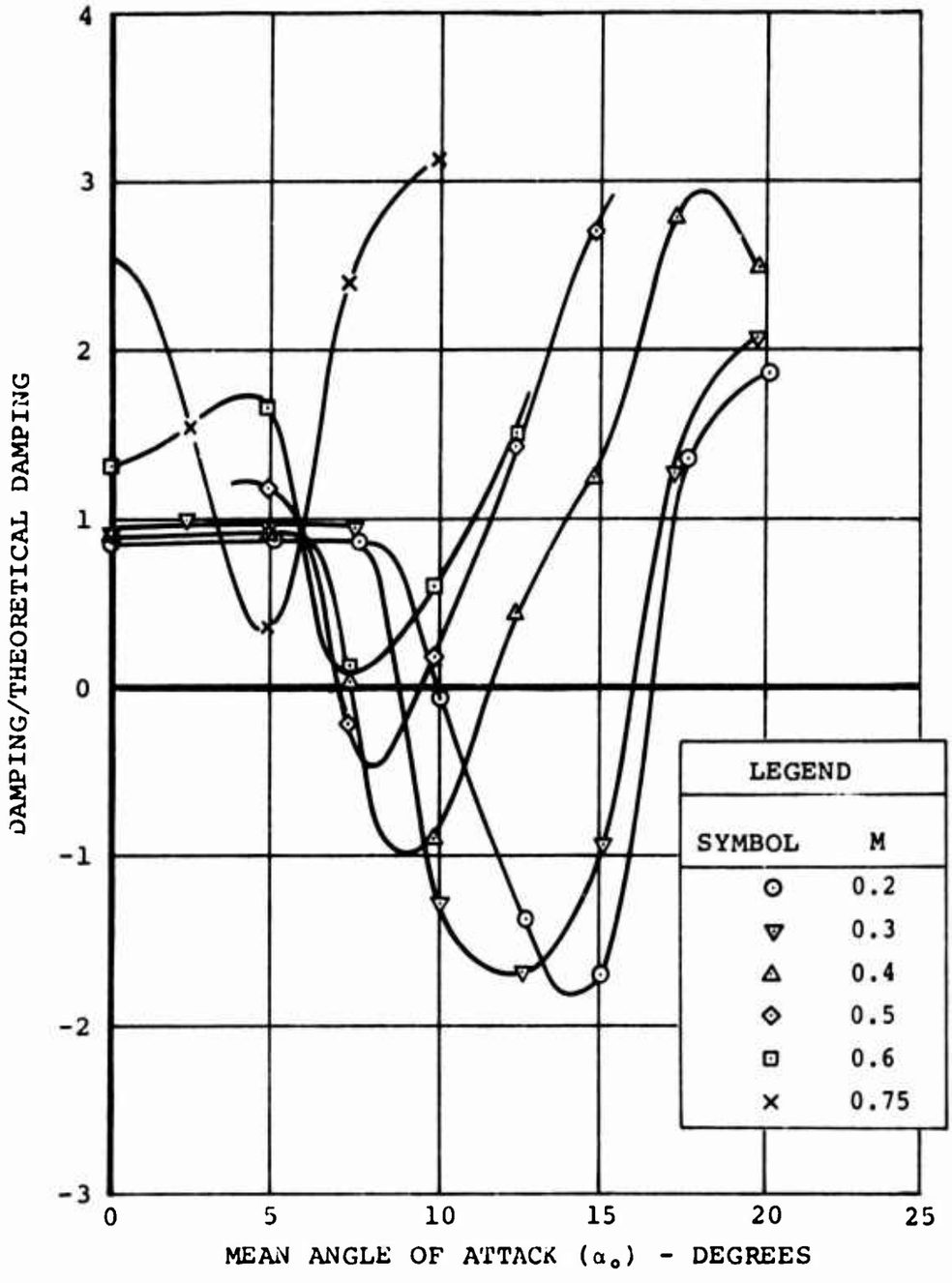

Figure 15. Effect of Mach Number on Pitch Damping Characteristics for the Vertol 13006-.7 Airfoil at f = 48 Hertz and $\Delta\alpha$ = 2.5°.

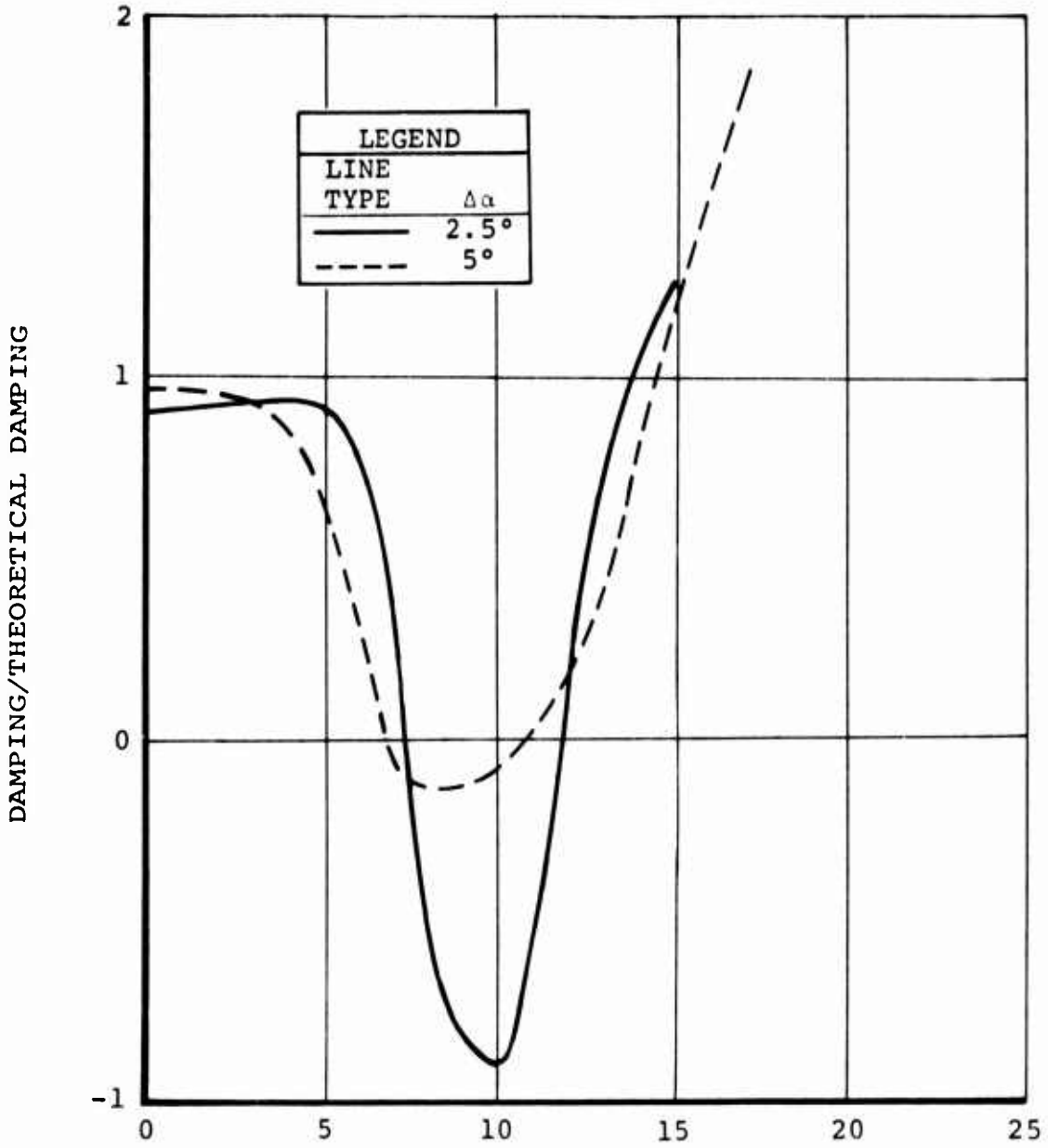

Figure 16. Effect of Oscillatory Amplitude on Pitch Damping for the Vertol 13006-.7 Airfoil at M = 0.4 and f = 48 Hertz.

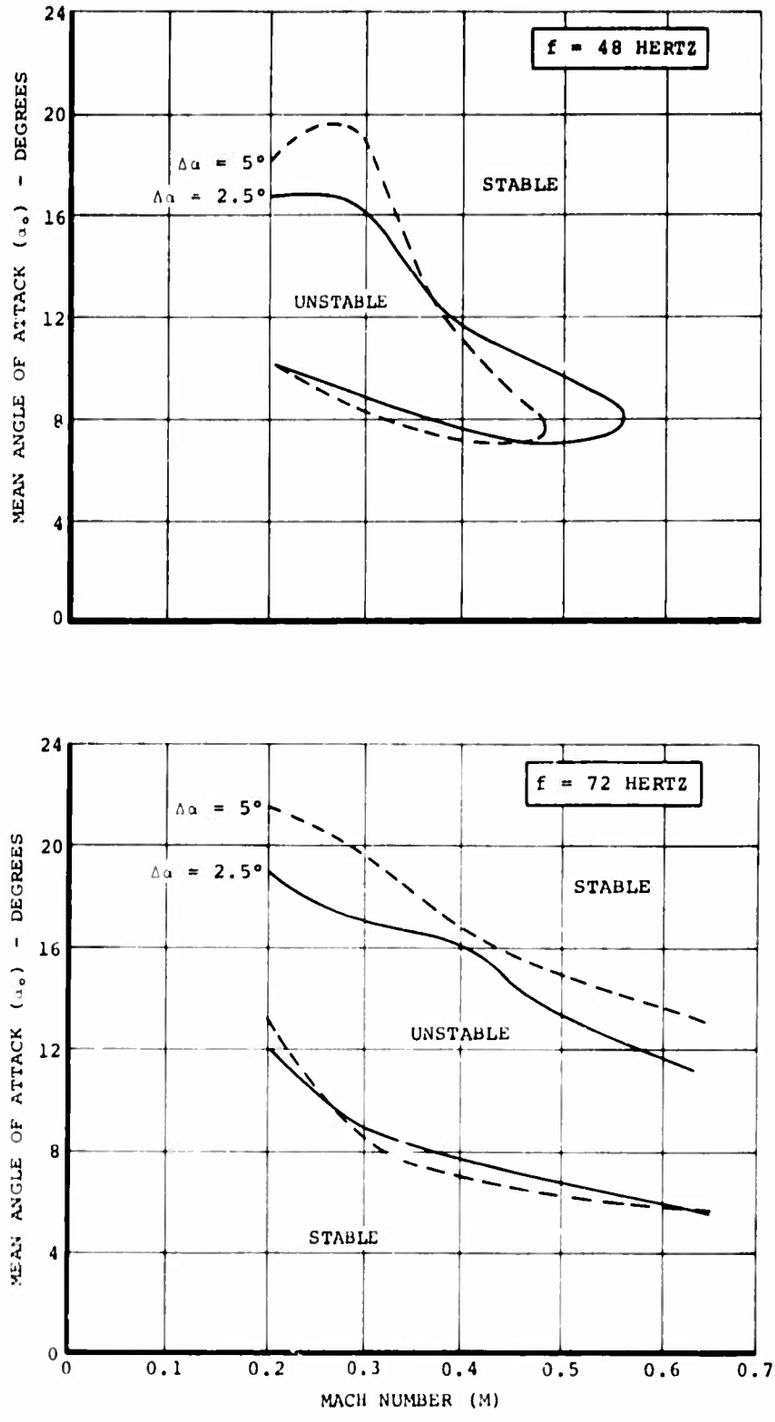

Figure 17. Pitch Damping Stability Limits for the Vertol 13006-.7 Airfoil at f = 48 Hertz and f = 72 Hertz.

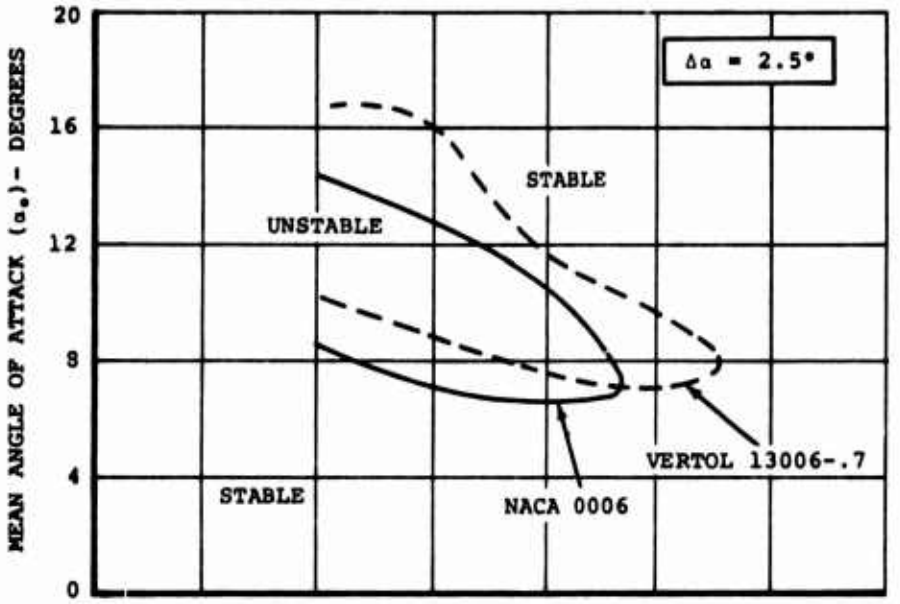

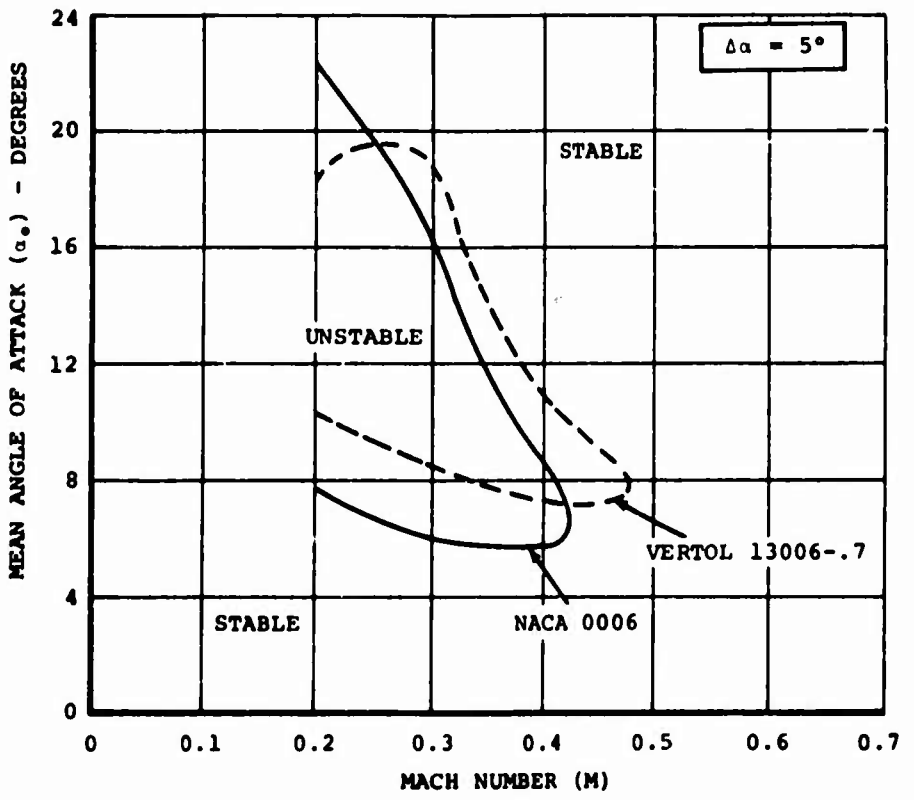

Figure 18. Comparison of Pitch Damping Stability Limits for the Vertol 13006-.7 and NACA 0006 Airfoils at 4/Rev Frequency.

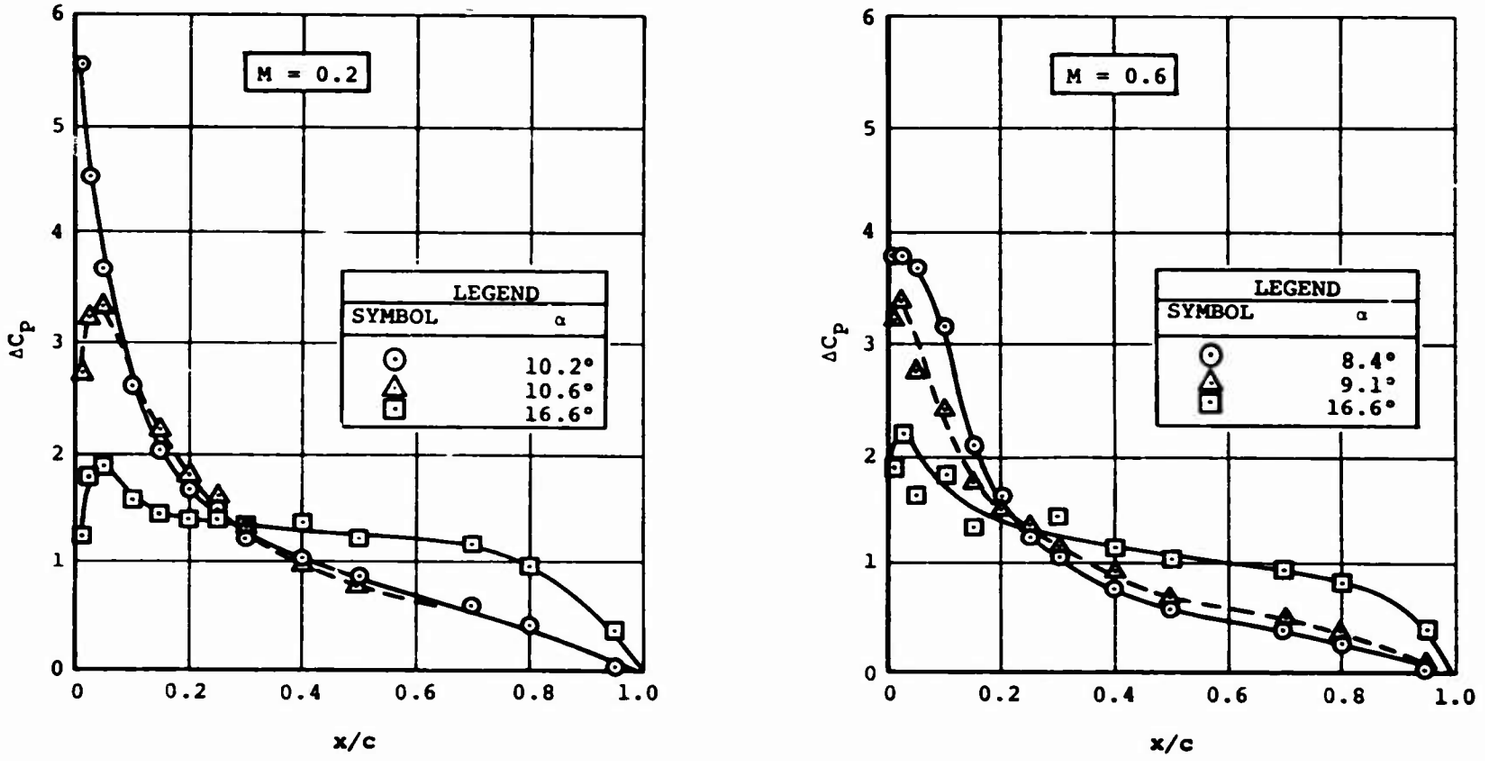

Figure 19. Static Chordwise Load Distributions Illustrating Stall Development for the Vertol 13006-.7 Airfoil at M = 0.2 and M = 0.6.

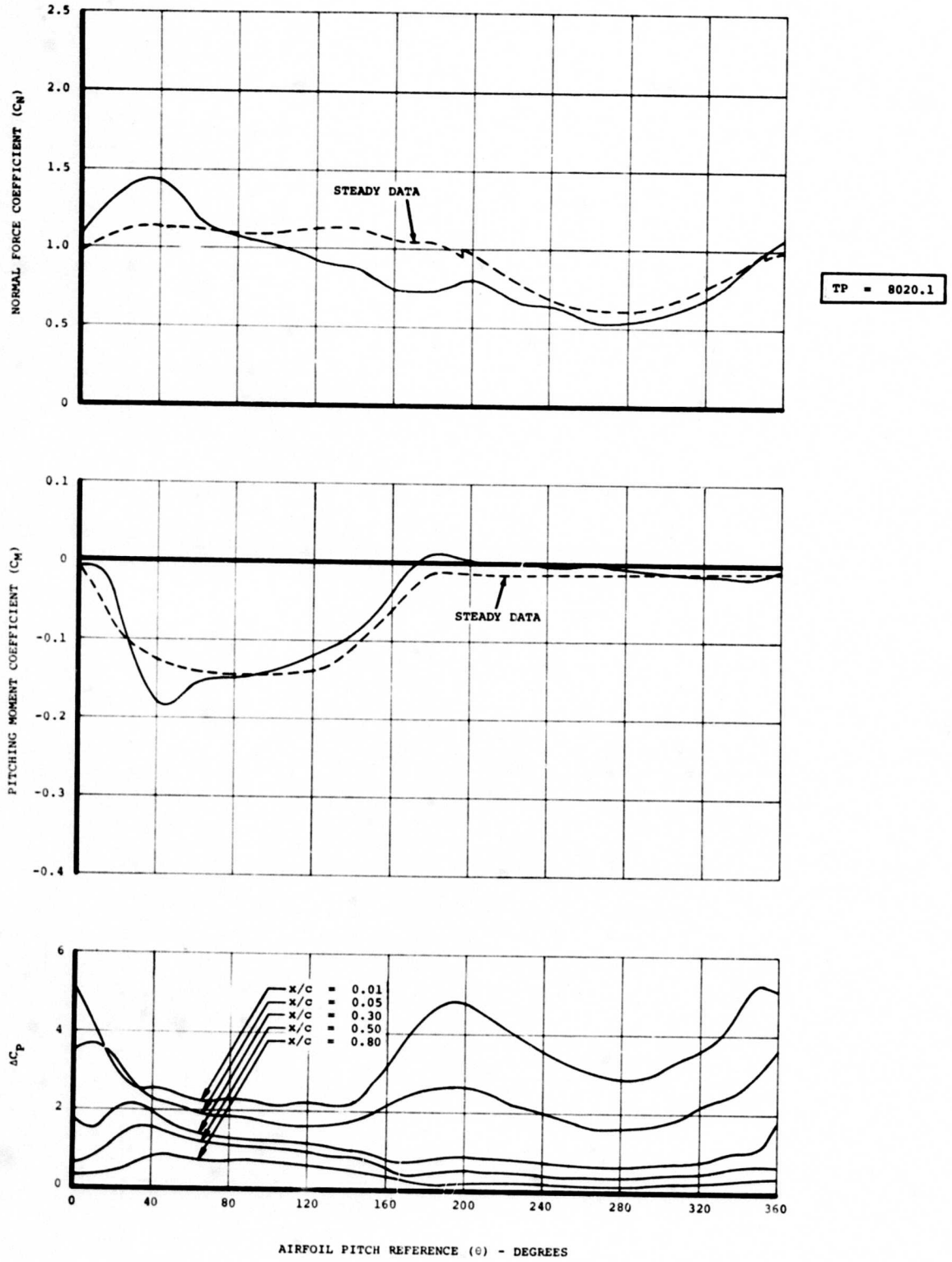

Figure 20. Cycle History of C_N, C_M, and ΔCp for the Vertol 13006-.7 Airfoil Oscillating in Pitch at M = 0.3, f = 12 Hertz, $\Delta\alpha$ = 5°, and α_o = 10°.

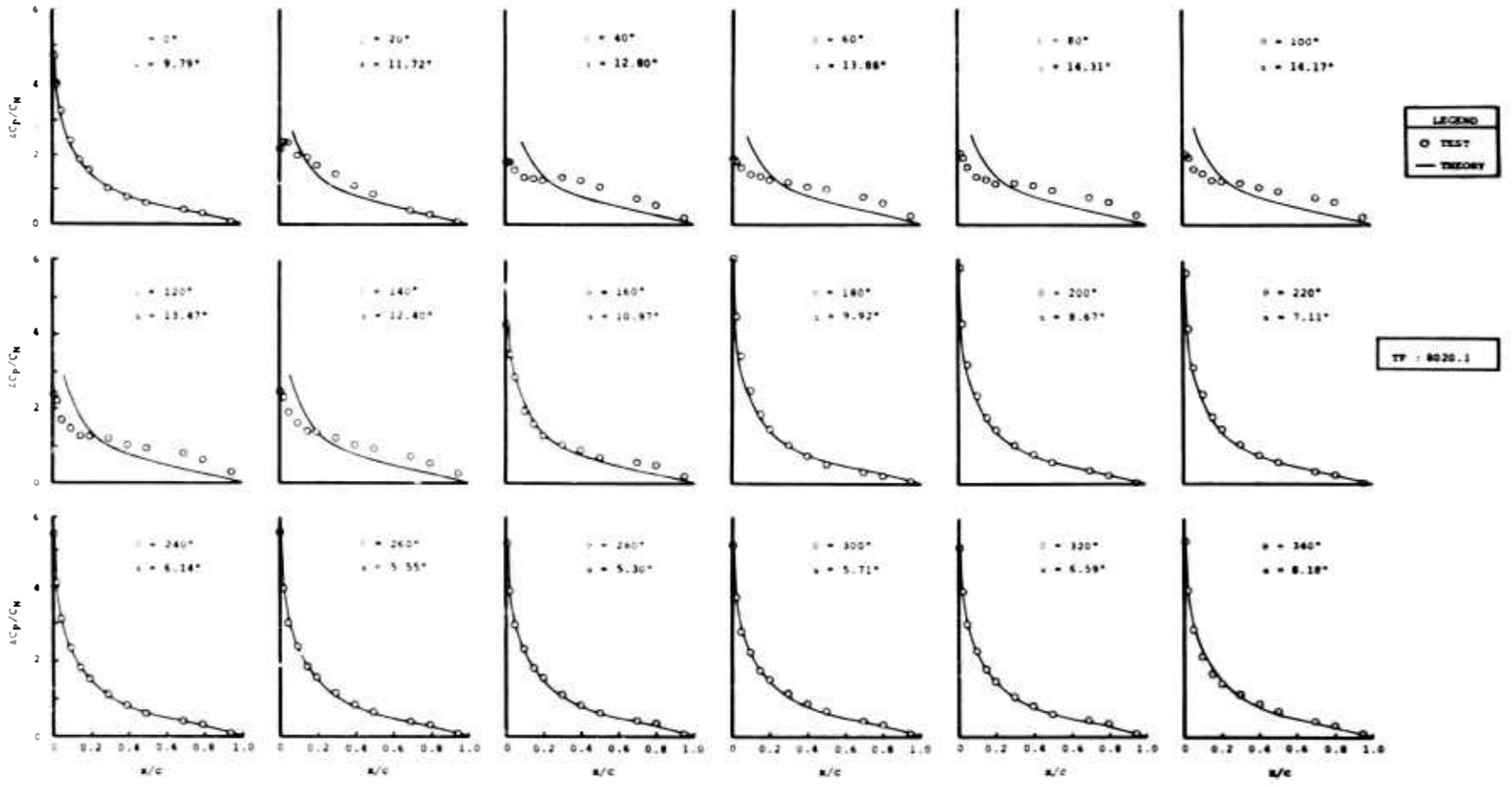

Figure 21. Sequential Chordwise Load Distributions for the Vertol 13006-.7 Airfoil in Pitching Oscillation at $M = 0.3$, $f = 12$ Hertz, $\Delta\alpha = 5°$, and $\alpha_o = 10°$.

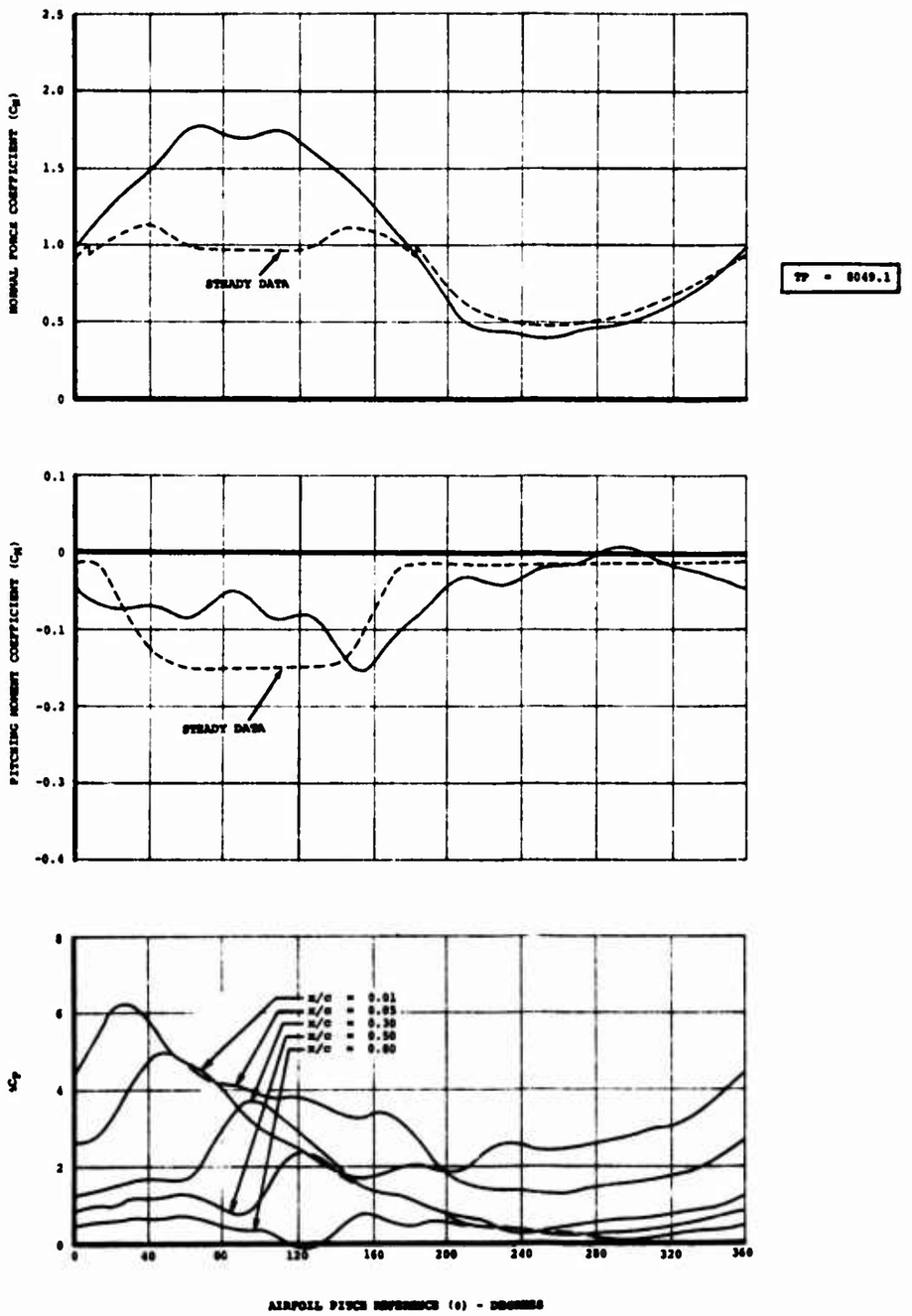

Figure 22. Cycle History of C_N, C_M, and ΔCp for the Vertol 13006-.7 Airfoil Oscillating in Pitch at M = 0.3, f = 68 Hertz, $\Delta\alpha$ = 5°, and α_o = 10°.

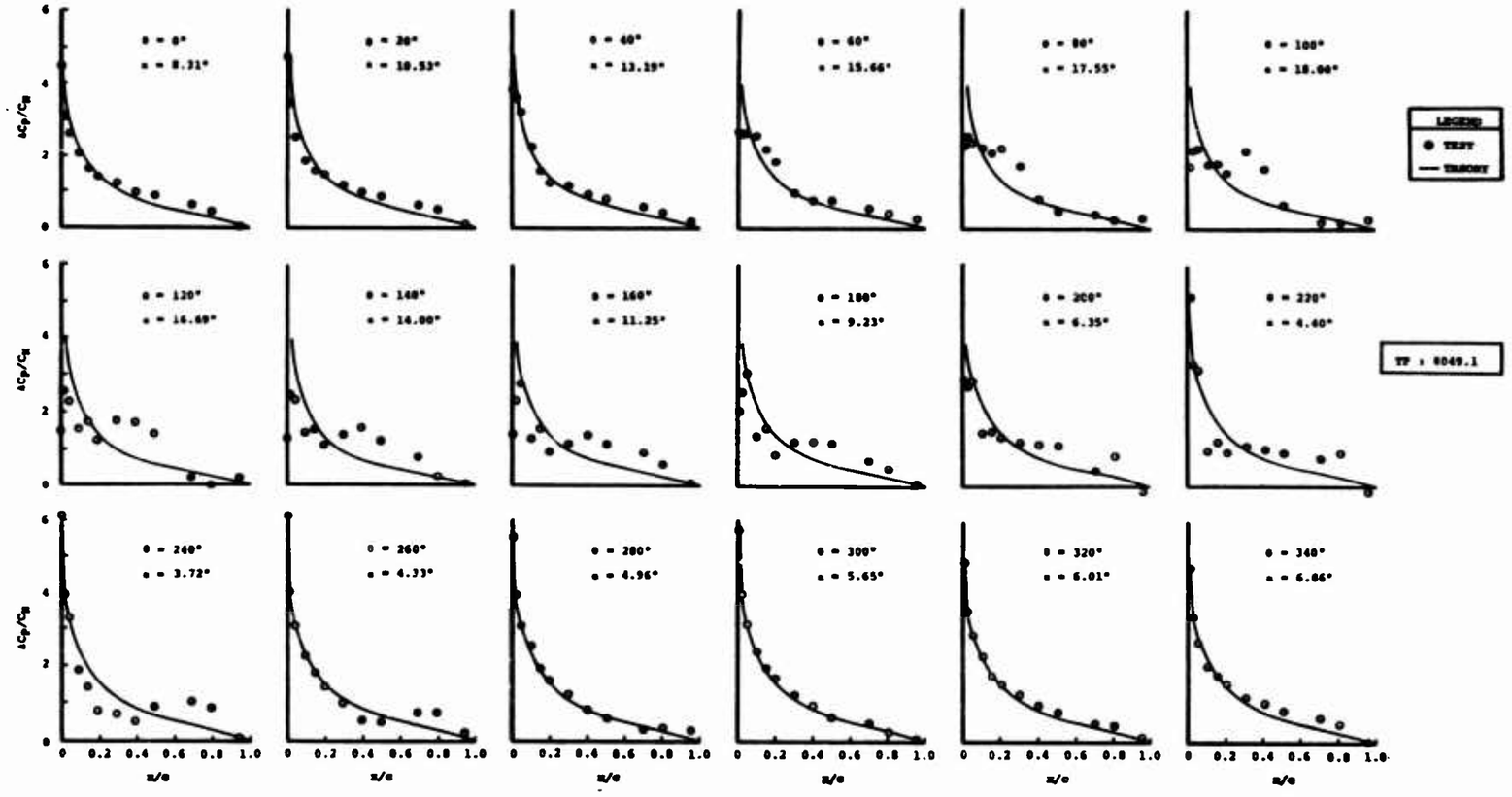

Figure 23. Sequential Chordwise Load Distributions for the Vertol 13006-.7 Airfoil in Pitching Oscillation at M = 0.3, f = 72 Hertz, $\Delta\alpha$ = 5°, and α_o = 10°.

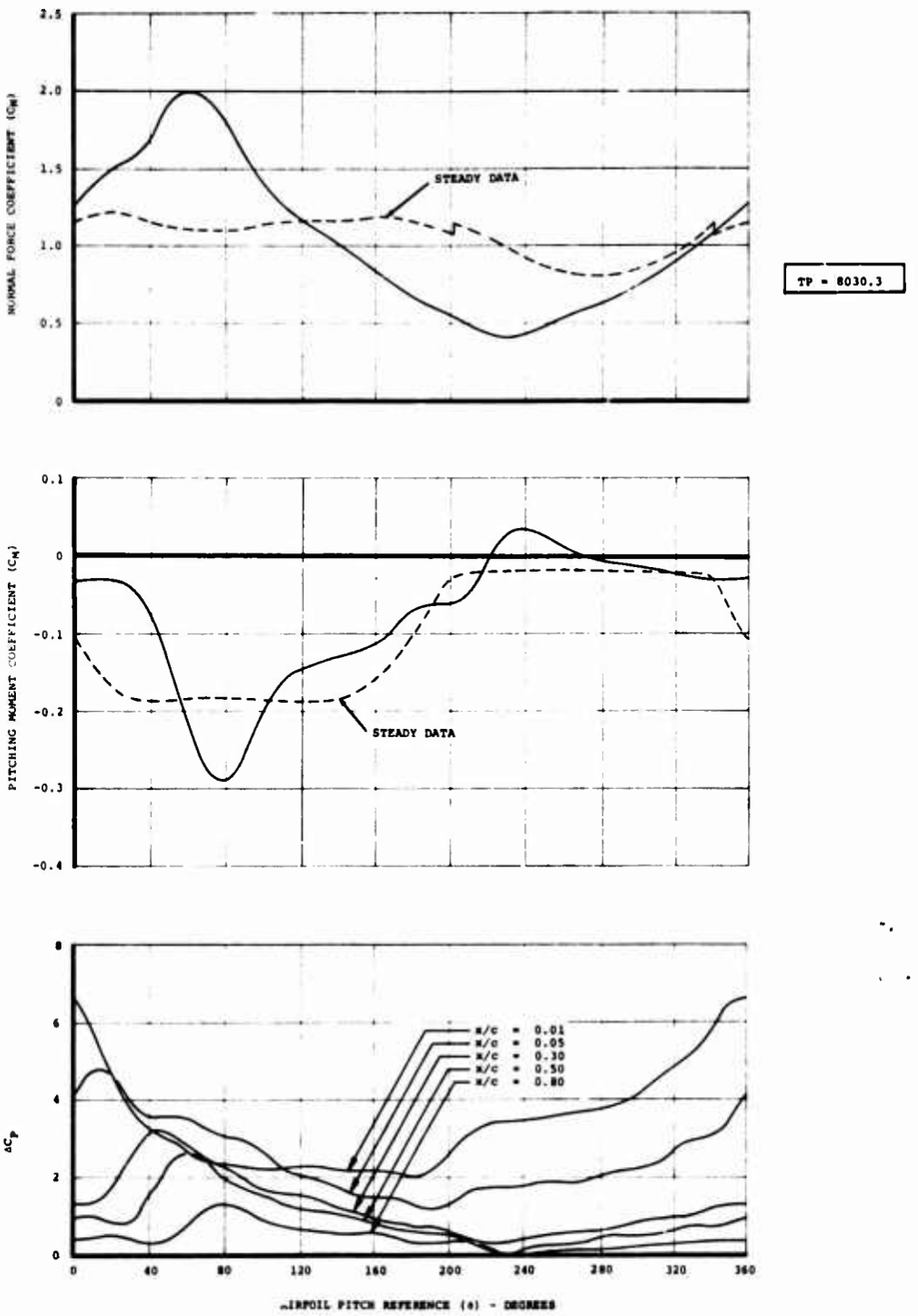

Figure 24. Cycle History of C_N, C_M, and ΔC_p for the Vertol 13006-.7 Airfoil Oscillating in Pitch at M = 0.2, f = 24 Hertz, $\Delta\alpha$ = 5°, and α_o = 12°.

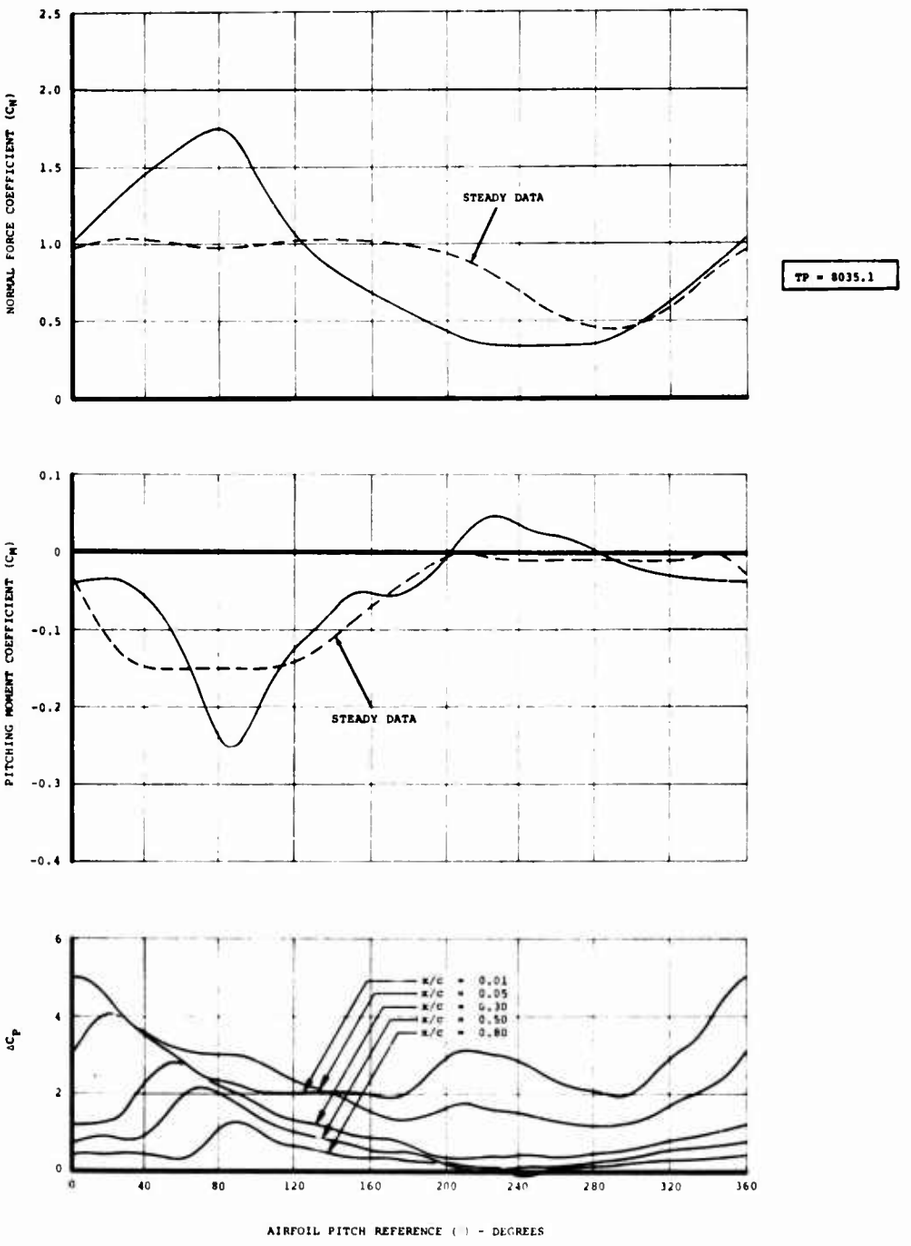

Figure 25. Cycle History of C_N, C_M, and ΔC_p for the Vertol 13006-.7 Airfoil Oscillating in Pitch at M = 0.4, f = 48 Hertz, $\Delta\alpha$ = 5°, and α_o = 10°.

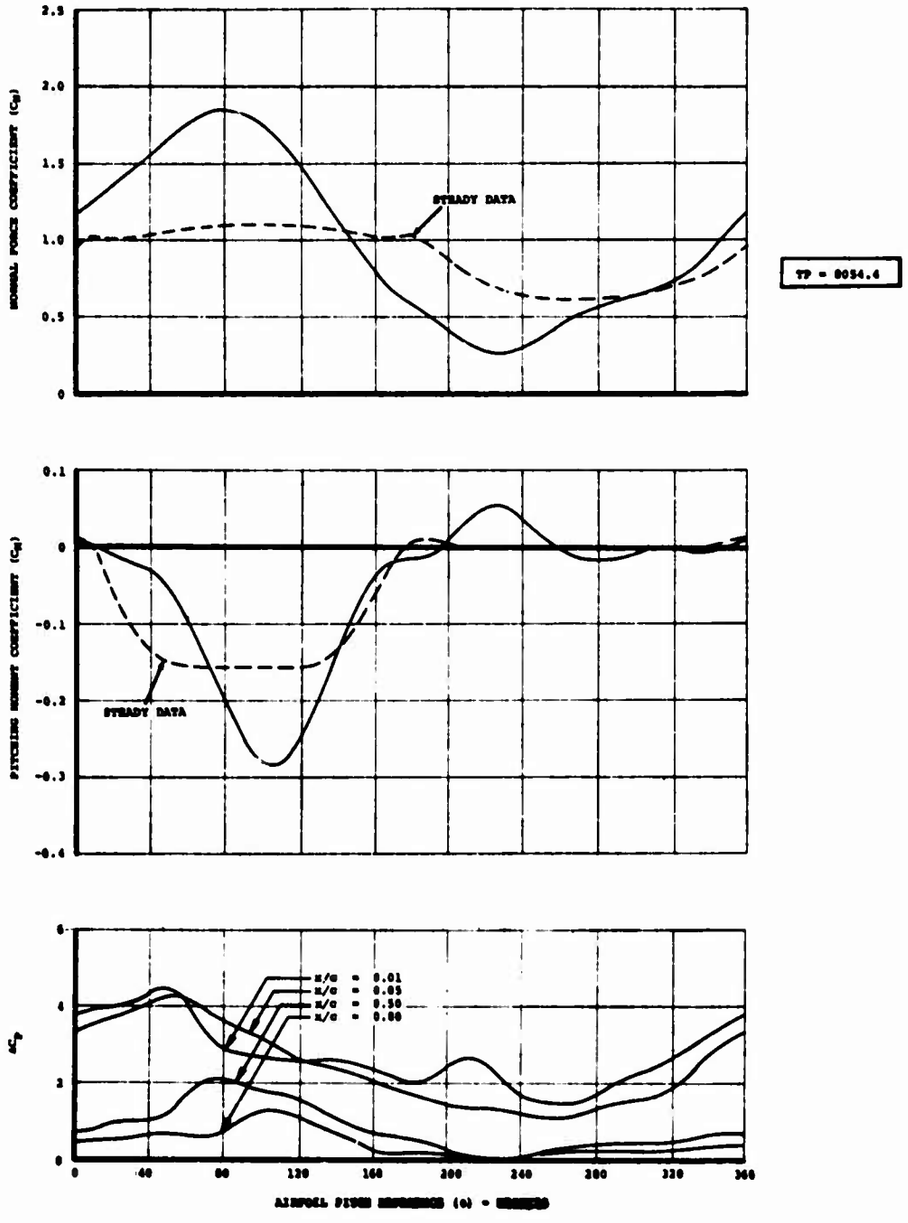

Figure 26. Cycle History of C_N, C_M, and ΔCp for the Vertol 13006-.7 Airfoil Oscillating in Pitch at M = 0.6, f = 72 Hertz, $\Delta\alpha$ = 5°, and α_o = 10°.

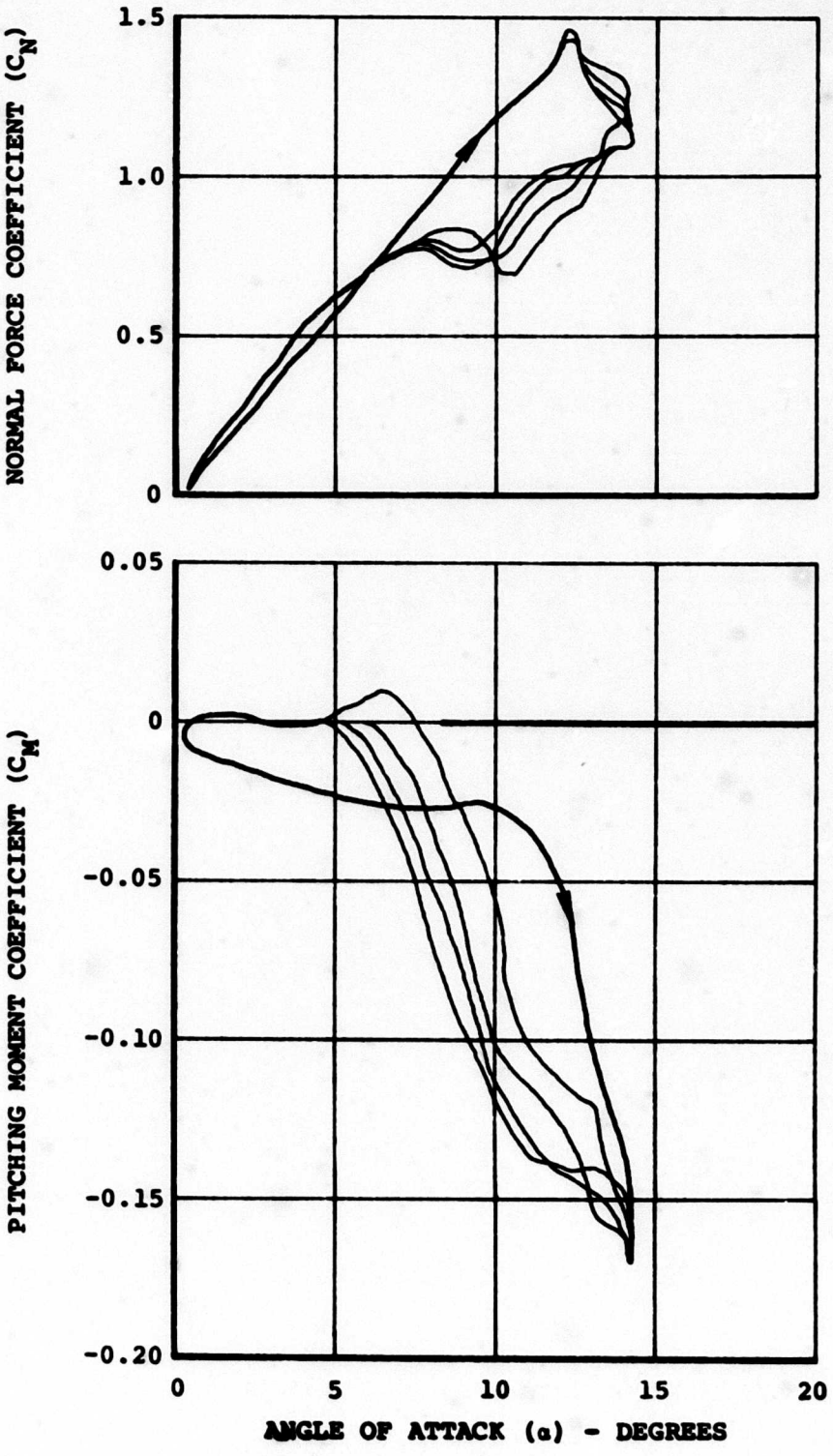

Figure 27. Successive Cycle-to-Cycle Variations in C_N and C_M During Pitch Oscillation for the Vertol 13006-.7 Airfoil.

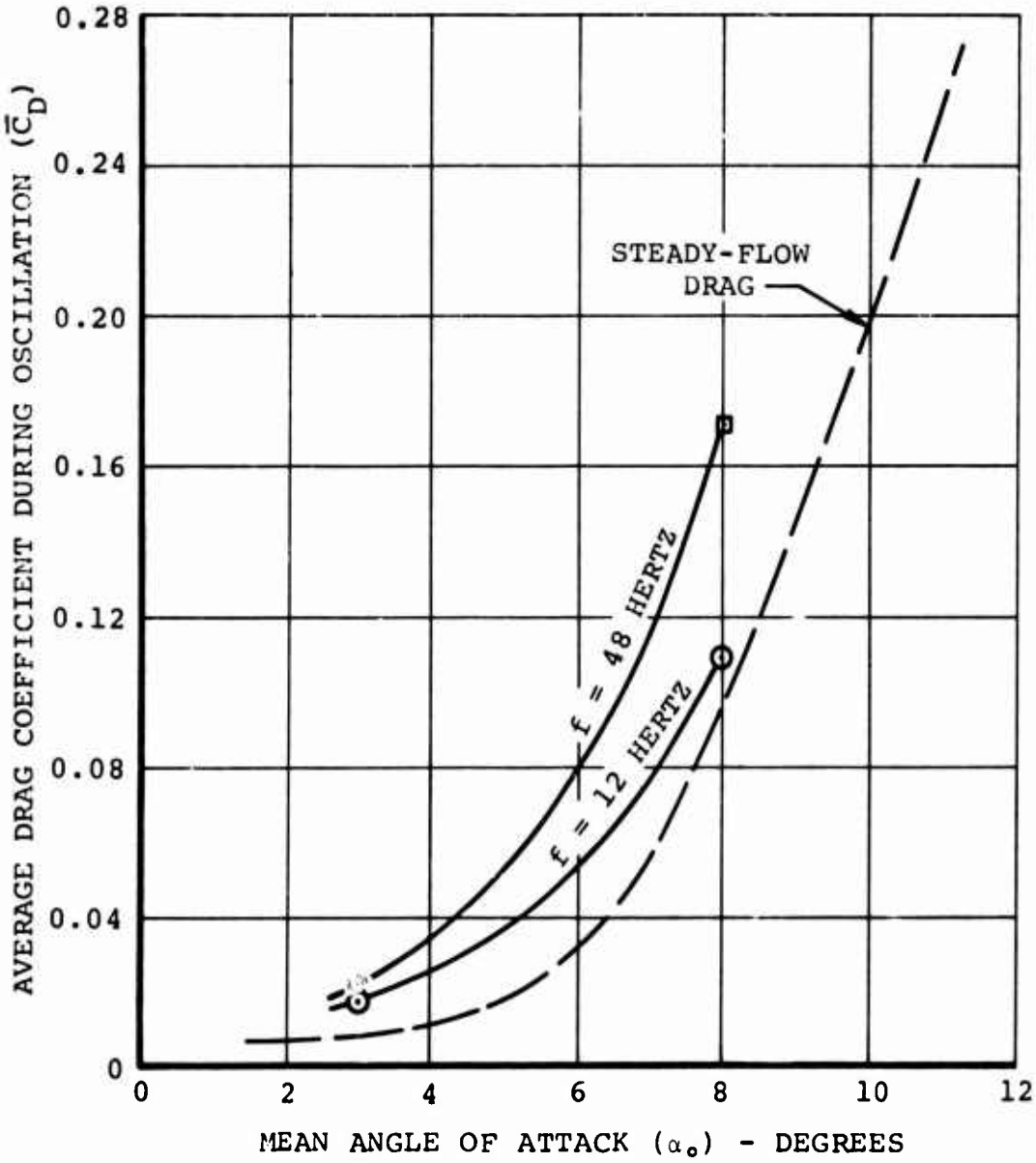

Figure 28. Oscillatory Drag Data for the NACA 0006 Airfoil From Wake Traverse Measurements at M = 0.4 and $\Delta\alpha = 5°$.

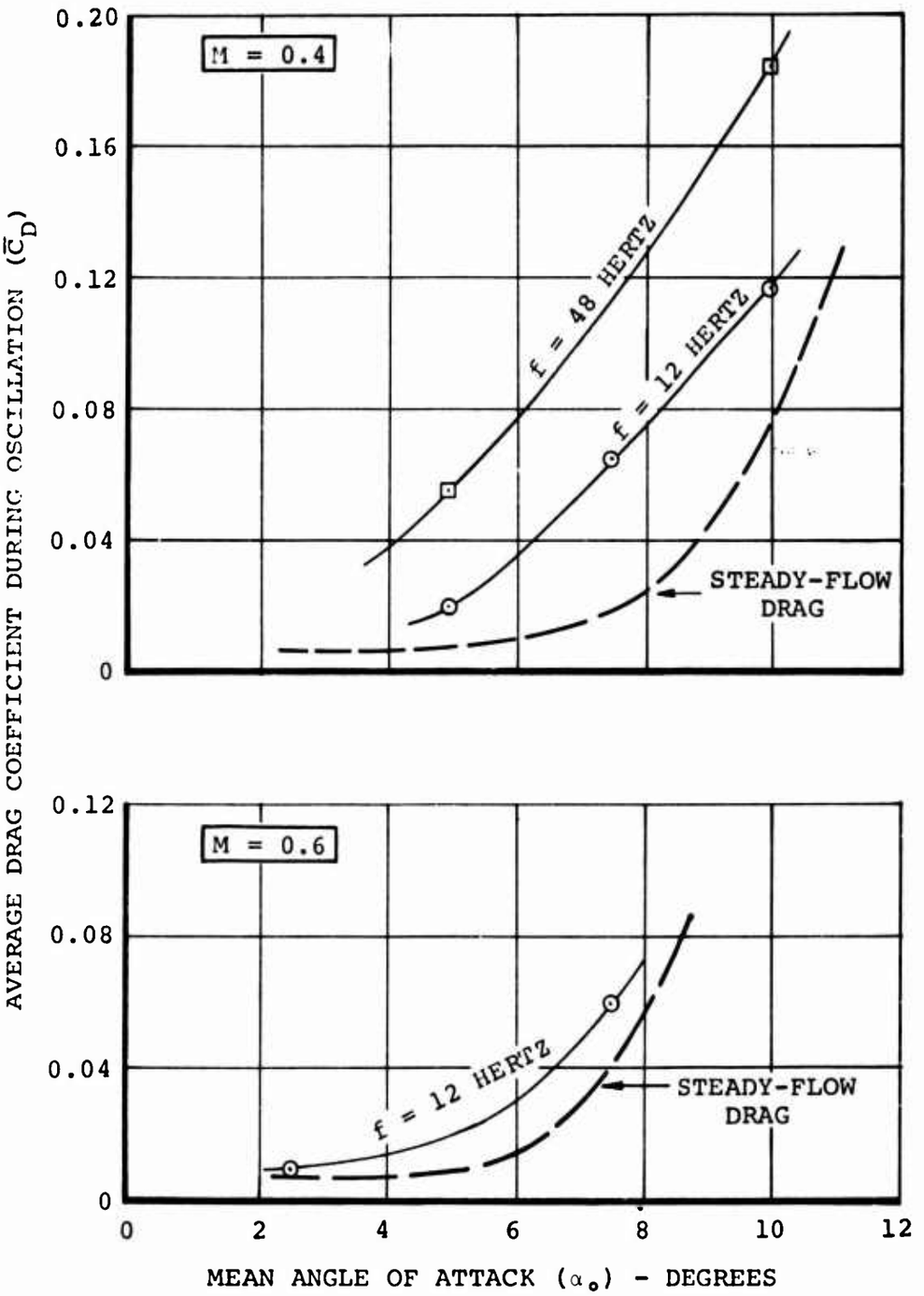

Figure 29. Oscillatory Drag Data for the Vertol 13006-.7 Airfoil From Wake Traverse Measurements at $\Delta\alpha = 5°$.

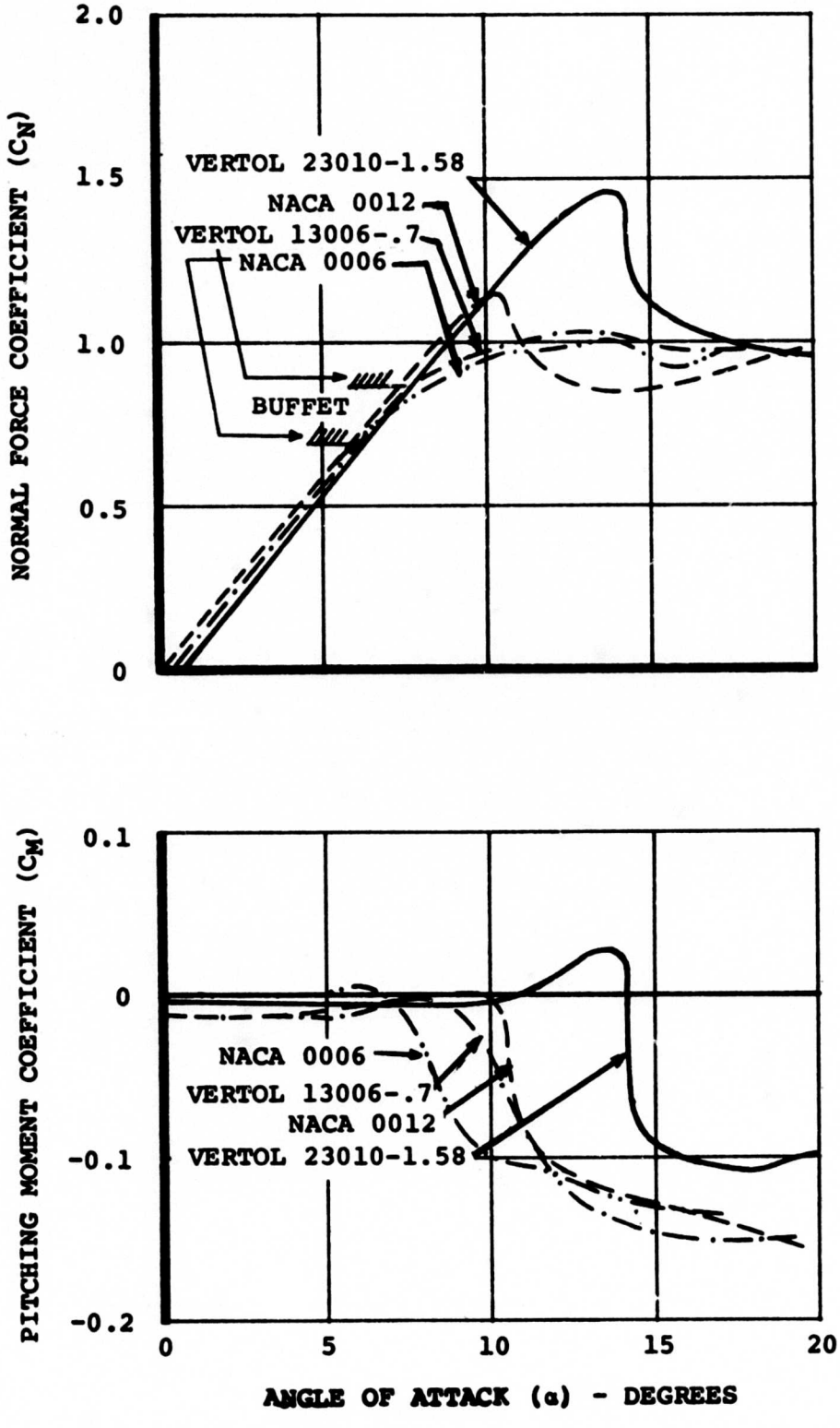

Figure 30. Comparison of Steady-Flow C_N and C_M Characteristics With Data of Reference 2 at M = 0.4.

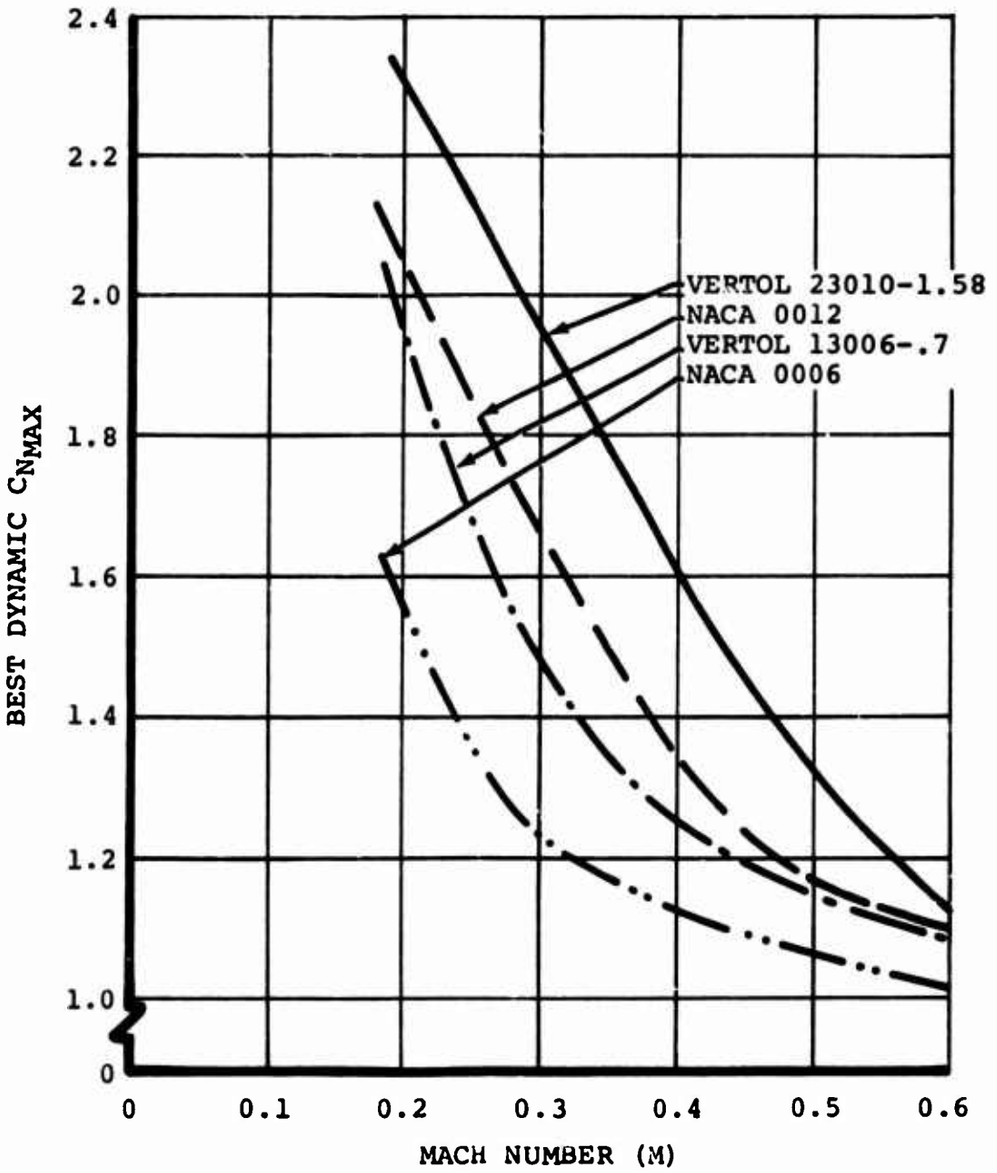

Figure 31. Comparison of Maximum Attainable Normal Force Characteristics With Data of Reference 2, at f = 1/Rev Frequency and $\Delta\alpha$ = 5°.

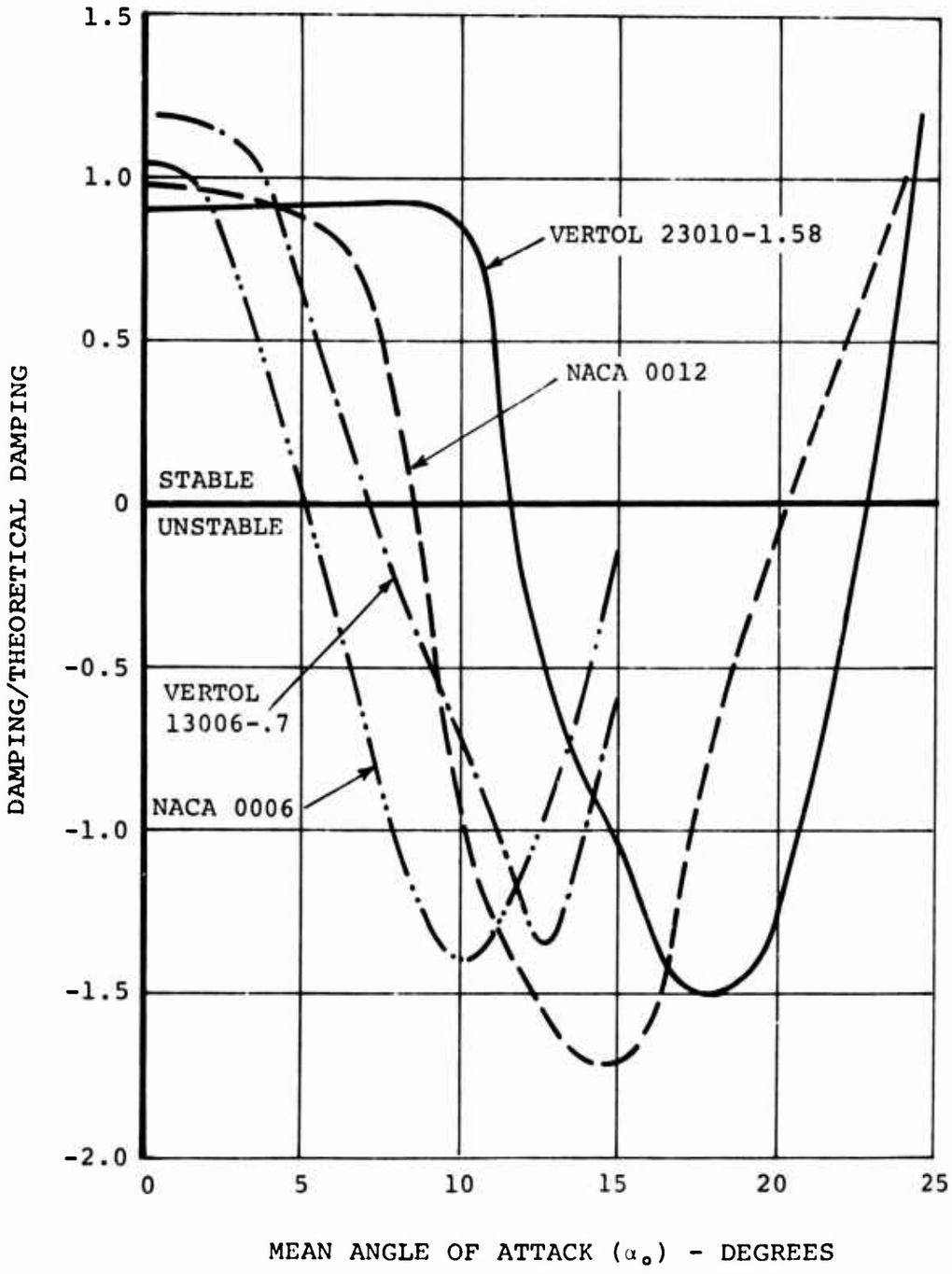

Figure 32. Comparison of Aerodynamic Damping With Data of Reference 2, at 6/Rev Frequency, M = 0.4, and $\Delta\alpha$ = 5°.

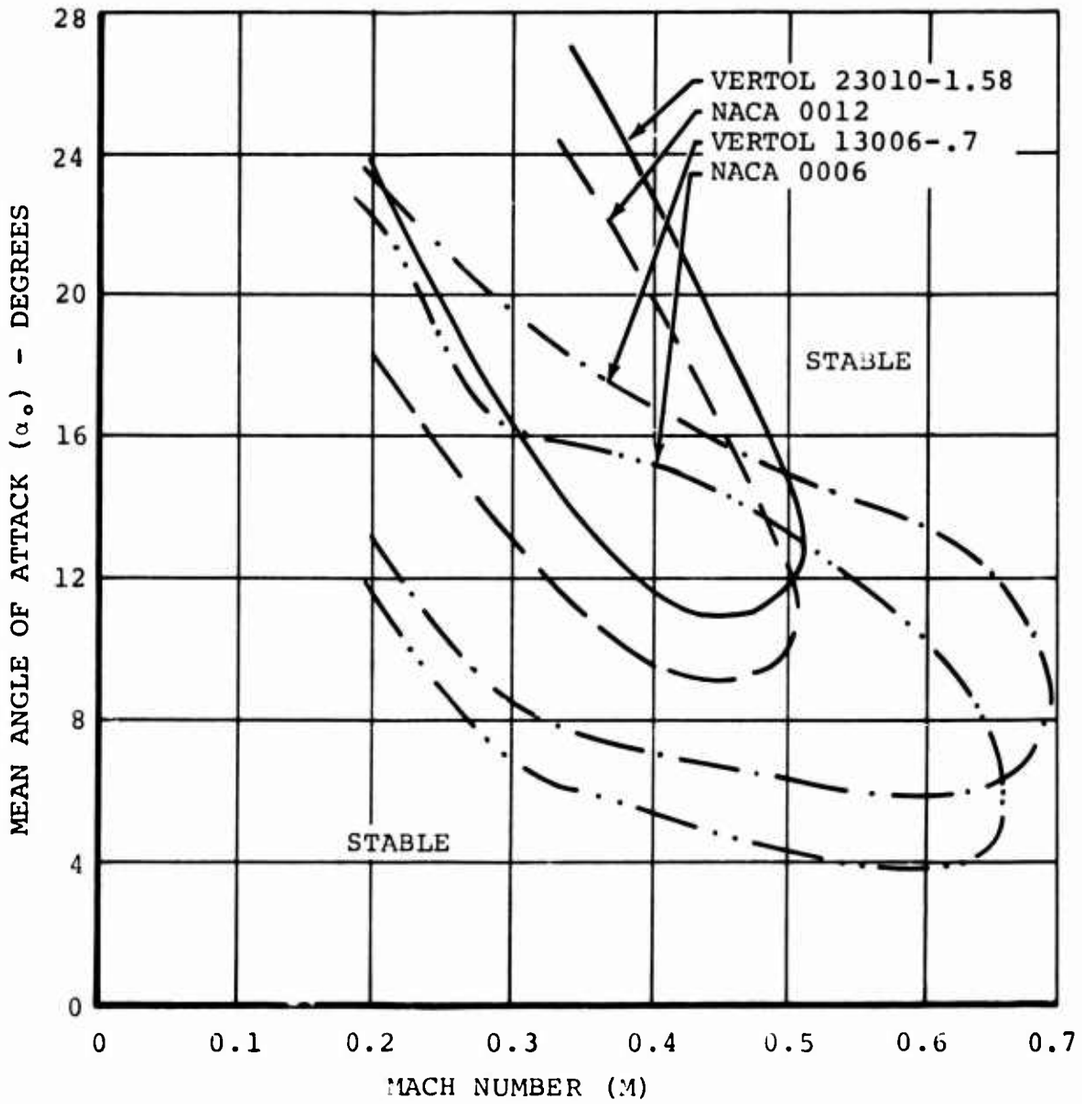

Figure 33. Comparison of Aerodynamic Instability Regions With Data of Reference 2, at 6/Rev Frequency and $\Delta\alpha = 5°$.

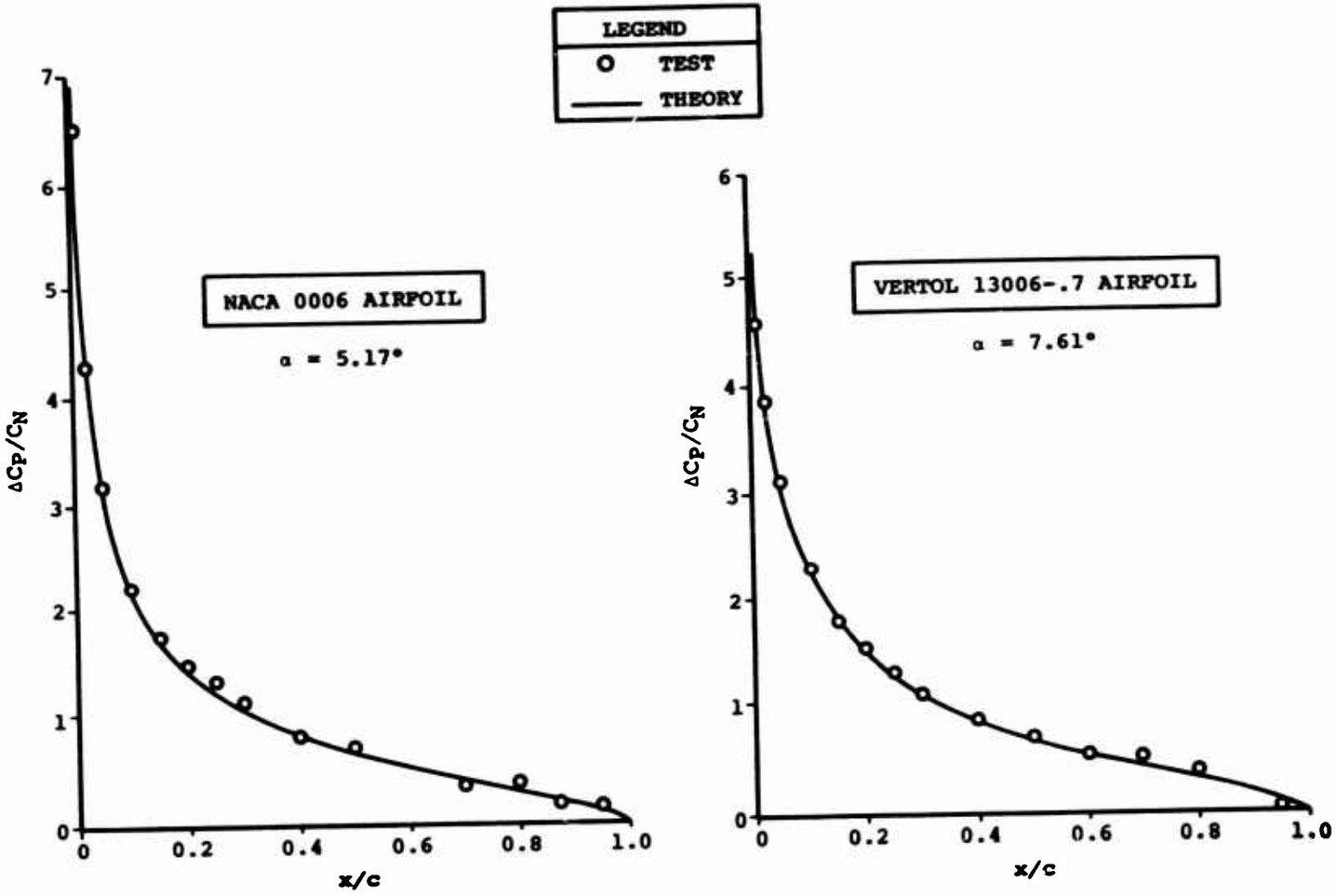

Figure 34. Comparison of Test and Theoretical Static Load Distribution for the NACA 0006 and Vertol 13006-.7 Airfoils at M = 0.2.

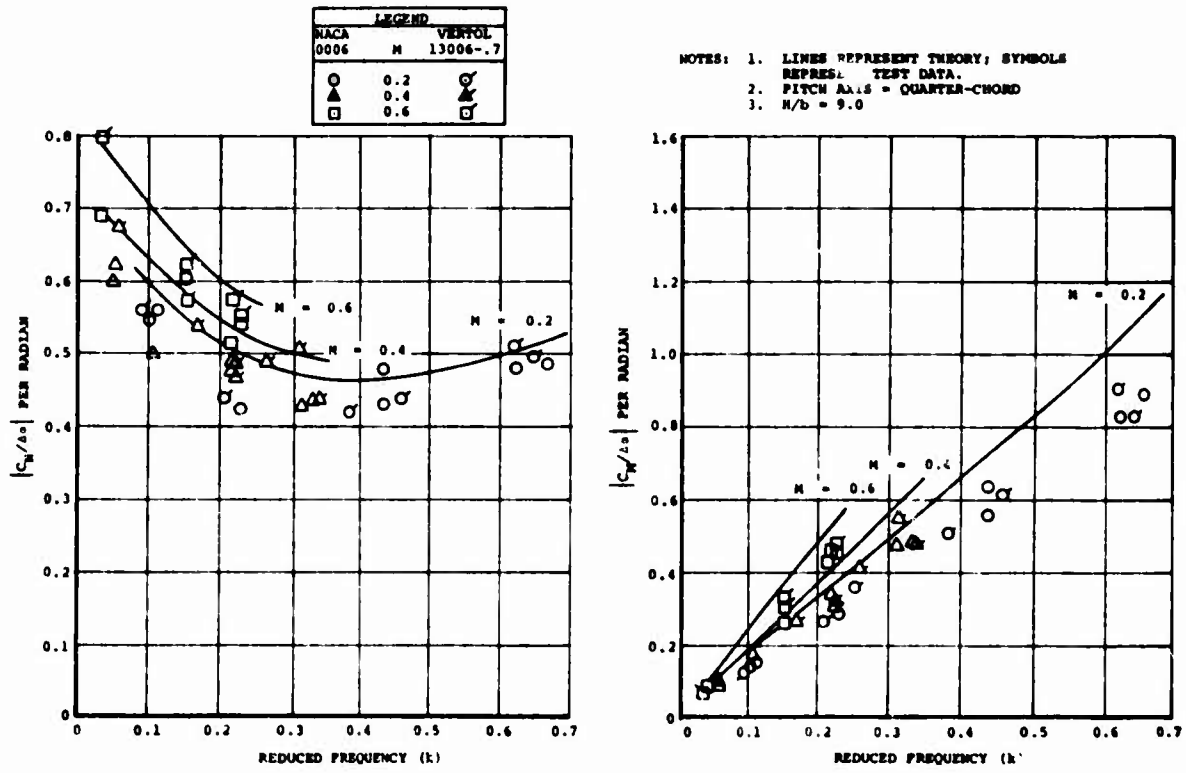

Figure 35. Comparison of Pitch Oscillation Test Data With Theory.

LITERATURE CITED

1. Harris, F.D., SPANWISE FLOW EFFECTS ON ROTOR PERFORMANCE, Proceedings of the Symposium on Aerodynamics Problems Associated with V/STOL Aircraft, CAL/USAAVLABS, June 1966.

2. Liiva, J., Davenport, F.J., Gray, L., and Walton, I., TWO-DIMENSIONAL TESTS OF AIRFOILS OSCILLATING NEAR STALL, USAAVLABS Technical Report 68-13, Volumes I and II, U.S. Army Aviation Materiel Laboratories, Fort Eustis, Virginia, April 1968, AD670957 and AD670958.

3. Davenport, F.J., and Front, J.V., AIRFOIL SECTIONS FOR ROTOR BLADES - A RECONSIDERATION, American Helicopter Society, Inc., 22nd Annual Forum, 12 May 1966.

4. Bisplinghoff, Raymond L., Ashley, Holt, and Halfman, Robert L., AEROELASTICITY, Addison-Wesley Publishing Company, Inc., Reading, Massachusetts, 1955.

5. McCullough, G.B., and Gault, D.E., EXAMPLES OF THREE REPRESENTATIVE TYPES OF AIRFOIL-SECTION STALL AT LOW SPEED, NACA TN2502, September 1951.

6. Abbott, I.H., and Von Doenhoff, A.E., THEORY OF WING SECTIONS, Dover Publications, New York, N.Y., June 1958.

7. Davenport, F.J., SINGULARITY SOLUTIONS TO GENERAL POTENTIAL-FLOW AIRFOIL PROBLEMS, The Boeing Company, Document D6-7202, Revised May 1963.

8. Halfman, Robert L., Johnson, H.C., and Haley, S.M., EVALUATION OF HIGH-ANGLE-OF-ATTACK AERODYNAMIC-DERIVATIVE DATA AND STALL-FLUTTER PREDICTION TECHNIQUES, Massachusetts Institute of Technology, TN2533, National Advisory Committee for Aeronautics, Washington, D.C., November

9. Runyan, Harry L., and Watkins, Charles E., CONSIDERATIONS ON THE EFFECT OF WIND-TUNNEL WALLS ON OSCILLATING AIR FORCES FOR TWO-DIMENSIONAL SUBSONIC COMPRESSIBLE FLOW, Langley Aeronautical Laboratory, TN2552, National Advisory Committee for Aeronautics, Washington, D.C., December 1951.

10. Runyan, Harry L., Woolston, Donald S., and Rainey, A. Gerald, THEORECTICAL AND EXPERIMENTAL INVESTIGATION OF THE EFFECT OF TUNNEL WALLS ON THE FORCES ON AN OSCILLATING AIRFOIL IN TWO-DIMENSIONAL SUBSONIC COMPRESSIBLE FLOW, Langley Aeronautical Laboratory, TN3416, National Advisory Committee for Aeronautics, Washington, D.C., June 1955.

11. MANUAL ON AEROELASTICITY, PART IV, North Atlantic Treaty Organization Advisory Group for Aeronautical Research and Development, NASA N63-17815, August 1965.

APPENDIX I
STATIC (NONOSCILLATORY) TESTS

Each airfoil was tested under the steady-α condition over the full range of α and M at which dynamic data were obtained.

Figures 36 through 38 show steady C_N and C_M versus α characteristics for both airfoils. The position of sharp changes in the airfoil characteristics was verified from continuous analog records.

The cambered airfoil has higher $C_{N_{MAX}}$ and α_{STALL} than the symmetrical section. Neither profile is subject to large discontinuities on the C_N curve. Below M = 0.4, both airfoils exhibit a leading-edge laminar separation bubble which is a well-known characteristic of thin airfoils[5]. The onset of this phenomenon is indicated by the notch in the C_N curve, which occurs later with the cambered airfoil and precedes full stall development.

Both airfoils show well-behaved pitching moment behavior at angles of attack below stall. The presence of small changes in $dC_M/d\alpha$ with increasing Mach number for the NACA 0006 airfoil reflects a slight forward shift of the aerodynamic center. Stalling characteristics indicated consistent trends for the range of Mach numbers tested, without the abrupt drop shown by the thicker airfoils in Reference 2.

In Figures 39 through 41, C_N versus C_M curves are presented for each airfoil. Comparison with unpublished data obtained during 1965 from tests using the same wind tunnel facilities is given for M = 0.4 and 0.6 in Figure 42. Good agreement was obtained for both airfoils.

Static drag data from wake traverse measurements are shown in Figure 43 for both airfoils. The tests on the NACA 0006, limited to M = 0.4, show a lower α for drag rise due to stall. This is consistent with the normal force and moment data. Figure 44 presents static C_N versus C_D data for the Vertol 13006-.7 airfoil in comparison with the previous measurements. Good agreement is obtained at both M = 0.4 and 0.6.

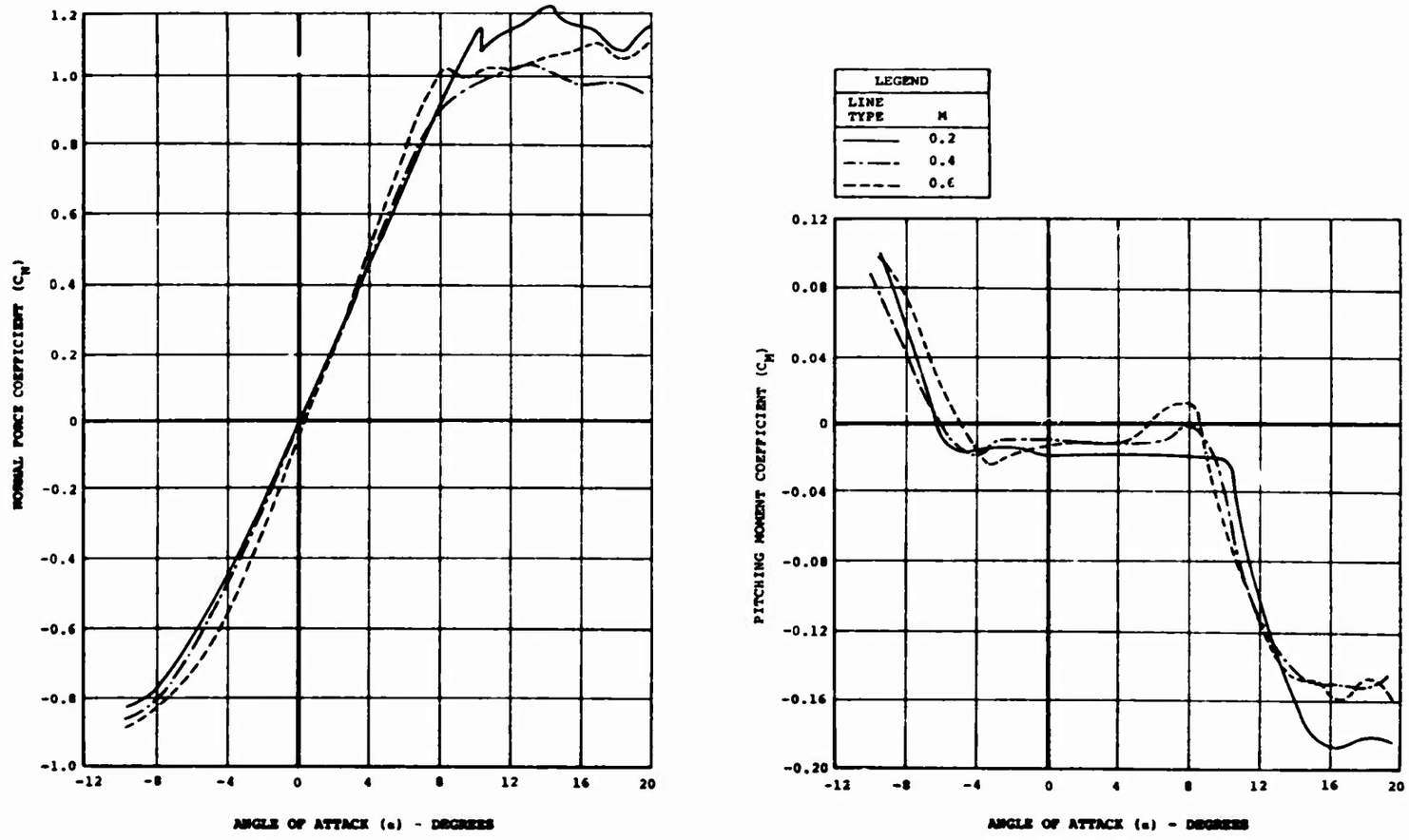

Figure 36. Static C_N and C_M Versus α Characteristics for the Vertol 13006-.7 Airfoil at M = 0.2, 0.4, and 0.6.

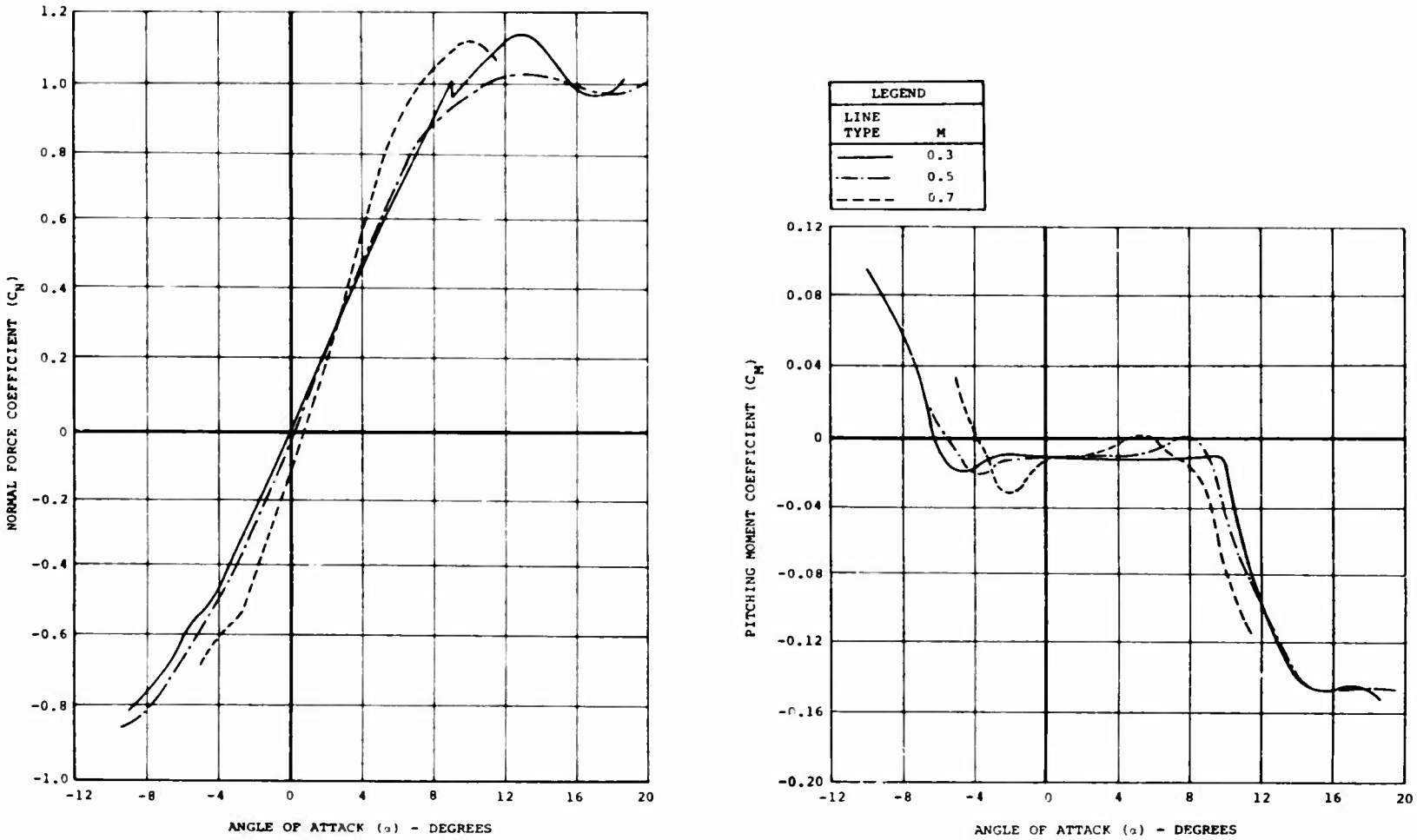

Figure 37. Static C_N and C_M Versus α Characteristics for the Vertol 13006-.7 Airfoil at M = 0.3, 0.5, and 0.7.

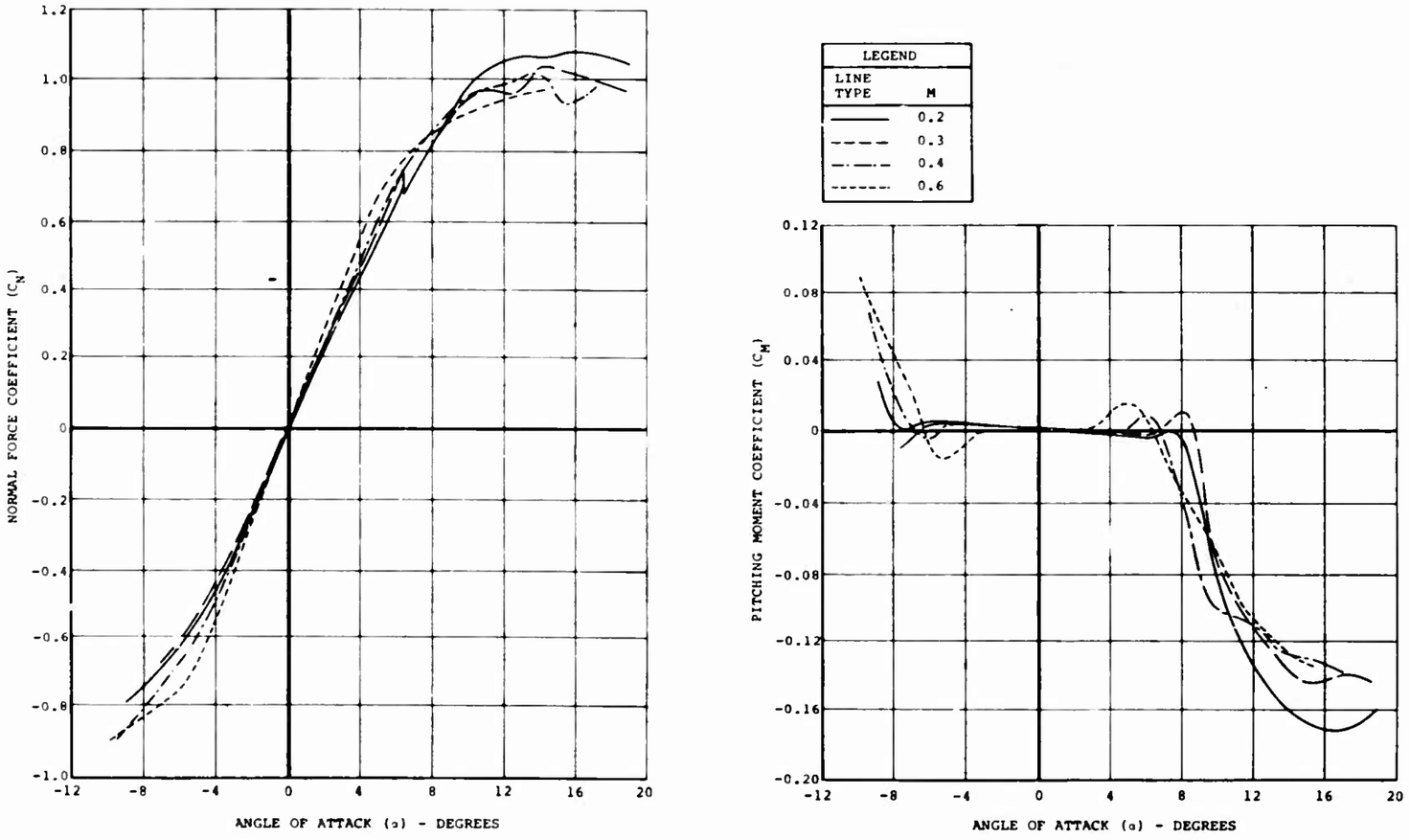

Figure 38. Static C_N and C_M Versus α Characteristics for the NACA 0006 Airfoil at M = 0.2, 0.3, 0.4, and 0.6.

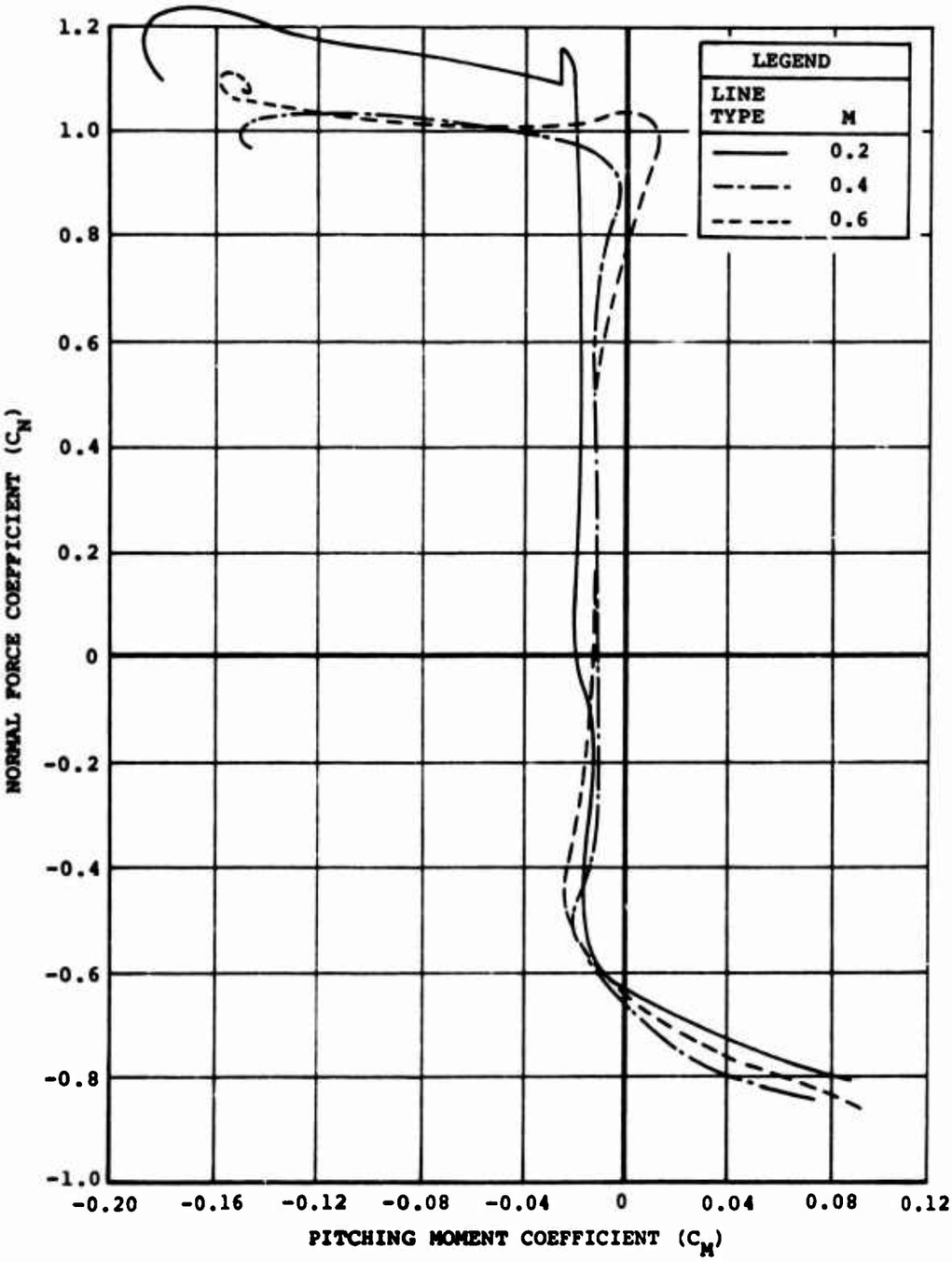

Figure 39. Static C_N Versus C_M Characteristics for the Vertol 13006-.7 Airfoil at M = 0.2, 0.4, and 0.6.

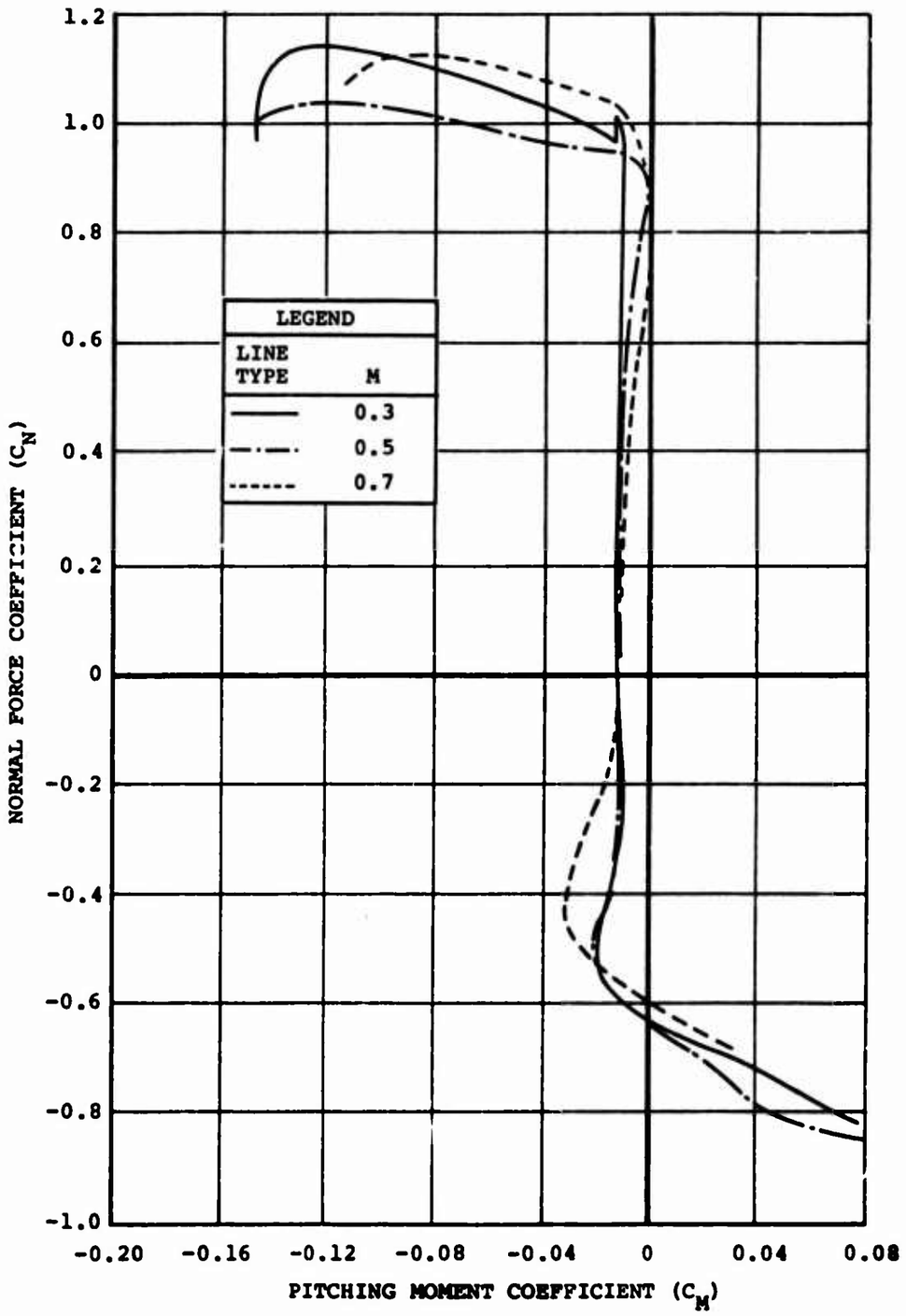

Figure 40. Static C_N Versus C_M Characteristics for the Vertol 13006-.7 Airfoil at M = 0.3, 0.5, and 0.7.

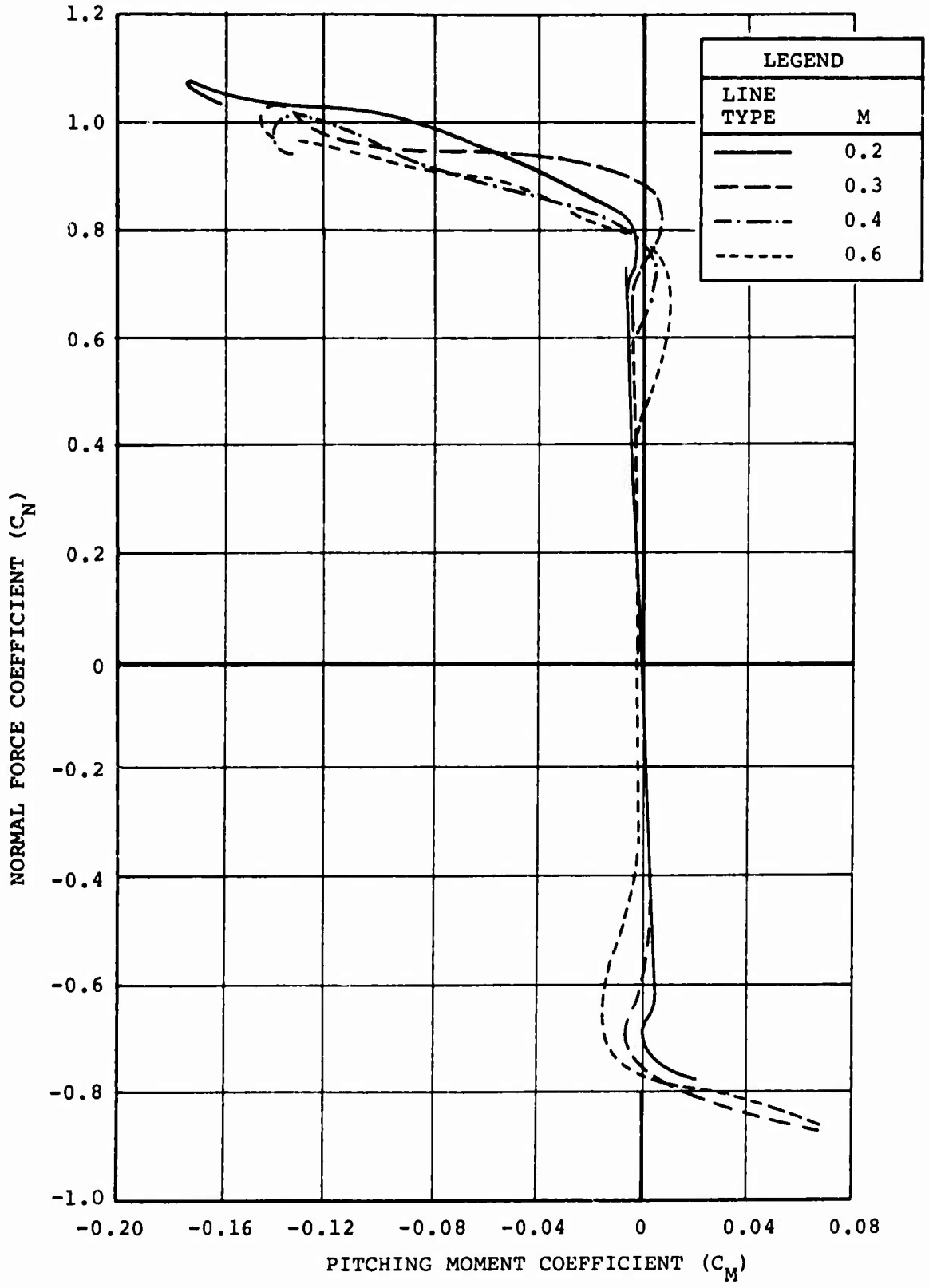

Figure 41. Static C_N Versus C_M Characteristics for the NACA 0006 Airfoil at M = 0.2, 0.3, 0.4, and 0.6.

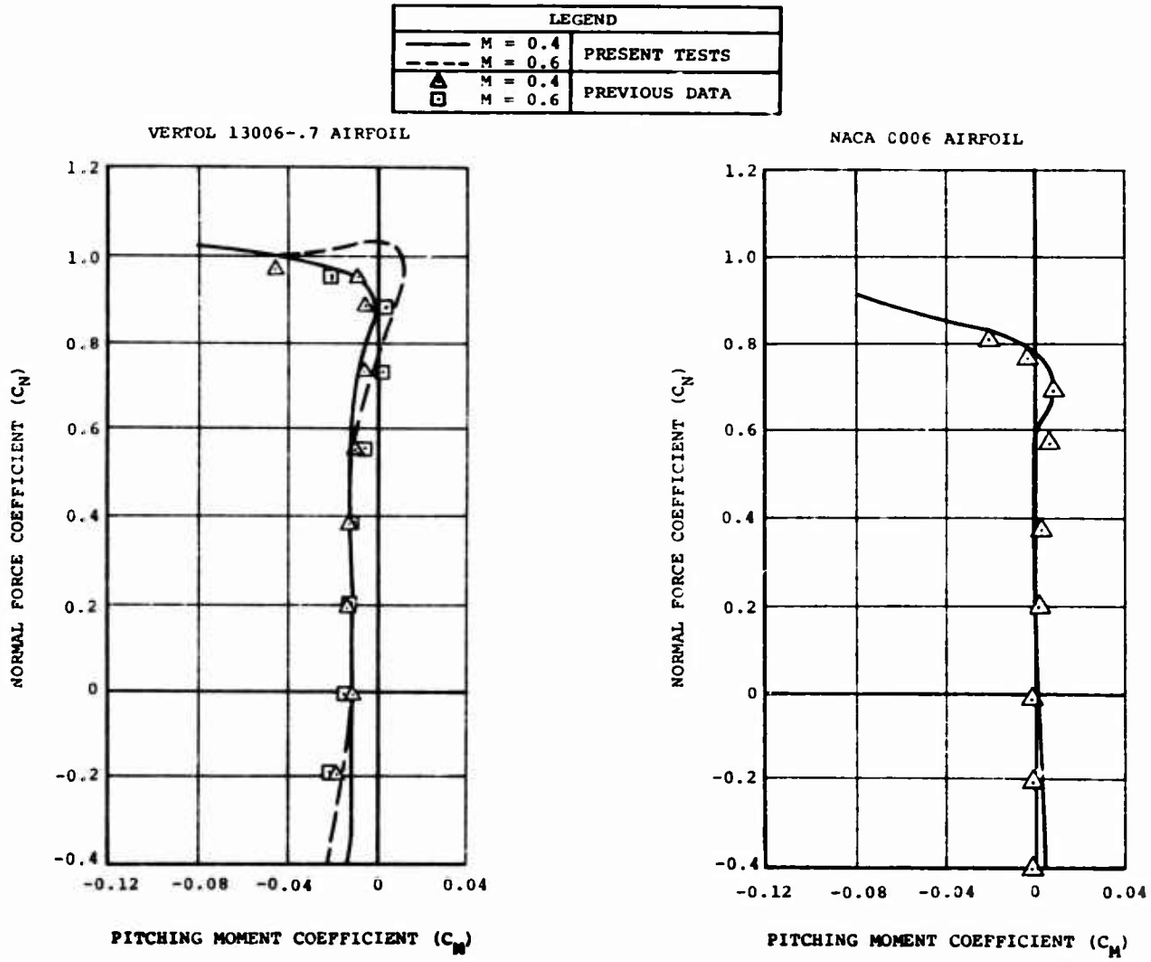

Figure 42. Comparison of Static C_N Versus C_M With Previous Data for the Vertol 13006-.7 and NACA 0006 Airfoils.

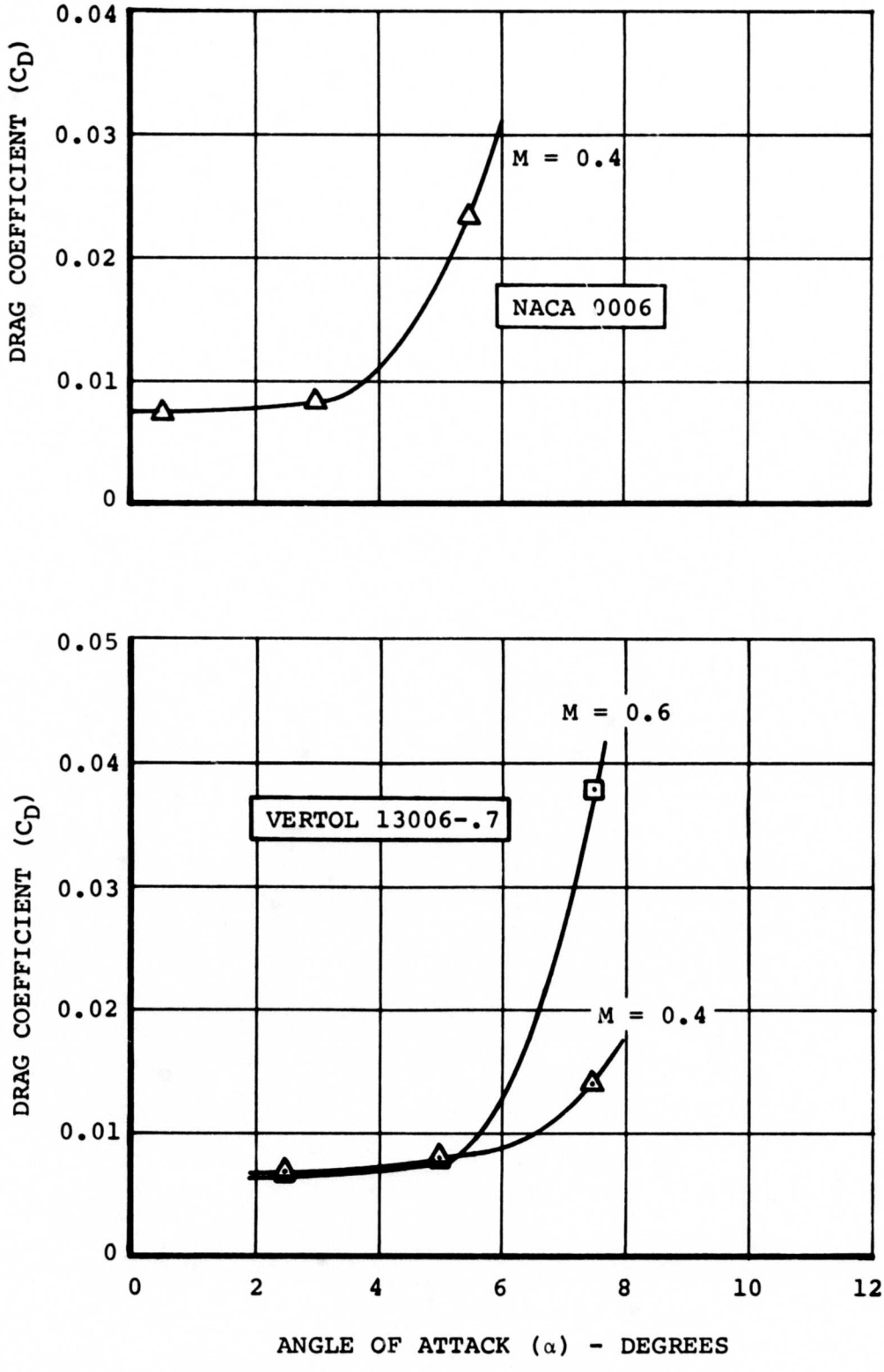

Figure 43. Static C_D Versus α for the NACA 0006 and Vertol 13006-.7 Airfoils.

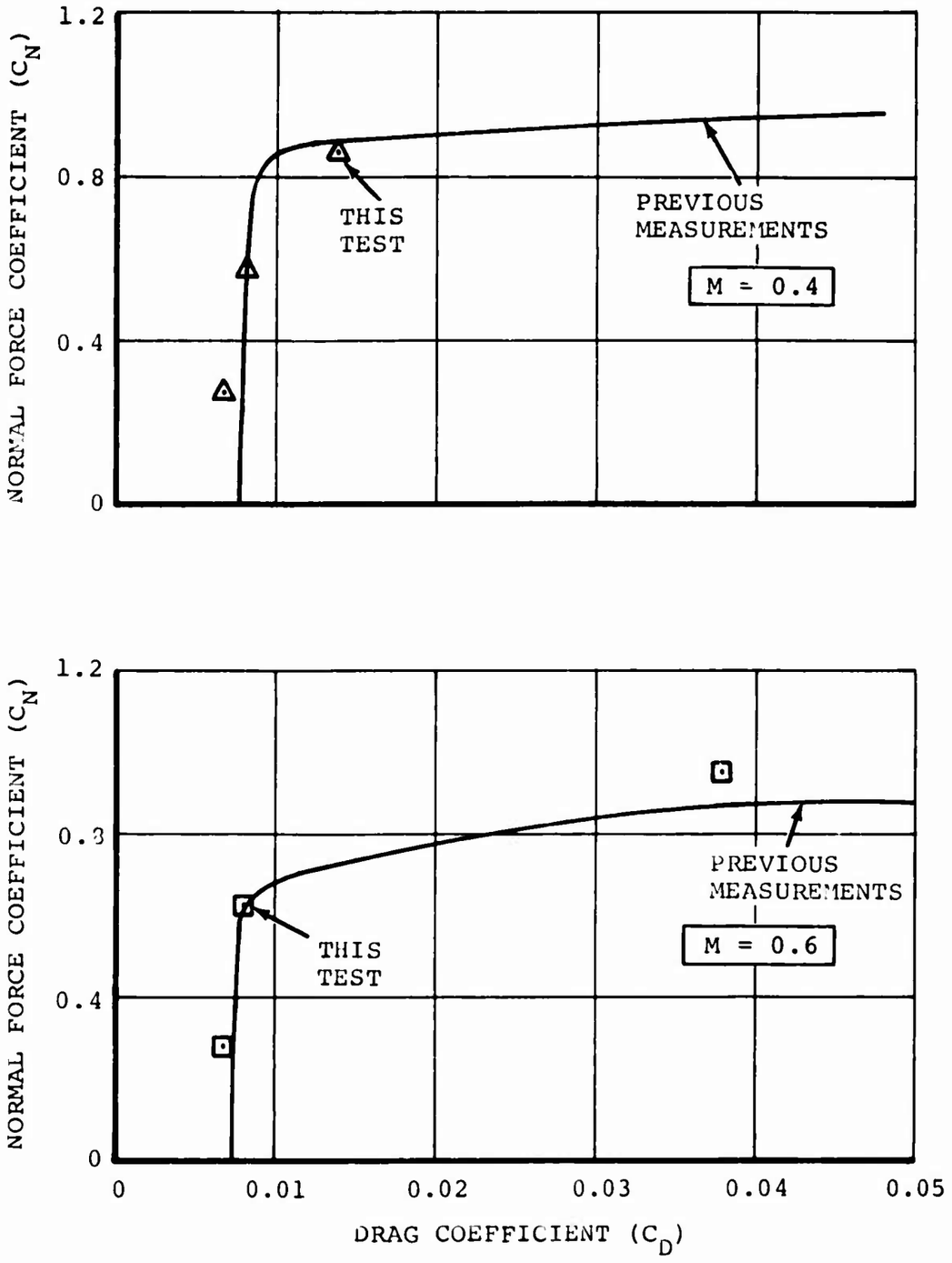

Figure 44. Comparison of Vertol 13006-.7 Steady Drag Data With Previous Measurements.

APPENDIX II
WIND TUNNEL WALL CORRECTIONS

Wind tunnel boundary corrections were developed by using a computer program provided by NASA (based on the formulation in References 9 and 10) to calculate C_N, C_M, and phase for an airfoil oscillating in a wind tunnel. Comparative free-air values were obtained from the data tables in Reference 11. The theoretical values were based on compressible thin airfoil theory, with the method of images used to simulate the tunnel walls.

The amplitude ratios of C_N and C_M in free air to the values in a tunnel, as well as phase differences, are shown in Figure 45. The corrections to magnitude, which are largest at low values of k and high Mach number, are all less than 14 percent. The corrections to phase are all less than 10 degrees, except for the pitching moment at M = 0.6 and low values of k.

The corrections calculated here were found to be small in comparison with the large changes in both magnitude and phase due to stall, and therefore they have not been included in the wind tunnel results.

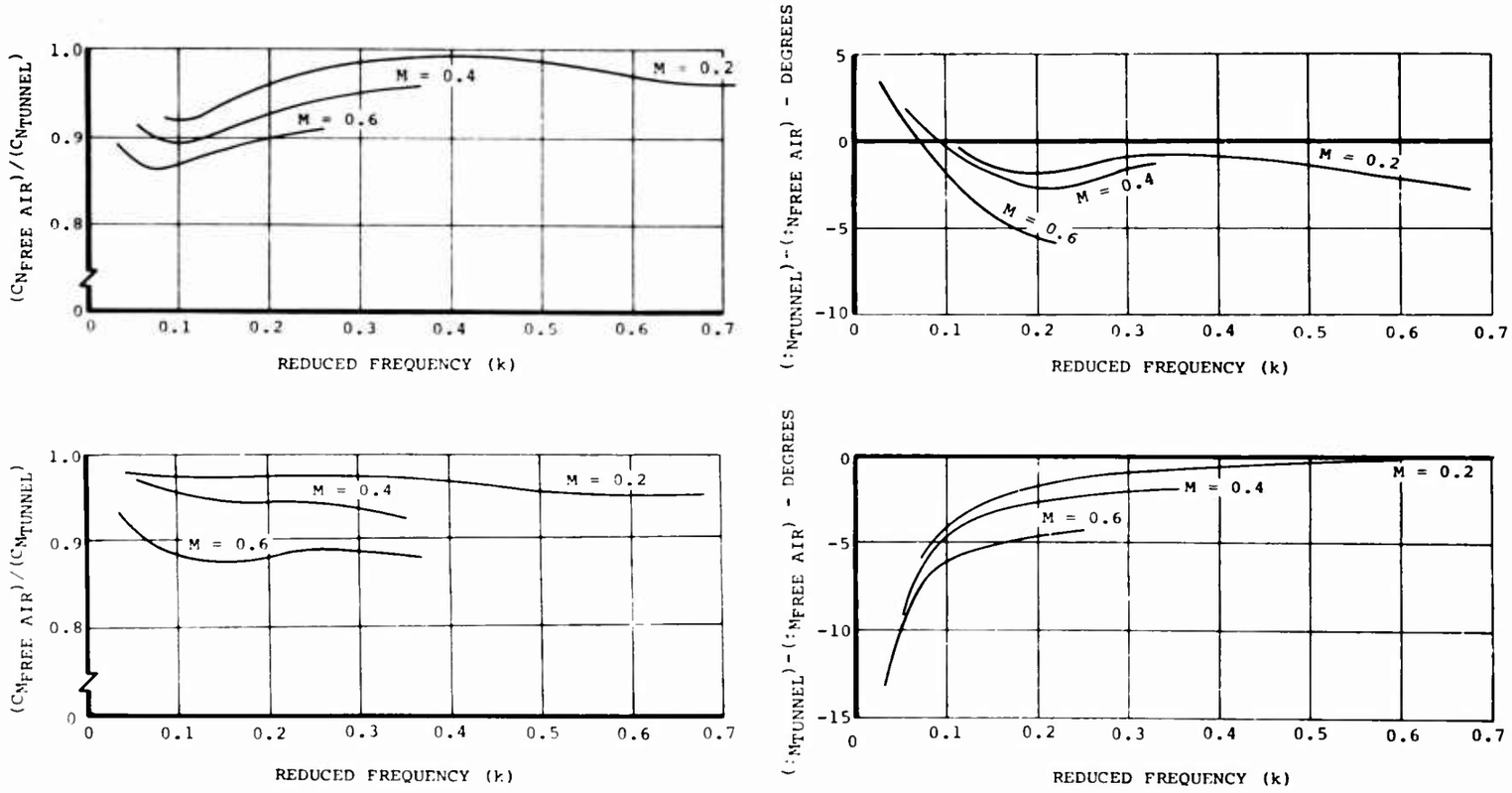

Figure 45. Wind Tunnel Wall Corrections for Pitching Oscillation.

BLANK PAGE

UNCLASSIFIED

Security Classification

DOCUMENT CONTROL DATA - R & D

(Security classification of title, body of abstract and indexing annotation must be entered when the overall report is classified)

1. ORIGINATING ACTIVITY (Corporate author) The Boeing Company Vertol Division Philadelphia, Pennsylvania	2a. REPORT SECURITY CLASSIFICATION Unclassified 2b. GROUP

3. REPORT TITLE
WIND TUNNEL TESTS OF THIN AIRFOILS OSCILLATING NEAR STALL
VOLUME I, SUMMARY AND EVALUATION OF RESULTS

4. DESCRIPTIVE NOTES (Type of report and inclusive dates)
Final Report, 6-27-67 through 8-15-68

5. AUTHOR(S) (First name, middle initial, last name)
Lewis Gray
Jaan Liiva
Franklyn J. Davenport

6. REPORT DATE January 1969	7a. TOTAL NO. OF PAGES 85	7b. NO. OF REFS 11
8a. CONTRACT OR GRANT NO. DAAJ02-67-C-0095 b. PROJECT NO. c. Task 1F162204A13903 d.	9a. ORIGINATOR'S REPORT NUMBER(S) USAAVLABS Technical Report 68-89A 9b. OTHER REPORT NO(S) (Any other numbers that may be assigned this report) D8-0925-1	

10. DISTRIBUTION STATEMENT
This report has been approved for public release and sale; its distribution is unlimited.

11. SUPPLEMENTARY NOTES Volume I of a 2-volume report	12. SPONSORING MILITARY ACTIVITY U.S. Army Aviation Materiel Laboratories Fort Eustis, Virginia

13. ABSTRACT

This report presents the results of an experimental investigation of rotor blade dynamic stall. Forces and moments in two-dimensional flow were determined for two thin airfoil sections (NACA 0006 and Vertol 13006-.7) usually considered in advanced helicopter rotor concepts by measuring differential pressure during oscillatory pitch motions. The Mach number, Reynolds number, and angle of attack prevailing in the retreating-blade stall region were investigated up to typical first-torsion mode natural frequencies.

Pitch oscillation was shown to increase the angle of attack at which stall occurred, with a corresponding increase in maximum normal force. Hysteresis effects on the pitching moment response produced regions of negative aerodynamic damping in oscillations at mean angles of attack near the steady-flow stall values for all Mach numbers from 0.2 to 0.6.

It is shown that dynamic stall effects are strongly related to the reduced frequency parameter. Significant evidence of compressibility effects appears only at Mach numbers higher than 0.4. At lower Mach numbers, the data indicate that the two effects of decreased Mach number and airfoil camber are fully comparable in terms of dynamic stall patterns and increase both the usable angle of attack and the maximum normal force.

DD FORM 1 NOV 68 1473 REPLACES DD FORM 1473, 1 JAN 64, WHICH IS OBSOLETE FOR ARMY USE.

UNCLASSIFIED

Security Classification

UNCLASSIFIED

Security Classification

14. KEY WORDS	LINK A		LINK B		LINK C	
	ROLE	WT	ROLE	WT	ROLE	WT
Two-dimensional flow						
Thin airfoils						
Oscillating near stall						
NACA 0006						
Vertol 13006-.7						
Mach Number						
Reynolds number						
Angle of attack						
Hysteresis effects						
Negative aerodynamic damping						
Dynamic stall						

UNCLASSIFIED

Security Classification

153-69